Protein Bioconjugation to Carbon Nanotubes for Near-Infrared Sensing

Thèse N° 7175

Présentée le 28 juin 2019

à la Faculté des sciences de base
Laboratoire de nanobiotechnologie
Programme doctoral en chimie et génie chimique

pour l'obtention du grade de Docteur ès Sciences

par

Vitalijs ZUBKOVS

Acceptée sur proposition du jury

Prof. S. Gerber, présidente du jury
Prof. A. A. Boghossian, directrice de thèse
Prof. C.-J. Shih, rapporteur
Prof. T. Hertel, rapporteur
Dr G. Wagnières , rapporteur

2019

ÉCOLE POLYTECHNIQUE
FÉDÉRALE DE LAUSANNE

The more we share, the more we have.
— *Leonard Nimoy*

Acknowledgements

I am grateful to my advisor Prof. **Ardemis A. Boghossian**, who supported my research and encouraged me on my journey into the unknown. She honored me by giving me the opportunity to join the Laboratory of Nanobiotechnology as the first PhD student. I was there during the time when the lab was growing in number of its members and expanding in its research capacity. Ardemis guided me in the first steps of my project and encouraged me during the times when I faced challenges, which happened throughout my doctorate years. I am thankful to her for giving a chance to develop optical microscopes, to work on the project as the part of the multinational team, and to support my curiosity in research.

I am beholden to **Nils Schürgers** with whom I worked together on many projects. He is a great scientist and a virtuous person. His guidance helped me to frame my ideas, and his way of doing science became an example. Nils taught me to be critical, but positive, and to carry out research with passion, without losing the taste for fun in private life. All my good and hilarious memories from the hikes we did together, will stay forever in my mind.

A very special thanks to my colleagues, **Alessandra Antonucci**, **Shang-Jung Wu**, **Benjamin Lambert**, **Alice Gillen**, **Mohammed Mouhib**, and **Melania Reggente**, for sharing laboratory benches, coffee breaks, evenings in Sat, and climbing. Alessandra is the kindest person I have ever known. Shang-Jung is a smart and innovative researcher, who knows everything about everything. Benjamin has an unleashed imagination for excellent and unexpected ideas. Alice is the energy booster of the lab discussions, I appreciated a lot her help in shaping ideas and having a critical look on the statistical relevance of results. Mohammed knows the ABCs in synthetic biology and is always keen on trying things out. Melania gives the lab a positive mood and expresses limitless energy in everything she does.

I wish to thank all the internship and project students with whom I worked and shared exciting times: **Esra Ahunbay**, **Benjamin Lambert**, **Manuel Moradell-Casellas**, **Sayed Yahya Rahnamaei**, and **Raha Rajaei**. It was great fun and an enjoyable experience to work together. You enabled me to discover how much more one can learn from teaching.

Words cannot express my gratefulness to my **parents** and my **sister**. I am at my place because they taught me to listen to the heart and follow the mind. They have always supported my desires and given advice when needed.

Last but not least, I thank my friends and the brilliant minds whom I met at EPFL. **Carlos Macias Romero** who was my mentor in optics and taught me how to build new things on an empty optical breadboard. **Ossama Khalaf** who is exceptionally intelligent and the best running partner. **Jens Antons** and **Anja Holzheu** - my rock-climbing teammates. **Maiia Bragina**, **Sergey Arzoyan**, **Roman Bulushev**, **Maxim Norkin**, and **Anna Rozenblit** who added laughter to my lunches at EPFL. I thank the **EPFL Toastmasters Club members** for all the interesting chats we had during my doctorate studies. Also, I express my gratitude to everyone who supported me in this scientific odyssey.

Lausanne, 18 April 2019
V. Z.

Abstract

Single-walled carbon nanotubes (SWCNTs) are a promising material for electrochemical and optical biosensing applications. Their small dimensions, large surface area, indefinite photostability, and remarkable electronic properties make SWCNTs an ideal transducer in optical sensors. SWCNTs fluoresce in the near-infrared (NIR)-II region of the light spectrum, between 1000 and 1350 nm. The absorbance of living tissue and cells reaches a minimum within this spectral range, making SWCNTs an excellent material for *in vivo* sensor implants. Although inherently non-selective, a selective optical response can be imparted to SWCNTs for a specific analyte through appropriate surface functionalization, commonly achieved using oligonucleotides or proteins. The type of biofunctionalization dictates the specificity, biocompatibility, and overall stability of the composite. Therefore, targeted engineering of the SWCNT surface coating is critical for the development of improved optical sensors.

This PhD thesis is focused on producing, and further researching, protein-SWCNT composites, with a specific aim towards their application for glucose sensing. The proposed sensors consist of SWCNTs, acting as the optical transducer element, and a glucose-selective protein, glucose oxidase (GOx), which was used to activate the nanotube surface and impart selectivity. This study presents the design and fabrication of a reversible, mediatorless sensor that undergoes a selective fluorescence increase in the presence of glucose.

The first sensor comprises of non-specifically adsorbed GOx onto the sidewall of SWCNTs. Incorporating this GOx-SWCNT composite into a custom-built sensor device enabled the selective and reversible detection of glucose. Further, the focus was directed towards designing a method to immobilize the protein onto the SWCNT through a non-covalently bound linker molecule, which would impart greater long-term stability.

In order to achieve this goal, a site-specific protein conjugation method was developed and optimized using enhanced yellow fluorescence protein (EYFP) with synthetically-engineered surface cysteine. The protein was conjugated to a N-(1-pyrenyl)-maleimide (PM) linker and immobilized onto SWCNTs *via* $\pi - \pi$ stacking. Protein conjugation and immobilization were confirmed using absorbance and fluorescence spectroscopy, and time-resolved NIR spectroscopy was employed to study the protein-/protein-linker-SWCNT interactions. This work demonstrated that the secondary structure of the protein was preserved to a higher degree by employing the PM-linker compared to relying on non-specific protein adsorption. These

findings imply that PM-based immobilization is the most promising method for engineering protein-based SWCNT optical sensors.

Based on these findings, the GOx was conjugated to the PM linker in order to immobilize the protein onto the SWCNTs. That was achieved through bioengineering of GOx variants with accessible surface cysteine. The resultant GOx-PM-SWCNT sensor demonstrated a reversible response towards glucose in liquid. Given the requirement of sensors capable of continuous, long-term monitoring in diabetes management, future devices can undoubtedly benefit from the advantages offered by this technology.

Keywords: carbon nanotubes, SWCNT, near-infrared fluorescence, proteins, bioconjugation, sensors, glucose oxidase, GOx, enhanced yellow fluorescent protein, EYFP

Résumé

Les nanotubes de carbone monoparoi (SWCNT) sont un matériau prometteur pour la création de biosenseurs électrochimiques et optiques. Leurs petites dimensions, leur importante surface de contact, leur photostabilité illimitée et leurs propriétés électroniques singulières font des SWCNTs un transducteur idéal pour les senseurs optiques. Les SWCNTs émettent une fluorescence dans la région du proche infrarouge (NIR)-II du spectre lumineux, entre 1000 et 1350 nm. L'absorption des tissus et des cellules vivantes atteint un minimum dans cette région spectrale, faisant des SWCNT une excellente plateforme pour l'élaboration de biosenseurs *in vivo*. Bien qu'intrinsèquement non sélectifs, une réponse optique sélective pour un composant spécifique peut être conférée aux SWCNTs par le biais d'une fonctionnalisation de surface appropriée, couramment obtenue à l'aide d'oligonucléotides ou de protéines. Le type de biofonctionnalisation dicte la spécificité, la biocompatibilité et la stabilité globale du complexe. Ainsi, une ingénierie ciblée de la fonctionnalisation de surface des SWCNTs est essentielle pour le développement de senseurs optiques améliorés.

Cette thèse de doctorat porte sur la production et la poursuite de recherches sur les complexes protéine-SWCNT dans le but spécifique de les appliquer à la détection du glucose. Les senseurs proposés sont composés de SWCNTs, jouant le rôle de transducteurs optiques, et d'une protéine sélective au glucose, la glucose oxydase (GOx), utilisée pour conférer une sélectivité au nanotube. Cette étude présente la conception et la fabrication d'un senseur réversible sans médiateur subissant une augmentation sélective de la fluorescence en présence de glucose.

Le premier senseur présente des GOx non spécifiquement adsorbés sur la paroi latérale des SWCNTs. L'incorporation de ce complexe GOx-SWCNT dans un dispositif de détection personnalisée a permis la mesure sélective du glucose. De plus, l'accent a été mis sur la conception d'un procédé d'immobilisation de la protéine sur le SWCNT par le biais d'une molécule de liaison immobilisée sur le nanotube de façon non-covalente, conférerant alors une plus grande stabilité à long terme.

Afin d'atteindre cet objectif, une méthode de conjugaison spécifique à certains sites particuliers de protéines a été développée et optimisée en utilisant la protéine fluorescente jaune (EYFP) présentant une cystéine de surface modifiée synthétiquement. La protéine a été conjuguée à un lieur N-(1-pyrényl)-maléimide (PM) et immobilisée sur des SWCNTs *via* une liaison entre orbitales π-π. La conjugaison et l'immobilisation des protéines ont été confirmées

par spectroscopie d'absorbance et de fluorescence, et une spectroscopie NIR à résolution temporelle a été utilisée afin d'étudier les interactions protéine / protéine-PM-SWCNT. Ces travaux ont démontré que la structure secondaire de la protéine était préservée à un degré plus élevé en utilisant le lieur PM par rapport à une adsorption non spécifique de la protéine. Ces résultats impliquent que l'immobilisation à l'aide lieur PM est la plus prometteuse pour l'ingénierie de senseurs optiques SWCNT à base de protéines.

Sur la base de ces découvertes, la protéine GOx a été conjuguée au lieur PM afin de l'immobiliser sur les SWCNTs. Pour y parvenir, une variante de la GOx, avec une cystéine accessible sur sa surface, a été créée. Le senseur résultant GOx-PM-SWCNT a démontré une réponse réversible au glucose en milieu liquide. Compte tenu de la nécessité de senseurs capables de mesure continue et à long terme du glucose dans le traitement du diabète, de futurs appareils pourraient sans aucun doute bénéficier des avantages offerts par cette technologie.

Mots-clés : nanotubes de carbone, SWCNT, fluorescence proche infrarouge, protéines, bioconjugaison, senseurs, glucose oxydase, GOx, protéine fluorescente jaune, EYFP

Contents

Abbreviations

A	Adenine
ABTS	2,2'-Azino-bis(3-ethylBenzoThiazoline-6-Sulfonic acid) diammonium salt
AFM	Atomic Force Microscopy
BMD	Buffered Minimal Dextrose growth medium
BMM	Buffered Minimal dextrose Methanol growth medium
C	Cytosine
CCD	Charge-Coupled Device
CD	Circular Dichroism
CoMoCAT	Cobalt–Molybdenum CATalyzed
DBCO	DiBenzoCycloOctyne-maleimide
DMSO	DiMethyl SulfOxide
DRIFT	Diffuse-Reflectance Infrared Fourier Transform
EDTA	EthyleneDiamineTetraAcetic acid
EMCCD	Electron-Multiplying Charge-Coupled Device
EYFP	Enhanced Yellow Fluorescent Protein
FAD	Flavin Adenine Dinucleotide
FTIR	Fourier Transform InfraRed
FWHM	Full-Width at Half-Maximum
G	Guanine
GOx	Glucose Oxidase
HiPco	High-Pressure carbon monoxide process
HRP	HorseRadish Peroxidase
InGaAs	Indium Gallium Arsenide
LB	Lysogeny Broth growth medium
LOWESS	LOcally WEighted Scatterplot Smoothing
MSD	Mean Squared Displacement
MWCO	Molecular Weight Cut-Off
NA	Numerical Aperture
NHE	Normal Hydrogen Electrode
NIR	Near-InfraRed
PBS	sodium Phosphate-Buffered Saline
PDB	Protein Data Bank

PDMS	PolyDiMethylSiloxane
PM	N-(1-Pyrenyl)-Maleimide
PVA	PolyVinyl Alcohol
QDs	Quantum Dots
QY	Quantum Yield
RBM	Radial Breathing Mode
RNA	RiboNucleic Acid
SC	Sodium Cholate
SDC	Sodium DeoxyCholate
SDCLM	Spinning-Disc Confocal Light Microscopy
SDS-PAGE	Sodium Dodecyl Sulfate-PolyAcrylamide Gel Electrophoresis
SDS	Sodium Dodecyl Sulfate
SNR	Signal-to-Noise Ratio
SPDP	N-Succinimidyl 3-(2-PyriDyldithio)Propionate
ssDNA	single-stranded DeoxyriboNucleic Acid
SWCNT	Single-Walled Carbon Nanotube
T	Thymine
TCEP	Tris(2-CarboxyEthyl)Phosphine
TIR	Total Internal Reflection
uPAINT	universal Point Accumulation Imaging in Nanoscale Topography
UV	UltraViolet
Vis	Visible
WT	Wild Type
YPD	Yeast extract Peptone Dextrose growth medium

List of Figures

List of Tables

Introduction

Properties of carbon nanotubes

Since their discovery in 1991, carbon nanotubes emerged as promising materials for catalysis, electronics, and medicine [1–3]. Carbon nanotubes can be categorized as either multi-walled or single-walled. A single-walled carbon nanotube (SWCNT) appears as a rolled-up graphene sheet yielding a monolayer of sp^2 carbon atoms arranged in a tube, as depicted in **Figure 1a**. The direction in which the graphene sheet is rolled results in various nanotube chiralities, which are each designated by n and m indices. These indices correspond to a specific combination of chiral angle for the rolling direction and diameter for the rolling distance. The physical properties of SWCNTs vary among these chiralities: if n - m = 0, then the SWCNTs have metallic properties; when n - m = 3p (where p is an integer), the SWCNTs are semimetallic; and if n - m ≠ 3p, then the SWCNTs are semiconducting. The semiconducting SWCNTs show intrinsic fluorescence that can be useful for optoelectronic applications (**Figure 1b**).

The fluorescence of SWCNTs originates from the excitons (electron-hole pairs) on the surface, resulting in emission wavelengths that are specific to the chiralities (**Figure 1c**). Aqueous dispersions of SWCNTs fluoresce in the near-infrared (NIR) region between 900 and 1400 nm [4, 5]. The radiative energy (E_{ii}) of the peaks depends not only on the nanotube's chiral angle but also on structural and chemical defects on the SWCNT surface and the local dielectric environment [6, 7]. The carbon nanotube can interact with ions, solvents, surfactants, and other molecules in close proximity to the surface [6, 8, 9]. Therefore, environmental changes on the surface of the SWCNT can modulate the fluorescence emission.

Surface functionalization effects on SWCNT fluorescence

To obtain colloidal dispersions in aqueous solutions, the SWCNT surface is functionalized with wrappings such as surfactants, polymers, oligomers, and biomolecules [10, 11]. The surface functionalization can alter the SWCNT optical properties, such as: the emission energy of the SWCNT peaks, the fluorescence quantum yield (QY), or the fluorescence responsivity towards analytes. The optical response of these wrappings towards an analyte of interest is modulated through several possible interactions (**Figure 2**): (**i**) analyte-induced conformational change of the SWCNT wrapping, (**ii**) adsorption of the analyte onto the SWCNT, (**iii**) electron transfer

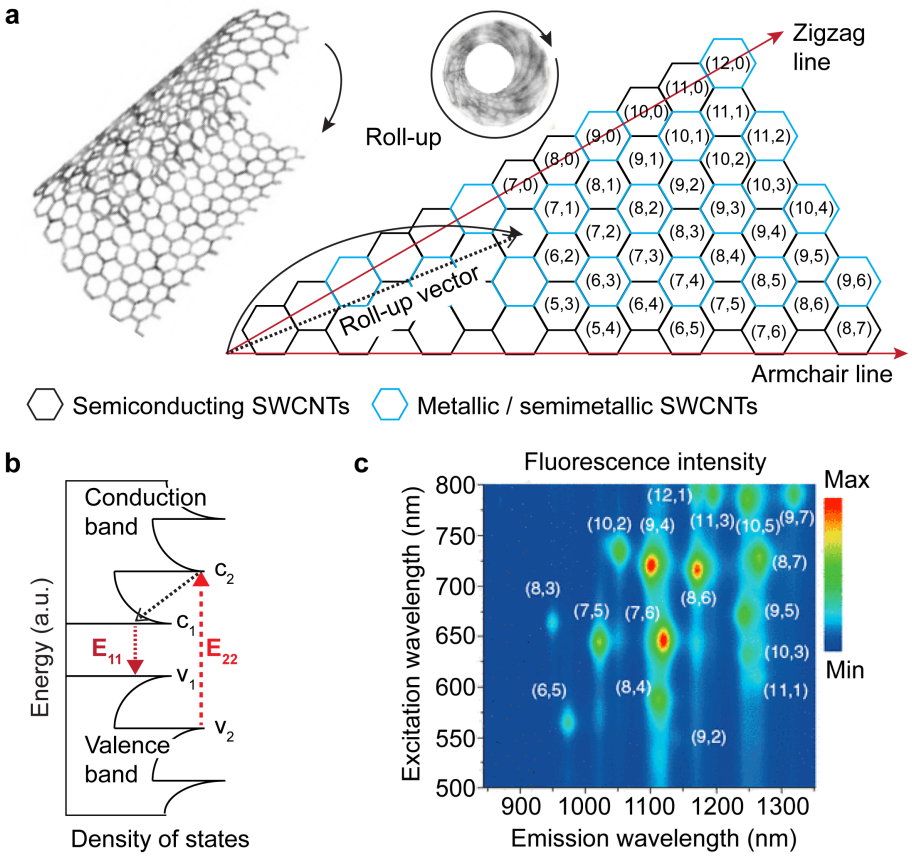

Figure 1 – Chirality and optical properties of SWCNTs. **(a)** Graphical representation of roll-up vectors of a graphene sheet into the SWCNT. The roll-up vector results in SWCNTs with different *(n,m)* indices or chiralities. Depending on the chirality, the SWCNT can have metallic, semimetallic, or semiconducting properties. **(b)** Electronic band diagrams of semiconducting SWCNTs show density of states at valence and conductive energy bands. **(c)** The photoluminescence map of sodium cholate-suspended SWCNTs (HiPco^{TM} SWCNTs) shows positions of the characteristic peaks corresponding to the specific *(n,m)* semiconducting SWCNT chiralities.

between the analyte and the SWCNT, and (**iv**) electron transfer between the analyte and the SWCNT wrapping [6]. Engineering of SWCNT wrappings is critical in the design of a sensor with an analyte-specific fluorescence response. The above-mentioned interactions can result in a wavelength shift of the fluorescence peak, a change in fluorescence intensity, or both [12]. Thus, the ratio of the fluorescence intensity or the wavelength shift can be correlated with the amount of analyte present in a solution [6, 13].

One of the most common SWCNT surface wrappings is single-stranded DNA (ssDNA). Representative fluorescence spectra of (6,5) chirality-enriched SWCNTs functionalized with six ssDNA sequences, C_{30}, T_{30}, A_{30}, G_{30}, $(GT)_{15}$, and $(AT)_{15}$ are shown in **Chapter 1**, **Figure 1.1d**.

The SWCNTs were excited in the NIR region at 808 nm, and multiple emission peaks corresponding to different chiralities are seen on the spectra. The ssDNA sequences are shown to encapsulate certain chiralities preferentially; therefore, the relative magnitudes of the chirality peaks can vary with the sequence [14]. In addition to analyte specificity and chirality distribution, the surface wrapping may also alter the fluorescence QY, which is an important parameter for biosensing. Unfortunately, the absolute QYs of functionalized SWCNTs are low, achieving, for example, 1.5% for polyfluorene-wrapped SWCNTs and 1.1% for surfactant-suspended SWCNTs [4, 5, 15, 16]. Since the SWCNT surface often provides recombination sites for excitons, surface defects can diminish or completely quench the fluorescence [7, 17].

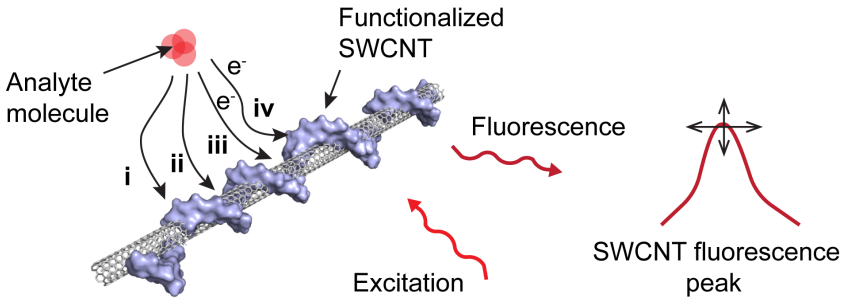

Figure 2 – Functionalization of SWCNTs. The illustration shows interactions between an analyte and functionalized SWCNTs. The symbols indicate: (**i**) conformational change of the SWCNT wrapping due to interaction with the analyte, (**ii**) adsorption of the analyte to the SWCNT, (**iii**) electron transfer between the analyte and the SWCNT, and (**iv**) electron transfer between the analyte and the SWCNT wrapping. The arrows on the SWCNT fluorescence peak indicate a wavelength shift and/or a fluorescence intensity change. The illustration was reproduced from *Polo et al.* [6].

Protein immobilization onto SWCNTs for sensing applications

In addition to ssDNA, proteins provide an alternative wrapping for optical SWCNT-based sensors. Enzymes in particular benefit from their intrinsic selectivity and reactivity to an analyte. Furthermore, non-covalent functionalization of SWCNTs with proteins may also promote biocompatibility while preserving the intrinsic fluorescence of SWCNTs [18].

The literature reports four major non-covalent SWCNT-protein functionalization approaches (**Figure 3**): (**i**) direct adsorption of proteins onto the SWCNT sidewall; (**ii**) helical ssDNA wrapping containing reactive groups that can conjugate to proteins; (**iii**) amphipathic polymers that contain hydrophobic regions that stack onto a SWCNT and hydrophilic chains for protein conjugation; (**iv**) protein conjugation to pyrene-containing linkers that are non-covalently immobilized onto SWCNTs [18–21]. Non-specific adsorption (method **i**) is the most facile and scalable of these methods [22, 23]. However, despite its advantages, adsorption is limited to proteins capable of suspending SWCNTs through, for example, sufficient hydrophobic interactions at the surface [24]. In addition, protein adsorption on the nanostructure may also disturb protein conformation, leading to a significant reduction of protein activity [25–27].

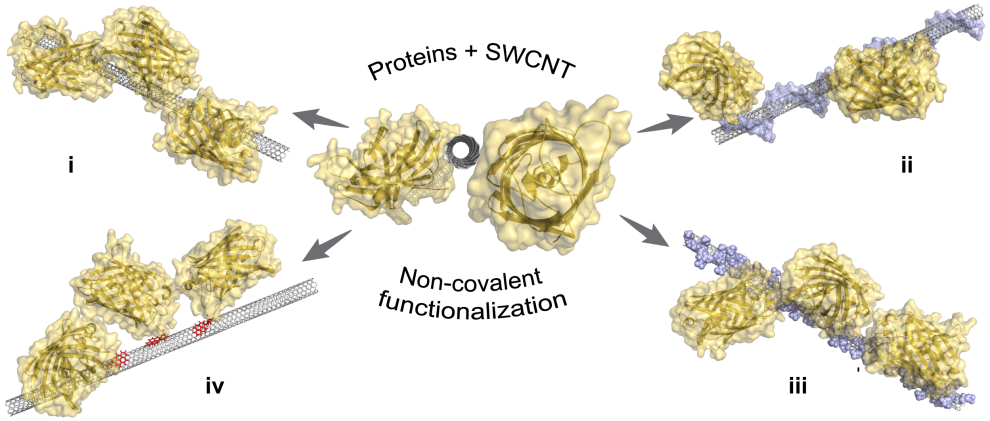

Figure 3 – Approaches for non-covalent immobilization of proteins onto a SWCNT. The graphic indicates four protein immobilization approaches: **(i)** direct adsorption of proteins onto a sidewall of the SWCNT; **(ii)**helical SWCNT wrapping with ssDNA containing reactive groups that can link to a protein; **(iii)** stacking of the hydrophobic region of an amphipathic polymer onto the SWCNT and protein conjugation to the polymer's hydrophilic chains; **(iv)** protein conjugation to pyrene-containing linkers that are immobilized onto the SWCNT.

The two polymer-based SWCNT functionalization approaches include method **ii**, biopolymer wrappings (ssDNA), and method **iii**, amphipathic polymer wrappings such as branched polyethyleneglycol phospholipids [28]. In these approaches, after SWCNT surface functionalization with the polymer, proteins are subsequently covalently linked to functional groups contained by the polymers. A disadvantage of ssDNA functionalization approach is that certain ssDNA sequences may be intrinsically sensitive to specific analytes or ions, as discussed above, which could interfere with the protein-induced signals [8]. In contrast to ssDNA, amphipathic polymers may benefit from more populated functional groups that can accommodate a larger number of proteins. However, long, synthetic polymers may randomly wrap onto the SWCNT surface and produce scaffolds that could restrict interactions between the protein and the surface of a SWCNT [29].

Pyrene-containing linkers described in method **iv** benefit from less inherently intrusive contributions to the SWCNT surface. These moieties are highly resistant to desorption from SWCNTs in aqueous solutions [21]. To date, pyrene derivatives such as 1-pyrenebutyric acid, 1-pyrenebutanoic acid succinimidyl ester, or damantane–pyrene, biotin–pyrene, and nitrilotriacetic acid (NTA)–pyrene were largely used for cross-linking [30–35]. These linkers cross-link with primary and secondary amine groups (-NH_2) present in protein amino acids, such as lysine, asparagine, and glutamine, as well as the N-terminus of a polypeptide chain.

NIR SWCNT-based sensors for *in vivo* monitoring

When SWCNTs are dispersed in aqueous solutions, they fluoresce in the NIR region, where absorption of water, proteins, hemoglobin, melanin, and DNA is low (**Figure 4a**). The op-

tical region between 1000 and 1350 nm (called the NIR-II window) is attractive for sensing because the absorbance of biological tissue is minimal [36, 37]. In the NIR-II region, SWCNT fluorescence can be imaged at a high resolution even at a 1 cm tissue depth [38, 39]. Therefore, SWCNTs are promising candidates for *in vivo* applications compared to conventional fluorophores that typically fluoresce in the visible wavelength region and can interfere with endogenous compounds [39, 40]. Furthermore, the indefinite photostability of SWCNTs allows long-term and continuous fluorescence monitoring.

In vivo implementation of a SWCNT-based sensor is illustrated in **Figure 4b**. This illustration shows an encapsulated SWCNT sensor that is implanted in adipose tissue under the skin. Other research groups have demonstrated encapsulations in hydrogels or semipermeable membranes for analyte monitoring *in vivo* [41, 42]. For example, *Heller et al.* demonstrated *in vivo* RNA detection with the 100 pmol sensitivity using a microRNA (GT15mir19) SWCNT-based sensor in a mouse [41]. A more recent feasibility study demonstrated the application of SWCNT-based sensors for analyte monitoring in marine animals [43]. Hydrogel-encapsulated sensors were implanted in the muscle tissue of deceased teleost fish, a deseased catshark, and a turtle. Fluorescence signals were collected from implants inserted 7 mm within the tissue [43], validating the potential use of optical SWCNT sensors for monitoring aquatic animals.

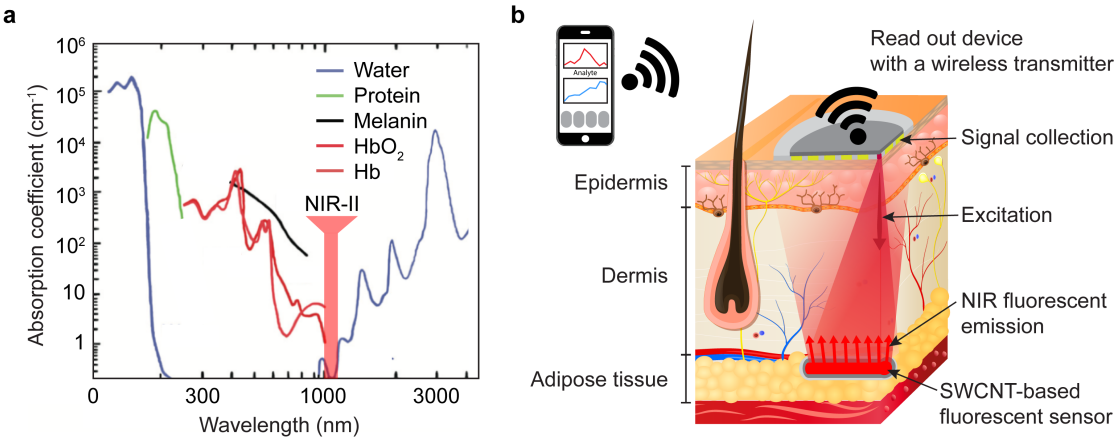

Figure 4 – *In vivo* implementation of SWCNT-based sensors. (a) Absorption coefficients for common endogenous substances: water, proteins, melanin, oxyhemoglobin (HbO_2), hemoglobin (Hb). The plot is reproduced from *Vogel and Venugopalan* [44]. **(b)** The illustration shows the implementation of implantable SWCNT-based NIR sensors for continuous analyte monitoring *in vivo*. The sensor readings are wirelessly transmitted to a smartphone. The illustration was reproduced from *Bisker et al.* [45].

Sensors for diabetes management

Diabetes is a metabolic disease characterized by the failure to control blood sugar, or glucose, levels. High saccharide levels of up to 10 mM may cause hyperglycemia, leading to health complications such as blindness, amputation, kidney failure, heart disease, and strokes.

Conversely, rapid depletion of blood sugar may lead to hypoglycemia, resulting in sudden patient collapse [46]. Therefore, blood glucose concentrations must be maintained at healthy physiological levels between 4 and 8 mM [47]. Although the cure for diabetes does not yet exist, the disease can be treated by monitoring blood glucose and adjusting sugar levels with a strict diet and insulin regiments. The International Diabetes Federation reported that in 2017, between 346.4 and 545.4 million adults (20 to 79 years old) worldwide had diabetes, and these numbers could reach 808.7 million by 2045 [48]. Provided that hyperglycemia alone already contributes to approximately 3.7 million deaths per year, the number of deaths could double in the next 25 years due to the increasing number of diabetics [48].

At present, diabetics inject insulin *via* subcutaneous insulin injections, insulin pumps, or pens. Frequent injections using these methods are inconvenient to patients, who gradually become reluctant to treat the disease. Moreover, most diabetics must also manually monitor their blood glucose level by frequently pricking their fingers and using a glucose meter to analyze the extracted blood. Given the crucial need for these devices for managing diabetes, glucose meters constitute about 85% of the total biosensor market [49]. Among the variety of glucose monitoring devices currently available, only very few are applicable for continuous glucose monitoring. Continuous glucose monitoring sensors allow better control of diabetes, and therefore, long-lasting sensors are highly sought. Continuous glucose monitoring sensors that are based on electrochemical glucose detection are typically limited to two weeks of consecutive use [50, 51]. Advances in glucose detection by optical means can increase the lifespan of continuous glucose sensors to six months while also providing to patients an implantable approach to monitor their glucose levels using light [52, 53]. However, the fluorescent dyes often employed in these optical sensors photobleach under prolonged illumination and require multiple daily recalibration procedures through blood extraction [54]. Therefore, photostable alternatives are needed for continuous glucose monitoring and general sensing applications.

Selectivity towards glucose detection can be achieved by functionalizing the SWCNT surface with proteins such as glucose-binding protein, glucose dehydrogenase, concanavalin A, or glucose oxidase (GOx) [19, 20, 55, 56]. GOx is the gold standard for commercial glucose sensing due to its high specificity to glucose and stability [57]. When immobilized onto the sidewall of the SWCNT, GOx was shown to stimulate a glucose-specific response in electrochemical and optical sensors [19]. Several proof-of-concept optical glucose sensors based on SWCNTs have already been demonstrated [13, 19], though the optical sensors, reported before this study, are not reversible and require redox mediators such as potassium ferricyanide [13, 58]. The addition of exogenous mediators is unfavorable for implantable sensors because of cytotoxicity and stability [13].

Objectives of the thesis

The goal of this thesis is to develop protein-based bioconjugation strategies for optical SWCNT-based sensors and to apply these strategies in creating a reversible, mediatorless optical glucose sensor. The realization of optical SWCNT sensors requires the development of custom-built optical setups that can record fluorescence emissions from SWCNTs in the NIR region. Following their development, these setups were used to characterize and compare several protein-SWCNT immobilization methods, particularly in the context of creating a glucose sensor. This work combines techniques in optics, bioengineering, nanomaterials engineering, chemical synthesis, and fluorescence spectroscopy towards achieving viable protein-based SWCNT sensors.

This thesis has five chapters which have been or are expected to be published in international peer-reviewed journals. The outline for each chapter is listed below.

Chapter 1: *Optical systems for NIR imaging and spectroscopy*

The first milestone of this thesis was to develop tools for NIR imaging and spectroscopy, which are necessary for detecting the fluorescence emitted from SWCNTs. In addition to a wide-field imaging and NIR spectroscopy microscope, we developed a state-of-the-art spinning-disc confocal microscope that is specific to NIR emissions, as presented in **Chapter 1**. This setup was used to demonstrate applications including imaging of ssDNA-SWCNTs in organelles, confocal tracking of NIR particles, as well as spatiotemporal detection of glucose using NIR sensors. To the best of our knowledge, this development represents the first reported spinning-disc confocal NIR-II microscope in the world, and it has since found use in applications beyond SWCNT fluorescence imaging.

Chapter 2: *Mediator-free optical GOx-SWCNT glucose sensor*

The second milestone was to apply the custom-built constructs described in **Chapter 1** to develop a NIR optical glucose sensor based on non-specific enzyme adsorption onto the SWCNT surface. **Chapter 2** discusses the development of a reversible glucose sensor capable of detecting physiological concentrations of glucose in the absence of added mediators. Furthermore, it introduces a fundamentally new mechanism for protein-suspended SWCNT sensors based on enzymatic pocket doping.

Chapter 3: *Non-covalent bioconjugation of proteins to SWCNTs*

The third milestone was to enhance protein-based sensor performance by developing new bioconjugation approaches to immobilizing a protein onto a SWCNT. These strategies aim to achieve improved retention and site-specific orientation of the protein. **Chapter 3** focuses on non-covalent protein immobilization through cysteine-reactive linkers. In this chapter, we

engineered an EYFP variant with a surface-accessible cysteine as a model protein for verifying and comparing bioconjugation. The protein was cross-linked with ssDNA-wrapped SWCNTs or immobilized onto the SWCNT surface through a PM linker.

Chapter 4: *GOx-PM-SWCNT sensors for continuous glucose monitoring*

The final milestone of this thesis was to apply the protein immobilization methods described in **Chapter 3** to improve the glucose sensor. An engineered GOx variant with surface cysteines was site-specifically immobilized onto the sidewall of the SWCNT using the PM linker. **Chapter 4** describes GOx bioengineering methods, the fabrication of the GOx-PM-SWCNT sensor, and a new platform for continuous analyte monitoring.

Chapter 5: *Outlook towards portable fluorescence monitoring device*

This chapter demonstrates a portable device for detecting fluorescence emitted from SWCNT-based sensors. The setups established in **Chapter 1** are used as a basis for a portable prototype to be used for point-of-care health monitoring. This chapter concludes with an outlook on using this device to achieve the commercialization of the glucose sensors developed in this thesis.

1 Optical systems for NIR imaging and spectroscopy

This chapter consists of an article published in Scientific Reports with the title: ***Spinning-disc confocal microscopy in the second near-infrared window (NIR-II)*** *[59]. The co-authors of this article are: A. Antonucci, N. Schuergers, B. Lambert, A. Latini, R. Ceccarelli, A. Santinelli, A. Rogov, D. Ciepielewski, A. A. Boghossian. (DOI: 10.1038/s41598-018-31928-y)*

Author contributions: *V.Z., A.A., N.S., A.S., B.L., and A.A.B. participated in experimental design. V.Z. and A.A. performed the experiments. A.L., R.C., and A.S. developed the NIR confocal spinning-disc module, and V.Z., A.R., and D.C. conceived, designed, and integrated the NIR confocal microscope. V.Z., N.S., and A.A.B. wrote the manuscript. V.Z. and A.A.B. conceived and designed the research.*

1.1 Abstract

Fluorescence microscopy in the NIR-II optical window (1000-1350 nm) has become a technique of choice for non-invasive *in vivo* imaging. The deep penetration of NIR light in living tissue, as well as negligible tissue autofluorescence within this optical range, offers increased resolution and contrast with even greater penetration depths. In this chapter, we present two custom-built setups used for NIR SWCNT fluorescence characterization. First, we present a custom-built conventional wide-field microscope capable of fluorescence imaging and excitation-emission spectroscopy. We demonstrate the use of this setup in generating SWCNT excitation-emission maps as well as determining the QYs of various ssDNA-suspended SWCNTs. Next, we discuss in detail a spinning-disc confocal laser microscope (SDCLM) that is specific to imaging in the NIR-II. The SDCLM achieves a lateral resolution of 0.5±0.1 µm and an axial resolution of 0.6±0.1 µm, showing a 17% and 45% enhancement in lateral and axial resolution, respectively, compared to the corresponding wide-field configuration. We furthermore showcase several applications that demonstrate the use of the SDCLM for *in situ*, spatiotemporal tracking of NIR particles and bioanalytes within both synthetic and biological systems.

1.2 Introduction

A variety of NIR fluorophores, such as SWCNTs, quantum dots (QDs), inorganic nanoparticles, fluorescent proteins, and dyes, have been specifically developed for imaging and optical sensing applications [36, 37, 60–64]. These fluorophores span wavelengths throughout the NIR window from 700 to 1350 nm [65–67]. Since biological pigments like lipopigments and porphyrins are autofluorescent between 650 and 950 nm [37, 68, 69], and water strongly absorbs light between 1350 and 1500 nm [65, 70], fluorophores that lie within the NIR-II region from 1000 to 1350 nm specifically benefit from low cross-contamination and increased tissue penetration, permitting deep-tissue imaging and sensing applications (**Table 1.1**). NIR organic dyes in particular also benefit from biocompatibility and relatively simple conjugation methods that can be used on a variety of different substrates, including proteins and polymers. However, photobleaching of the dyes limits long-term monitoring; for example, the fluorescence intensity of IR-1061, a commercially available NIR dye, has been shown to drop to 50% of its initial value after 1250 s of continuous illumination at 808 nm when dissolved in dimethyl sulfoxide [71]. Although synthetic nanoparticles such as QDs are also susceptible to photobleaching in addition to cytotoxicity that limits their use *in vivo*, they enjoy advantages such as greater emission tunability [37]. Alternatively, certain synthetic nano-particles such as SWCNTs show indefinite photostability and can be functionalized to achieve improved biocompatibility. Despite QYs on the order of just 0.1%, the fluorescence tunability, indefinite stability, and improved biocompatibility make SWCNTs a formidable option for *in vivo* imaging and sensing applications [72, 73].

Several existing setups are capable of imaging and characterizing the expanding number of fluorophores in the NIR-II window. Similar in construction to conventional visible range optical microscopes, these setups are mostly distinguished by the use of a NIR-specific camera with an InGaAs sensor. This thesis work similarly includes the construction of such a wide-field optical setup capable of NIR imaging and spectroscopy. This conventional setup, shown in **Figure 1.1a** consists of a supercontinuum laser and a tunable wavelength filter (from 400 to 830 nm). The laser light is directed into a 20x objective *via* a dichroic mirror (with an 830 nm long-pass coating). The sample is illuminated from the bottom and the emitted light from SWCNTs is collected in the epi-configuration. The emission light passing through an 830 nm long-pass filter and is focused onto a spectrometer with the InGaAs NIR camera. The supercontinuum laser can be used to illuminate samples for wide-field imaging (**Figure 1.1b**) or for spectroscopy of NIR fluorophores, such as ssDNA-SWCNTs, across a range of excitation wavelengths to capture the emissions of various SWCNT chiralities (**Figure 1.1c**). Fluorescence emissions for different ssDNA wrappings (**Figure 1.1d**), show sequence-dependent chirality distributions and QYs. As summarized in **Table 1.2**, this setup can be used to calculate QYs based on the integrated fluorescence intensities shown in **Figure 1.1c** and fluorescence spectra relative to the reference dye, IR-26 (0.11±0.02% measured in 1,2-dichloroethane) [78]. The

Table 1.1 – Fluorophores with emission maxima in the NIR-II window between 1000 and 1350 nm. The fluorophores are listed by excitation wavelength maxima in ascending order

Fluorophore	Chemical structure	Ex. (nm)	Em. (nm)	QY (%)	Year	Ref.
(7,6) SWCNT	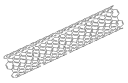	650	1120	0.1	1991	[73]
CH-4T	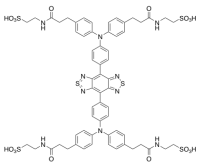	740	1000	11	2017	[74]
CH1055	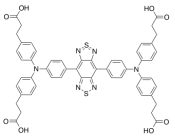	750	1055	0.3	2015	[60]
H1	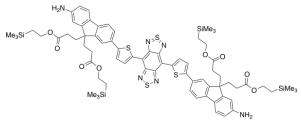	800	1100	2	2017	[75]
Q4	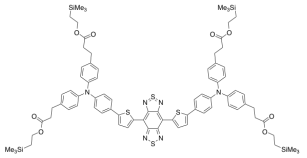	880	1100	-	2016	[76]
CQS1000	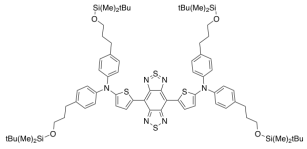	885	1000	-	2016	[76, 77]
IR-1061	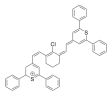	1074	1132	1.7	2014	[71]
IR-26	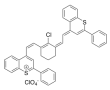	1080	1190	0.5	1981	[74, 76]
PbS QDs (∅ 4.4 nm)	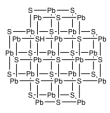	1250	1280	45	1994	[78]
PbSe QDs (∅ 4.3 nm)	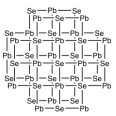	1300	1350	41	2001	[78–80]

SWCNT QYs (Φ_x) in this table were calculated using the following formula:

$$\Phi_x = \frac{A_{ref} \times F_x \times (n_x)^2}{A_x \times F_{ref} \times (n_{ref})^2} \times \Phi_{ref} \tag{1.1}$$

where the A_{ref} and A_x are absorbances of the IR-26 and SWCNTs solutions, F_{ref} and F_x are the areas under the emission curves of the reference and ssDNA-SWCNTs, respectively, Φ_{ref} is the QY of IR-26, and n_{ref} and n_x are the refractive indices of the solvent for the reference dye and ssDNA-SWCNT, respectively. For each of the wrappings, four replicate fluorescence spectra were integrated throughout the NIR region to calculate an average QY. Even though the C_{30} wrapping has the largest QY from among the ssDNA sequences, the $(GT)_{15}$ sequence shows the highest selectivity toward the (6,5) chirality [81].

Table 1.2 – Experimentally measured QYs of ssDNA-SWCNTs. Data adapted from [81]

Embodiment	**QY (%) x 10^{-2}**
C_{30}-SWCNT	5.3 ± 0.6
T_{30}-SWCNT	0.9 ± 0.1
A_{30}-SWCNT	2.0 ± 0.1
G_{30}-SWCNT	3.3 ± 0.4
$(GT)_{15}$-SWCNT	4.7 ± 0.6
$(AT)_{15}$-SWCNT	4.6±0.5

Compared to this conventional setup, recent advancements in wide-field deconvolution, laser-scanning confocal and super-resolution microscopy offer promising approaches to achieving even higher resolution images of NIR-II fluorophores [82–85]. However, these methods require relatively long acquisition times that limit their use for real-time monitoring [84]. An alternative approach is SDCLM, which is a high-speed optical sectioning technique widely used in biological sciences [86]. Whereas existing commercially available setups are largely limited to confocal fluorescence imaging in the visible region of the optical spectrum, this thesis presents a first-of-its-kind spinning-disc confocal setup tailored for imaging in the NIR-II window. The resolution limits and acquisition speed of the microscope are determined and subsequently used to image SWCNTs. The advantages of NIR SDCLM imaging is exemplarily demonstrated in three distinct applications: single-particle tracking of NIR fluorescent nanoparticles in solution, the spatial distribution of internalized nanoparticles within an organelle, and optical detection of glucose using immobilized SWCNT-based sensors.

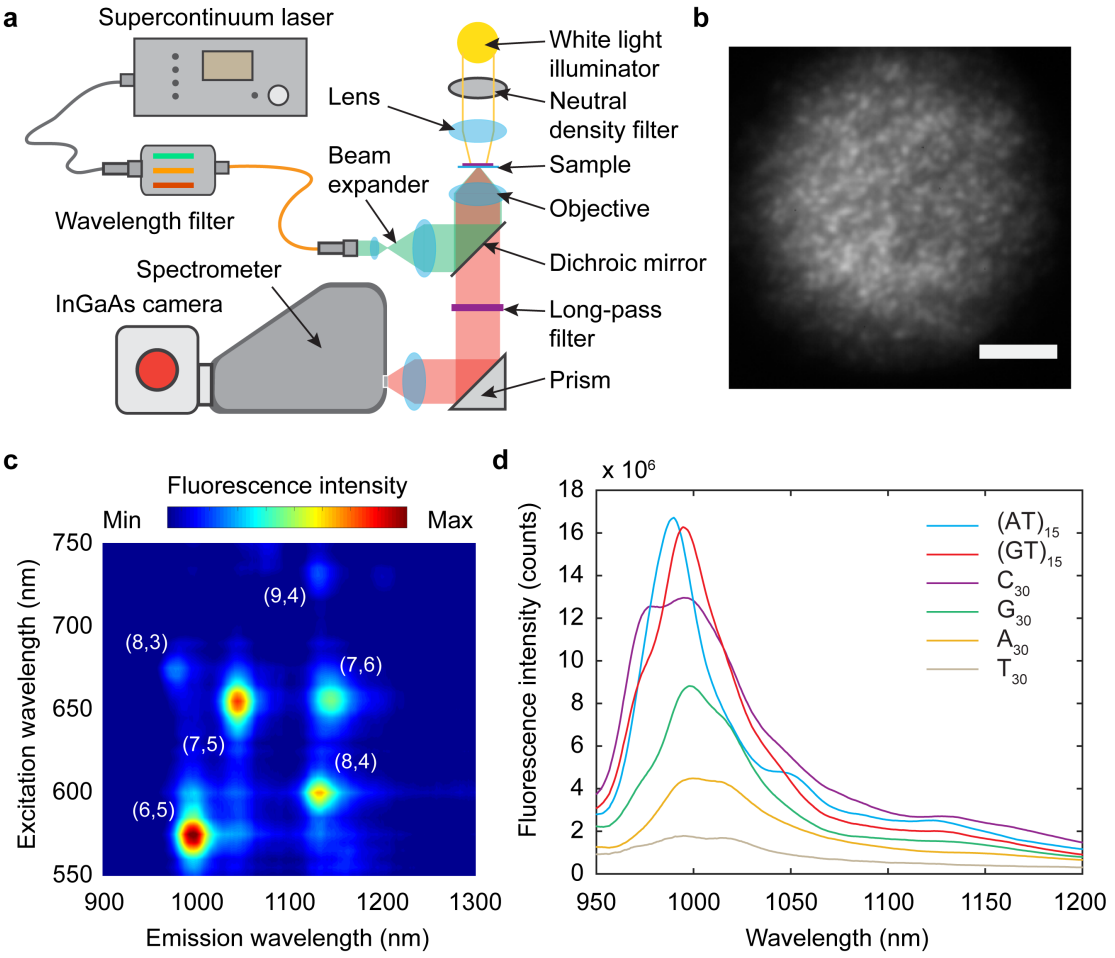

Figure 1.1 – Conventional wide-field optical setup for NIR fluorescence spectroscopy. (a) Schematic of the custom-built optical setup for wide-field imaging and excitation-emission spectroscopy. **(b)** Fluorescence image of SWCNTs immobilized on a glass slide recorded using the setup (a). Excitation at 785 nm, emission above 800 nm. Scale bar = 100 µm. **(c)** Excitation-emission map of the $(GT)_{15}$-SWCNTs (CoMoCAT^{TM} SWCNTs) suspension obtained using the setup shown in (a). **(d)** NIR fluorescence spectra of C_{30}, G_{30}, T_{30}, A_{30}, $(GT)_{15}$, $(AT)_{15}$-wrapped SWCNTs in water. The ssDNA-SWCNT suspensions were prepared *via* sonication using (6,5)-enriched SWCNTs. Excitation at 808 nm. All spectra were normalized to the ssDNA-SWCNT absorbances at 808 nm.

1.3 Materials and methods

Confocal NIR fluorescence microscope. The 640, 660, and 780 nm continuous wave (CW) laser light sources (Triline Laser Bank, Cairn Research) are coupled to a Nikon Eclipse Ti-E microscope body by an optical fiber (FT1500 EMT, 0.39 NA) (see **Figure A.1**). Both 780±5 nm band-pass and 830 nm short-pass filters (Semrock) were installed in front of the fiber output. The laser light passes through a spinning-disc confocal unit (X-light, CrestOptics) that includes discs of spinning arrays with pinholes (⌀ 60 µm) and lenses coated with a NIR anti-reflection layer (transmittance >60% in the wavelength range from 0.7 to 1.2 µm, see **Figure A.2**). The

excitation and emission beams are split by a dichroic mirror. When the microscope was operated in the wide-field configuration for comparison, the confocal assembly was removed from the light path. Samples mounted in the XYZ-translational stage were all illuminated through a TIRF Apo 100x 1.49 NA oil immersion objective (Nikon Instruments) and 1.5x tubelens. The fluorescence signal is collected in the epi-direction through a 980±15 nm band-pass (ChromaTechnology) or a 980 nm long-pass (BLP01-980R-25, Semrock) filter by a cooled indium gallium arsenide (InGaAs) camera (NIRvana 640 ST, Princeton Instruments). The laser power at the sample plane in the wide-field and confocal configurations are 2.6 W cm^{-2} and 1.8 W cm^{-2}, respectively. Images were acquired using the Nikon NIS-Elements software (Nikon Instruments).

Imaging of NIR fluorescent beads. Fluorophorex™ NIR fluorescent polystyrene beads with a mean diameter of 186 ±48 nm were purchased from Phosphorex Inc. Beads were diluted to ~ 3×10^{10} particles per mL and 5 µL of the sample were spin-coated on a glass coverslip at 3 000 rpm for 30 s following sonication (Polos SPIN150i, Semiconductor Production Systems). A drop of immersion oil (refractive index 1.515 at 23 °C, Type A, Nikon) was added on top of the coated layer, and bead fluorescence was imaged using an axial step size of 0.1 µm with 780 nm laser excitation and a 980 ±15 nm band-pass filter. The optical resolution of the setup was determined from the lateral and axial FWHM fits of the imaged beads using the PSFj software [87].

Wide-field imaging in the visible light region. Glass coverslips were spin-coated with either 5 µL of EYFPs (expressed and purified from genetically modified *Escherichia coli* cells) in a buffered solution or 5 µL of a QD suspension (Qdot 655 ITK amino(PEG), Life technologies corporation). Sample fluorescence was imaged in the wide-field configuration using an EMCCD camera (the objective with NA 1.49 and iXon Ultra Andor camera) using 480±15 nm excitation (Optoscan, Cairn) with a 525 ± 25 nm band-pass filter (Semrock) for EYFP or 425±15 nm excitation with a 640 ± 15 nm band-pass filter (Semrock) for the QDs. The optical resolutions of the setup were determined from the lateral and axial FWHM fits of the imaged beads using PSFj software.

Diffusion coefficients of the NIR fluorescent beads in different concentrations of glycerol. NIR beads were sonicated and suspended in water and in 25, 50, and 75 v/v% glycerol solutions (99.5% glycerol, Carl Roth) to a concentration of ~ 3×10^{10} particles per mL. 50 µL of each suspension were deposited in a glass-bottom petri dish (35 mm, ibidi). The fluorescence emission of the diffusing NIR beads was recorded over 5 min through an Apo 40x 1.3 NA objective (Nikon Instruments) and a 1x tube lens with a frame rate of 20 fps. All experiments were performed at 20 °C. The particle displacement tracks and diffusion coefficients were determined from 2D image stacks using the ParticleTracker plugin of Fiji [88]. In the calculations of the average and median distributions of the diffusion coefficients, we considered only particles with diffusion trajectories longer than 12 frames (or 0.6 s), and the total number of frames per track was limited to 1000.

Uptake of SWCNTs by isolated plant chloroplasts. Chloroplasts were isolated from commercially available spinach leaves as described previously [89]. 15 g of spinach leaves were ground using a mortar and pestle in 30 mL of ice-cooled chloroplast isolation buffer (0.05 M PBS (pH 7.3) with 0.4 M sucrose and 0.01 M KCl). Next, the suspension was centrifuged at 200 × g for 1 min at 4 °C to pellet unbroken cells and fragments. The supernatant was collected and transferred to a 50 mL tube. Centrifugation of the solution was repeated three times at 1 500 × g for 10 min at 4 °C, and pellets with chloroplasts were stored in the dark at 4 °C. Freshly isolated chloroplasts at a concentration of 5 mg chlorophyll L^{-1} were incubated for 15 min with 10 mg L^{-1} suspensions of ssDNA- or PVA-SWCNTs and imaged by the NIR confocal microscope. The ssDNA- and PVA-SWCNT suspensions were prepared according to previously reported protocols [90, 91].

Glucose detection in an agarose gel with GOx-SWCNT sensors. 50 mg of SWCNTs (single-walled carbon nanotube – (7,6) chirality, 704121, Sigma Aldrich) were suspended in 50 mL of 2 wt% SC (Sigma Aldrich) in PBS (pH 7.4, gibco®, Life Technologies). The suspension was sonicated for 30 min at 1% amplitude (1/4" tip, Q700 Sonicator, Qsonica) in an ice bath and centrifuged at 164 000 × g for 4 h (Optima XPN-80 Ultracentrifuge, Beckman Coulter) to remove aggregates. Next, 30 mg of GOx from *A. niger* (Type II, Sigma Aldrich) was added to 1 mL of the SC-suspended SWCNTs and dialyzed in a 14 kDa MWCO dialysis tube (cellulose membrane, D9777, Sigma Aldrich) against 1.5 L of PBS at 4 °C. The GOx-SWCNT suspension was subsequently transferred to a 300 kDa MWCO dialysis device (Spectra/Por® Float-A-Lyzer®, Spectrum Laboratories) and dialyzed overnight at 4 °C. 10 µL of the GOx-SWCNTs was mixed with 10 µL of a warm (40 - 50 °C) 4% agarose gel in PBS (ultrapure Agarose, invitrogen), and 10 µL of this mixture were drop-casted in a well with a glass-bottom device fabricated from polydimethylsiloxane (PDMS). 50 µL of PBS was added on the top of the gel to prevent drying. The sample was mounted on the microscope's specimen holder, and 60 µL of 30 mM glucose (β-D-glucose, AB 136302, abcr) in PBS was added to the well. The fluorescence signal was recorded in the confocal microscope with an acquisition time of 0.5 s and scan rate of 2.3 s between Z-slices (excitation at 660 nm, a long-pass 980 nm emission filter). The time-lapse Z-stacks were further analyzed using a customized MATLAB script.

1.4 Results and discussion

1.4.1 Spatial resolutions of NIR microscopes

Our SDCLM setup consists of a spinning-disc module coupled to a cooled InGaAs camera installed on a Nikon Eclipse Ti-E microscope body (see **Figure A.1**). Lenses in the spinning-disc confocal unit were coated with a NIR anti-reflective layer to maximize photon throughput (see **Figure A.2**). The disc can be removed from the optical path to image a specimen in the wide-field configuration. We compared images of NIR fluorescent beads (186±48 nm diameter) recorded in the wide-field and confocal microscope configurations (**Figure 1.2**). The beads were immersed in oil with a refractive index of n = 1.515. As shown in **Figure 1.2a**,

the confocal image (right) offers better image contrast and clearer distinction between two neighboring beads in comparison to the wide-field image (left). The intensity profiles of the lateral cross-sections in **Figure 1.2b** show that the two beads remain unresolved in the wide-field image when the distance between them is 0.6 µm, while they are clearly separated by confocal imaging. The full-width at half-maximum (FWHM) of lateral cross-sections of single beads are 0.6±0.1 µm and 0.5±0.1 µm in wide-field and confocal modes, respectively (see **Table A.1**). According to the Abbe equation, the theoretical lateral resolution limit in the wide-field configuration is r_x^{WF} = 0.33 µm (**Equation 1.2**, where the wavelength is λ_{EM}= 980 nm and the numerical aperture is NA = 1.49) [92].

$$r_x^{WF} = 0.5\frac{\lambda_{EM}}{NA} \tag{1.2}$$

We note that this theoretical resolution does not precisely account for all types of aberrations present in an optical setup nor signal-to-noise restrictions, and it is therefore typically lower than the experimental values [96, 99]. The lateral resolution is improved within the confocal microscope by limiting the out-of-focus emissions using small confocal pinholes with a diameter of 0.5 Airy units (AU) (or 60 µm), with one AU at the disc plane equal to 120 µm (**Equation 1.3**, λ_{EM} = 980 nm, NA = 1.49, magnification = 150x). Hence, the theoretical lateral resolution of the confocal microscope is calculated to be r_x^{CF} = 0.26 µm (**Equation 1.4**, the lateral FWHM pre-factor is F_x = 0.40) [93].

$$d_x = AU = 1.22\frac{\lambda_{EM}}{NA} \tag{1.3}$$

$$r_x^{CF} = F_x\frac{\lambda_{EM}}{NA} \tag{1.4}$$

The empirical lateral resolution is approximately half that of the theoretical limit. This difference can be explained by spherical aberrations of the optical lenses and a mismatch in the refractive indices of the sample media and coverglass [94, 96].
We determined the axial resolution of the imaging system through longitudinal scanning of the fluorescent beads (**Figure 1.2c**) measuring the FWHM of emission intensities in the Z-direction. The axial resolution of 1.1±0.1 µm in the wide-field configuration is surpassed by a resolution of 0.6±0.1 µm in the confocal configuration (see **Table A.2**). These values are close to the lowest experimental values of ~1.0 µm and ~0.5 µm reported for wide-field and confocal fluorescence microscopes in the visible light region [100]. The theoretical axial resolution for the confocal configuration is r_z^{CF} = 0.52 µm (**Equation 1.6**, with F_z equal to 0.66 for the 60 µm spinning-disc pinholes), which is slightly smaller than the experimental value (**Figure 1.2d**).

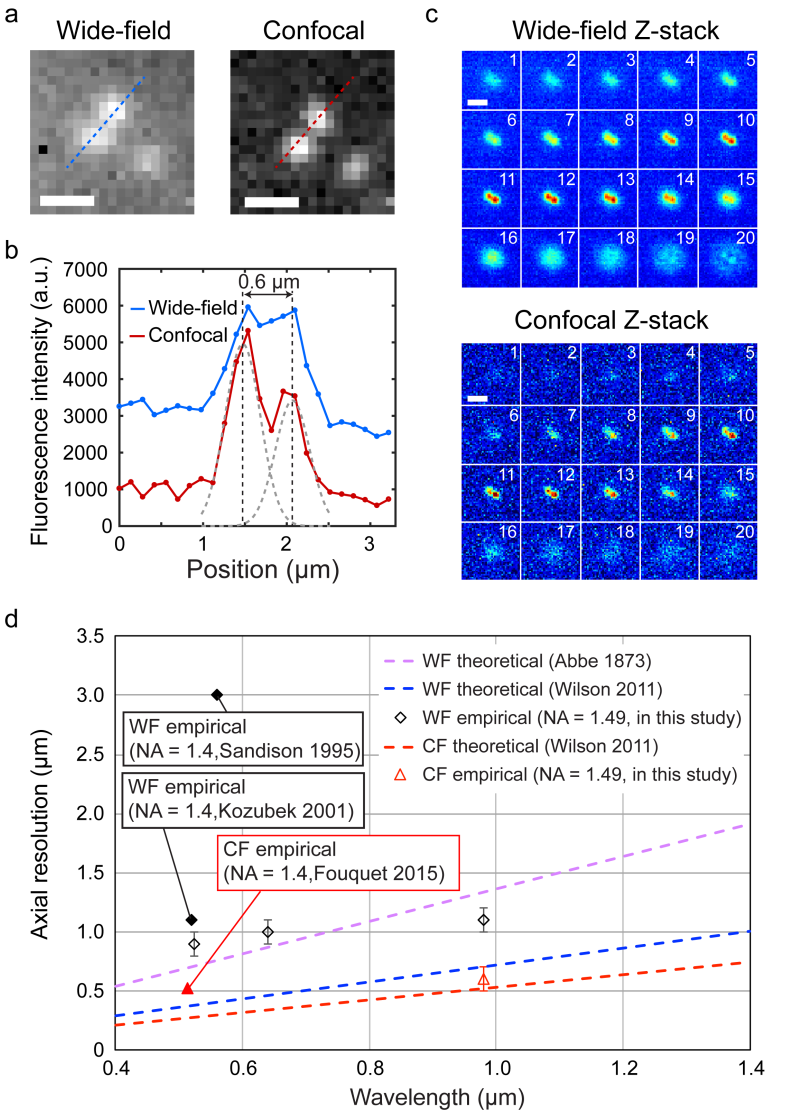

Figure 1.2 – Comparison of wide-field (WF) and spinning-disc confocal (CF) NIR microscope images. **(a)** Wide-field (left) and confocal (right) images of 186±48 nm NIR fluorescent beads. Scale bar = 1 μm. **(b)** Intensity profiles of the cross-sections indicated in (a) by dashed lines. **(c)** Z-stack projection of wide-field (top) and confocal (bottom) images of the fluorescent beads. Scale bar = 2 μm. **(d)** Wavelength dependence of theoretical and determined axial resolutions. The theoretical resolutions were calculated according to **Equation 1.5** (purple dashed line) and **Equation 1.6** for wide-field F_z = 0.89 (blue dashed line) and confocal F_z = 0.66 (red dashed line) cases, where NA = 1.49, n = 1.515 [93–95]. Empirical resolutions in the wide-field settings (white diamonds) were determined using enhanced yellow fluorescent protein (excitation at 480 nm, emission at 525 nm), quantum dots (excitation at 425 nm, emission at 640 nm), and NIR beads (excitation at 780 nm, emission at 980 nm), and they were compared to empirical data in the literature (shaded diamonds) [96, 97]. The empirical resolution in the confocal settings (red triangle) was determined using NIR beads (excitation at 780 nm, emission at 980 nm), and it was compared to empirical data in the literature (shaded triangle) [98].

The improvement in axial resolution by ~45% in the confocal mode therefore offers enhanced precision for imaging sub-micrometer objects, as reported later in this article.

$$r_z^{WF} = \frac{2 \times \lambda_{EM} \times n}{NA^2} \tag{1.5}$$

$$r_z^{CF} = F_z \frac{\lambda_{EM}}{n - \sqrt{n^2 - NA^2}} \tag{1.6}$$

1.4.2 Image acquisition speed in NIR microscopy

In comparison to point-scanning NIR confocal microscopes or NIR super-resolution systems, SDCLMs allow faster image acquisition. Capturing an area of 50 × 50 µm with a NIR uPAINT setup takes more than two seconds [101]. The confocal microscope allows for high spatial resolution while the spinning-disc maintains fast imaging acquisition speeds. The disc rotates at 15 000 RPM (250 Hz), and it is designed to achieve the maximal theoretical acquisition speed of ~18 000 fps, which is equivalent to a minimal exposure time of ~50 µs. However, the NIRvana 640 InGaAs camera in this setup limits the acquisition time to 110 fps or 9 ms. When imaging NIR beads, minimum capturing times of 20 fps or 50 ms (see **Figure A.3**) were selected to achieve a desirable signal-to-noise ratio of more than 40 [102]. Accordingly, the predominant factor limiting acquisition speed in this SDCLM setup is the brightness of the NIR fluorophores.

1.4.3 Temporal imaging of diffusing NIR beads

We tracked the 2D Brownian motion of NIR fluorescent beads in viscous solutions containing different concentrations of glycerol using both wide-field and confocal configurations (**Figure 1.3**). The particle trajectories were used to determine diffusion coefficients D according to the formula [103],

$$MSD = 4 \times D \times t \tag{1.7}$$

where MSD is the mean-squared displacement and t is time. The median diffusivity in water is ~25% higher based on trajectories from the confocal configuration compared to those obtained from the wide-field configuration (**Figure1.3a**). This difference is attributed to the more precise tracking of bead movement in the axial direction and thinner plane of the confocal configuration. To minimize the contribution of particles traversing the axial direction, which leads to underestimation of particle diffusivity, we only consider tracks that

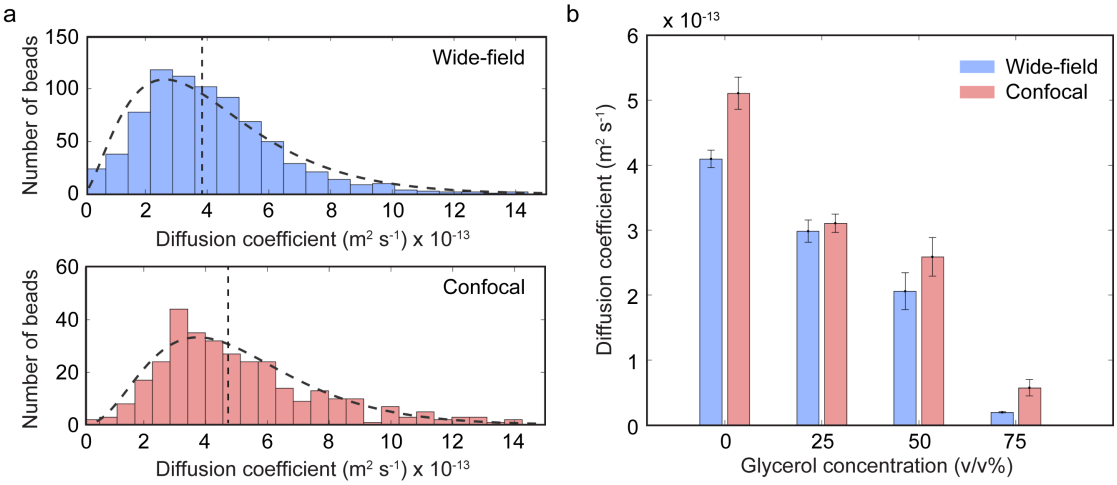

Figure 1.3 – Tracking of single NIR beads in water and viscous glycerol solutions. **(a)** Distribution of calculated diffusion coefficients of NIR beads in water. The dashed lines are fits to the beta distribution function. Median values for the wide-field and confocal distributions are 3.72 $\times$ 10^{-13} m^2 s^{-1} and 4.67 $\times$ 10^{-13} m^2 s^{-1} (vertical dashed lines), respectively. **(b)** Mean diffusion coefficients of NIR beads in 0, 25, 50, 75 v/v% aqueous glycerol solutions (error bars represent 95% confidence intervals). Between 300 and 800 bead trajectories were analyzed for each set of conditions.

are longer than 0.6 s (12 frames) in calculating the average and median diffusivities. As a consequence, the wide-field trajectories slightly underestimate the diffusivity since particles move in the axial direction for longer distances (and time) before leaving the plane. The mean diffusion coefficient was calculated for solutions containing different concentrations of glycerol (**Figure 1.3b**). According to the Stokes-Einstein equation [104, 105],

$$D = \frac{k_B \times T}{6 \times \pi \times \eta \times r} \tag{1.8}$$

where k_B s Boltzmann's constant, T is temperature, η is dynamic viscosity, and r is the radius of the spherical particle, the diffusivity is expected to vary inversely with solution viscosity. At 20 °C, the corresponding diffusivities for the glycerol solutions at 0, 25, 50, and 75 v/v%, with dynamic viscosities between 0.001 kg m^{-1} s^{-1} for pure water and 0.055 kg m^{-1} s^{-1} for 75 v/v% glycerol, are predicted to range between (18.3–30.9) $\times$ 10^{-13}, (7.3–12.4) $\times$ 10^{-13}, (2.1–3.5) $\times$ 10^{-13}, and (0.3–0.6) $\times$ 10^{-13} m^2 s^{-1}, respectively. Though these values largely lie within the same order of magnitude as the experimental values calculated from the MSD trajectories, the experimental values tend to lie below predicted values, particularly for lower glycerol concentrations where particles are expected to diffuse much more quickly. This observation suggests that limited frame rate may result in the underestimation of diffusivities for faster diffusing particles. Nonetheless, the values reported herein for the confocal measurements are closer to the theoretical value than the wide-field measurements, which further underestimate the measured diffusivities.

1.4.4 3D localization of SWCNTs in plant chloroplasts

The improved SDCLM resolution offers a promising basis for enhanced *in vitro* and *in vivo* imaging. We explored this prospect by imaging functionalized SWCNTs within photosynthetic chloroplasts [89]. Chloroplasts are organelles that autofluoresce in the visible range of the spectrum, benefitting in particular from imaging techniques that use NIR dyes with distinct fluorescent wavelengths. Although fluorescent properties of SWCNTs are attractive for NIR imaging inside living cells and organelles, their uptake can strongly depend on surface functionalization and the properties of wrapping polymers. Previous studies have shown that wrappings conferring a strongly positive or negative zeta potential allow SWCNTs to traverse the outer membrane of chloroplasts [106]. In agreement with these findings, our measurements show that extracted chloroplasts do not internalize polyvinyl alcohol-wrapped SWCNTs (PVA-SWCNTs), which are predicted to have an almost neutral surface zeta potential [107], while ssDNA-SWCNTs that exhibit a large negative zeta potential (approximately −45 mV in PBS pH 7) readily localize within the organelles (**Figure 1.4a**). The NIR imaging shows an inhomogeneous localization of SWCNTs within the chloroplast, with the sharper resolution offered in the confocal z-stack images revealing a rather granular distribution of SWCNT fluorescence, particularly in areas with low SWCNT fluorescence (**Figure 1.4b**). The axial distribution of ssDNA-SWCNTs in chloroplasts could not be readily discerned in the confocal Raman images reported in previous studies because of a limited axial resolution of 2 µm [106].

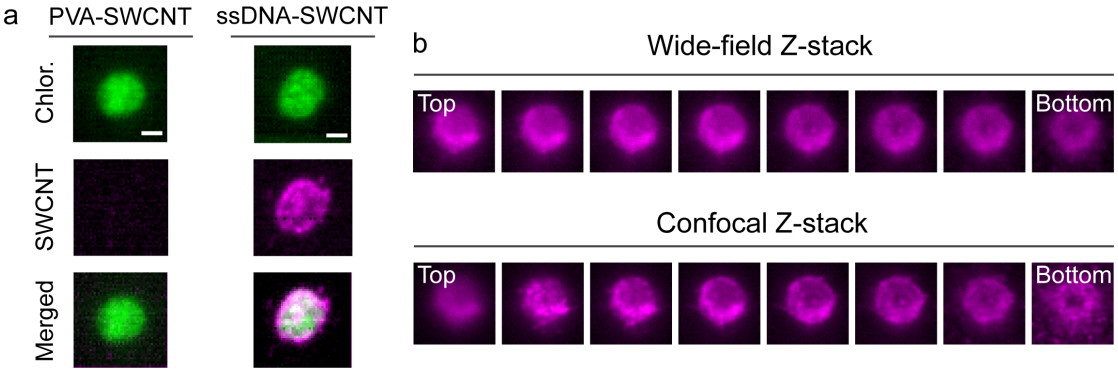

Figure 1.4 – Internalization of functionalized SWCNTs in a chloroplast. **(a)** Autofluorescence (green,excitation at 640 nm, emission above 950 nm), SWCNT fluorescence (violet, excitation at 780 nm, emission above 980 nm), and merged confocal images recorded after incubation with PVA-SWCNTs and ssDNA-SWCNTs. Scale bar = 2 µm. **(b)** NIR wide-field and confocal Z-stack images of ssDNA-SWCNTs within an isolated chloroplast (step size = 0.4 µm, excitation at 780 nm, emission above 980 nm).

1.4.5 Spatiotemporal glucose detection in an agarose gel

SWCNTs are typically functionalized with bio-molecules such as DNA, RNA, and proteins to enhance their fluorescence response towards specific analytes [18, 23, 41, 42]. One example is the use of the GOx-SWCNT sensors, which undergo a specific increase in fluorescence intensity in response to glucose [19]. Such biosensors are often encapsulated in gel matrices such as agarose prior to implantation for *in vivo* monitoring. Ensemble measurements of the

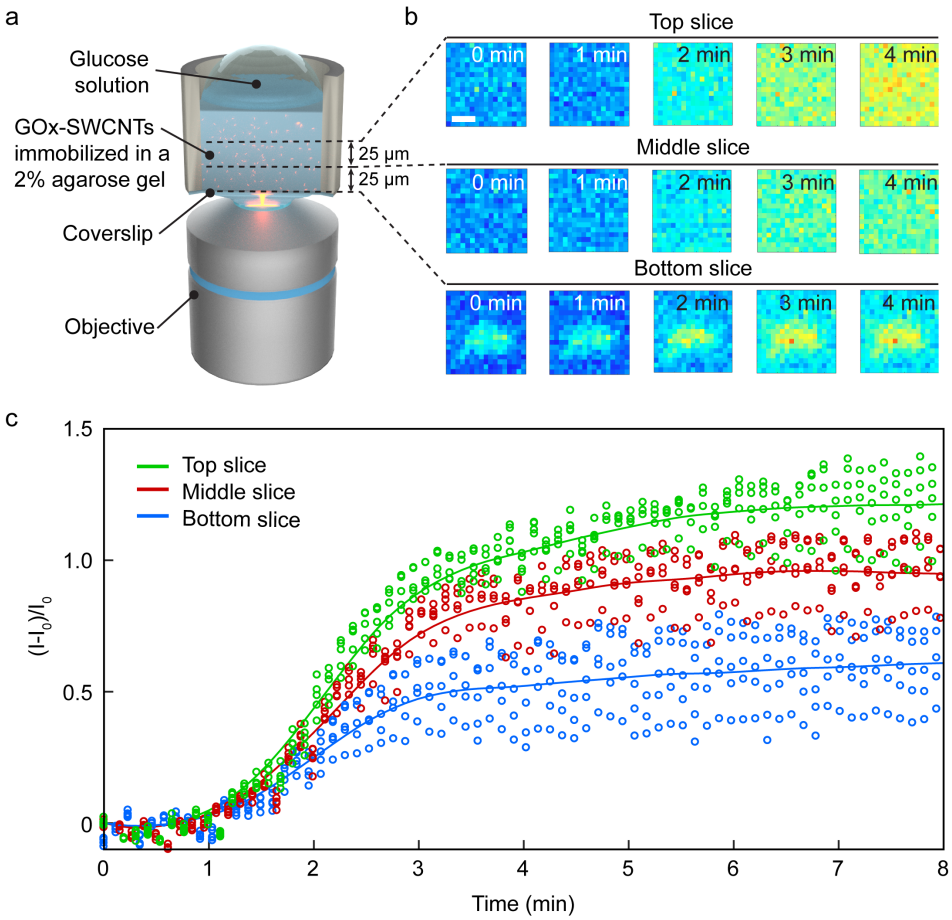

Figure 1.5 – Spatiotemporal response of immobilized GOx-SWCNT sensors to glucose. **(a)** Schematic of the setup. GOx-SWCNTs sensors were embedded in a 2% agarose gel within a glass-bottom well. **(b)** Confocal planar images (step size = 25 µm) of representative clusters with NIR fluorescent GOx-SWCNTs (excitation at 660 nm, emission above 980 nm). The observed fluorescence increase of the GOx-SWCNT sensors over time was triggered by adding enough glucose solution to yield a final concentration of 15 mM. Scale bar = 2.5 µm. **(c)** Normalized $(I - I_0)/I_0$ fluorescence intensity change of five GOx-SWCNT clusters from each axial position after addition of glucose (empty circles), where I is intensity and I_0 is initial intensity. The lines show average intensity changes at the top (green), middle (red), and bottom (blue) slices after applying locally weighted scatterplot smoothing (LOWESS).

implanted SWCNT sensors are measured despite gel diffusion limitations that may contribute to a heterogeneous SWCNT response. Minimizing this heterogeneity through facilitated diffusion can therefore improve sensor response. The spatiotemporal distribution of SWCNTs has been studied previously, for example, by *Galassi et al.*, who imaged SWCNTs distributed within an agarose gel [108]. However, monitoring of the sensor response in 3D, particularly in the axial direction, has not yet been reported. We therefore performed in situ glucose monitoring within a 120 µm × 100 µm × 50 µm gel sample containing GOx-SWCNT sensors in a 2 wt% agarose gel (**Figure 1.5a**). The GOx-SWCNT sensors were continuously excited with a 660 nm laser, and the fluorescence intensity of the sensors was monitored over multiple confocal planes to track the permeation of glucose in the axial direction. The fluorescence

intensity of GOx-SWCNTs in all confocal planes ultimately increases in response to the addition of 15 mM glucose (**Figure 1.5b, c**). Provided that the size of a glucose molecule (3.6 Å [109]) falls well below the average pore size of the agarose gel (~120 nm for 2% agarose gel), the matrix is expected to allow the glucose molecules to freely diffuse in the gel [110]. Assuming a diffusion coefficient of 5.73×10^{-10} m^2 s^{-1} [111], the glucose diffusion time through a 50 µm layer of an agarose gel is ~2.2 s, which is expected to occur within one complete scan in the axial direction (the integration time for a single frame is 0.5 s; the Z-stack acquisition time is 4.6 s). The continuous diffusion of glucose from the surface into the gel creates a concentration gradient along the axial direction, as shown in **Figure 1.5c**, which illustrates the NIR fluorescence increase at the top, middle slice, and bottom slices, consecutively. Although axial tracking of glucose permeation can be achieved through larger step sizes in the wide-field configuration, the spinning-disc confocal NIR microscope reduces the thickness of the sectioning by factor of ~2, allowing more precisely controlled and localized SWCNT imaging in the axial direction.

1.5 Conclusion

In addition to the conventional wide-field setup for spectroscopy, we developed a spinning-disc confocal setup designed for imaging in the NIR-II window. This confocal setup shows a ~17% and ~45% enhancement in lateral and axial resolutions, respectively, achieving a lateral resolution of 0.5±0.1 µm and an axial resolution of 0.6±0.1 µm. The enhancement in the resolution allows more precise visualization of NIR nanoparticles within biological structures as small as plastids or bacterial cells. Confocal images of ssDNA-SWCNTs internalized in a single chloroplast reveal an inhomogeneous, granular distribution of nanoparticles in the organelle. This setup was also used to track the Brownian motion of NIR fluorescent beads in 0, 25, 50, and 75 v/v% aqueous glycerol solutions in wide-field and confocal modes. The diffusivities calculated from both modes fall within the range of expected theoretical diffusivities, with the diffusivities calculated from the wide-field measurements further underestimating the diffusion coefficient compared to those calculated from the confocal measurements. This discrepancy may arise from the thicker imaging plane of the wide-field setup, which accounts more for movement in the axial direction. Finally, the setup was also used to image the axial permeability of an analyte, in this case, glucose, by monitoring the NIR fluorescence response of immobilized sensors within a gel matrix.

To further improve the spatial resolution and overcome the Abbe diffraction limit, the confocal system can be combined with Image Scanning Microscopy (ISM). *Azuma and Kei* demonstrated that the conventional spinning-disc confocal microscope can be combined with ISM to improve the lateral resolution over the wide-field by 27% [112]. In this work, the setup achieved a 17% increase in lateral resolution in the NIR light region, which could be enhanced using ISM as well as deconvolution of the point spread function (PSF). The NIR confocal imaging of photostable SWCNTs is suited for the extended acquisition times required for ISM (typically 1 to 25 s per frame) and would profit from the NIR transparency of biological tissues [113].

Future improvements to the setup also include placement of a piezoelectric axial positioning stage instead of the motorized stage, which is expected to increase the z-sectioning speed and resolution. Also, NIR sensors with greater QY will reduce the image acquisition time and take advantage of the higher frame rate achievable by the NIRvana camera. These improvements are particularly beneficial for applications that require local analyte detection within or on a cell, such as the detection of local dopamine release in axons.

Nonetheless, the three demonstrations highlighted with the current configuration illustrate the use of the setup for applications that require not only increased resolution of NIR particle distribution, but also NIR tracking of moving nanoparticles and axial tracking of analytes within immobilized 3D matrices. Though these three demonstrations provide only a glimpse of the possible applications unlocked with a NIR SDCLM, they lend a convincing basis for expanded studies on spatiotemporal monitoring for *in vitro* and *in vivo* imaging and sensing that include, for example, transient nanoparticle uptake and localization measurements in living cells and biological tissue.

2 Mediator-free optical GOx-SWCNT glucose sensor

This chapter consists of an article published in Small with the title: ***Mediatorless, reversible optical nanosensor enabled through enzymatic pocket doping*** *[19]. The co-authors of this article are: N. Schuergers, B. Lambert, E. Ahunbay, and A. A. Boghossian.*
(DOI: 10.1002/smll.201701654)

Author contributions: *V.Z., N.S., and A.A.B. participated in experimental design. B.L. performed continuous glucose monitoring experiment in a buffer and E.A. performed a colorimetric assay with saccharides. V.Z. performed the rest experiments. V.Z., N.S., and A.A.B. wrote the manuscript. V.Z. and A.A.B. conceived and designed the research.*

2.1 Abstract

The custom-built, NIR-II setups described in **Chapter 1** allow us to characterize the NIR emissions from optical sensors based on SWCNTs. The intrinsic SWCNT fluorescence benefits from indefinite photostability and tissue transparency, offering a promising basis for *in vivo* biosensing. Existing SWCNT optical sensors that rely on charge transfer for signal transduction often require exogenous mediators that compromise the stability and biocompatibility of the sensors. This chapter presents a reversible, mediatorless, near-infrared glucose sensor based on GOx-SWCNTs. GOx-SWCNTs undergo a selective fluorescence increase in the presence of aldohexoses, with the strongest response toward glucose. When incorporated into a custom-built membrane device, the sensor demonstrates a monotonic increase in initial response rates with increasing glucose concentrations between 3 and 30 mM and an apparent Michaelis–Menten constant of $K_{M(app)} \approx 13.9$ mM. A combination of fluorescence, absorption, and Raman spectroscopy measurements suggests a fluorescence enhancement mechanism based on localized enzymatic doping of SWCNT defect sites that do not rely on added mediators. Removal of glucose reverses the doping effects, resulting in full recovery of the fluorescence intensity. The cyclic addition and removal of glucose is shown to successively enhance and recover fluorescence, demonstrating reversibility that serves as a prerequisite for continuous glucose monitoring.

2.2 Introduction

In the absence of a cure, patients who suffer from diabetes must continuously monitor their blood glucose to minimize the risk of complications. Though glucose test strips offer the most widespread approach to determining blood glucose levels, they require significant patient involvement in withdrawing blood, determining insulin doses, and administering insulin injection intermittently throughout the day. The next generation of technologies include automated mechanisms for glucose management, such as glucose-responsive insulin delivery patches and closed-loop control systems that couple continuous glucose detection with automated insulin injections [114–121]. Despite significant strides made in implementing closed-loop systems in patients, widespread commercialization is limited by continuous glucose sensors that suffer from short lifespans, tedious calibrations, instability, and/or high costs [47, 49, 122].

One approach to overcoming these challenges is to engineer a continuous glucose sensor that benefits from the advantageous optical properties of semiconducting SWCNTs. Semiconducting SWCNTs fluoresce in the NIR region where the absorbance of biological tissue and biofluids, such as blood, is minimal, enabling implantable sensors for *in vivo* measurements [123]. The indefinite photostability of these fluorophores is particularly advantageous for blood monitoring as it allows for continuous and quantitative measurements over an extended lifespan. Optical SWCNT-based sensors have demonstrated single-molecule sensitivity limits, and they have been used to detect a variety of analytes, such as H_2O_2, NO, dopamine, insulin, ribonucleic acids, and glucose [6, 13, 58, 103, 124, 125].

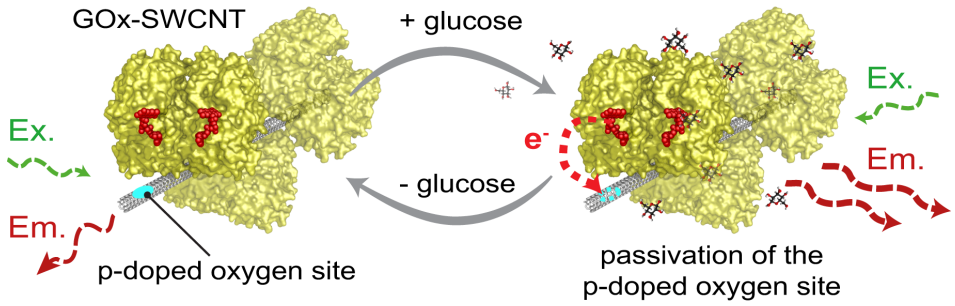

Figure 2.1 – Schematic of sensing mechanism for GOx-SWCNTs. GOx-functionalized SWCNTs (GOx-SWCNTs) demonstrate an intrinsic NIR fluorescence emission upon illumination (left). The presence of oxygenated p-doped sites, shown in blue, decreases fluorescence emission. Glucose reacts with GOx, and the extracted charge from glucose oxidation passivates the oxygenated site through localized n-doping of the SWCNT surface (right). This passivation yields an increase in NIR fluorescence intensity. Fluorescence is reversibly recovered through the removal of glucose.

Several optical SWCNT-based sensors have already been developed for measuring blood glucose [13, 42, 58, 123]. Despite significant advancement, these sensors suffer from limited reversibility and/or analytical range needed for physiological measurements [122], two figures of merit that are essential for continuous glucose monitoring [126]. In this study, we develop a SWCNT-based optical sensor that is capable of reversibly detecting physiological

concentrations of glucose. In contrast to the previous sensors, reversible glucose detection is observed in the absence of added constituents for regenerating the sensor and without the need of exogenous mediators for facilitating charge transfer. Protein-based pocket doping is responsible for a charge-mediated response within a protein-nanoparticle system with overall unfavorable redox matching. To the best of our knowledge, this previously unreported sensing mechanism, shown in **Figure 2.1**, obviates the need to engineer systems with favorable overall redox matching, enabling a new approach to creating reversible optical sensors.

2.3 Materials and methods

Preparation of SC suspended SWCNTs. SWCNTs (50 mg, CoMoCAT, SWeNT SG65i, batch MKBN5945V, Sigma Aldrich) were suspended in 50 mL of 2 wt% SC (Sigma Aldrich) in PBS (pH 7.4, gibco, Life Technologies). The suspension was sonicated for 30 min using a probe-tip ultrasonicator (1/4 in. tip, Q700 Sonicator, Qsonica) at 10% amplitude in an ice bath. The sonicated SWCNT suspension was centrifuged at 30 000 rpm (164 000 × g) for 4 h at room temperature using an Optima XPN-80 Ultracentrifuge (Beckman Coulter) to remove SWCNT aggregates. The supernatant was collected for further processing and analysis.

SWCNT surface activation with GOx. 30 mg of GOx from *A. niger* (batch SLBN9716V, Type II, 19 440 U g^{-1}, Sigma Aldrich) was dissolved in 1 mL of the SC-suspended SWCNT solution and stirred for 2 h at room temperature. The suspension was transferred to wet dialysis tubes with a 14 kDa MWCO (cellulose membrane, D9777, Sigma Aldrich) and dialyzed against PBS (1.5 L, pH 7.4) for 4 h at room temperature to remove SC. The SC removal facilitates the nonspecific adsorption of GOx. The GOx-SWCNT solution was subsequently transferred to a 300 kDa MWCO dialysis device (Spectra/Por Float-A-Lyzer, Spectrum Laboratories) and dialyzed overnight at room temperature against PBS (1.5 L) to remove unbound enzyme. The final concentration of SWCNTs as determined through UV–vis–NIR spectrophotometry (UV-3600 Plus, SHIMADZU) was between 16 and 22 mg L^{-1} (ϵ_{739nm}= 25.3 mL mg^{-1} cm^{-1}) [127]. The GOx-SWCNT suspension was stored at 4 °C and equilibrated to room temperature before measurements.

Colorimetric GOx activity test. An established colorimetric assay adapted from *Keston et al.* was used to measure GOx activity in response to different saccharides in a 96-well plate [128]. The colorimetric assay relies on the enzymatic catalysis of H_2O_2 and subsequent oxidation of a dye (o-dianisidine). Briefly, GOx (7 µL, 30 mg mL^{-1}), o-dianisidine (173 µL, 1%, Sigma Aldrich), and horseradish peroxidase (7 µL, 60 U mL^{-1}, HRP, Type-VI-A, Sigma Aldrich) in PBS at pH 6.0 were mixed in a 96 well plate and incubated at 36 °C for 20 min. After incubation, 13 µL of each 30 mM saccharide solution, D-glucose (β-D-glucose, AB 136302, ABCR GmbH & CO. KG), D-mannose (99%, ABCR GmbH & CO. KG), D-galactose (98%, ABCR GmbH & CO. KG), D-maltose monohydrate (>99.0%, Sigma Aldrich), D-fructose (>99.0%, TCI Deutschland GmbH), and D-xylose (>98.0%, TCI Deutschland GmbH) were added to each well, and absorption measurements were taken after 2.5 min at 500 nm in 96 well plate reader (Varioskan

LUX, Thermo Scientific). The absorbance of controls performed in the absence of GOx was subtracted from each measurement.

NIR microspectrometric setup. A custom-built microspectrometer was used for the NIR detection of SWCNT fluorescence. The setup consists of a supercontinuum laser source and a tunable band-pass filter unit (SuperK Extreme EXR-15 and SuperK Varia, NKT Photonics) that operates between 400 and 830 nm at a pulse frequency of 80 MHz. A short-pass filter (890 nm blocking edge BrightLine, Semrock) was used to remove NIR reflections. The excitation light is directed into a 20x objective (M Plan Apo NIR, NA 0.4 air, Mitutoyo Corporation) using silver-coated mirrors and a dichroic reflector (LP 830 nm, Semrock), resulting in an illumination spot of 350×350 µm. Light emitted from the sample is collected in the epi-direction and focused onto the entrance slit of an IsoPlane SCT- 320 spectrometer (Princeton Instruments). A 70 lines mm^{-1} grating was used to disperse the light, which is redirected into an InGaAs NIR camera (NIRvana 640 ST, Princeton Instruments). Measurements were recorded with LightField (Princeton Instruments) and custom-built LabView (National Instruments) software. The optical system was calibrated with a NIR calibration source (HL-3plus-CAL-EXT, Omicron Optics) prior to measurement, and wavelength calibration was performed using characteristic lines of a mercury lamp (IntelliCal, Princeton Instruments).

Active and deactivated sensor response to different saccharides. For the inactivated GOx measurements, GOx in PBS (30 mg mL^{-1}) was heated to 62 °C for 15 min to denature the secondary and tertiary structure of the enzyme [129]. This denaturation was followed by the same two-step dialysis procedure discussed above.
SWCNT fluorescence measurements were performed in 96-well plates with 50 µL of the active GOx-SWCNT suspensions mixed with 50 µL of PBS or 30 mM saccharide in PBS. The NIR spectra were recorded after 3 min by illuminating samples with a 575±5 nm laser and collecting the NIR emission using the aforementioned setup. The (6,5) SWCNT peak maxima were normalized to the PBS control ($(I - I_{PBS})/I_0 \times 100\%$).

Membrane device measurements. 100 µL of PBS was added to the top compartment of the device while the bottom sensing compartment (volume ~15 µL) was illuminated from below with a 575±5 nm laser. After 16 min, the PBS solution was exchanged with 100 µL of 30 mM glucose in PBS. For the sensor kinetic response measurements, the glucose solution in the top compartment was exchanged with PBS, and the procedure was repeated. Fluorescence spectra were taken throughout this process. As GOx activity does not vary significantly with temperature over the range of 20-40 °C [130], all measurements were carried out at room temperature (~22 °C). The fluorescence signal of the sensor was fully recovered after each measurement by rinsing the membrane and incubating with PBS for 25 min.

Absorbance spectroscopy. Absorbance spectra were taken between 300 and 1400 nm using a UV-vis-NIR spectrophotometer (UV-3600 Plus, SHIMADZU). Measurements were carried out in a 500 µL quartz cuvette (10 mm, Quartz SUPRASIL, Hellma Analytics). Spectra were taken before and 20 min after addition of glucose (1 µL, 3.5 M, in PBS) to 500 µL of GOx-SWCNTs

and GOx in PBS (15 mg mL^{-1}).

Raman spectroscopy. GOx-SWCNT (50 µL) was loaded into a 1 mm channel with openings on both sides, a cover glass on top, and a glass slide on the bottom. Raman spectra were recorded at an excitation wavelength of 532 nm and laser power of 3.7 mW from 100 to 1700 cm^{-1} using a 5x objective (Leica) on a spectrometer (inVia Raman Microscope, Renishaw). The spectrometer was calibrated before measurements using an internal standard. Background measurements in PBS were subtracted from the spectra. Glucose (0.1 µL, 3.5 M, in PBS) was added to the GOx-SWCNTs from one side of the channel. Spectra were recorded before and after addition of glucose.

Membrane device measurements with human serum. 100 µL of PBS were added to the top compartment of the device while the bottom sensing compartment was illuminated from below with a 575±5 nm laser. After 10 min, the PBS solution was exchanged with 100 µL of 7 mM glucose in PBS (**Figure 2.6**, at time 0 min). After 24 min, the glucose solution was exchanged with PBS, and after another 18 min, the PBS solution was exchanged with 100 µL human serum (H4522, human serum from human male AB plasma, Sigma Aldrich, glucose concentration between 3.3 and 7.8 mM. Fluorescence spectra were taken throughout this process.

2.4 Results and discussion

2.4.1 Fabrication of the GOx-SWCNT sensors

(6,5)-Enriched SWCNTs were functionalized with GOx using a two-step dialysis procedure. In the first dialysis step, SC was removed from a solution of SC-SWCNTs in the presence of GOx to immobilize the enzyme onto the nanotube surface. In this dialysis step, a multifold excess of GOx is added to sufficiently solubilize the SWCNTs (see **Figure B.1**). Immobilization occurs through dialysis-driven surfactant displacement, as modeled in previous studies [103]. Briefly, the SC molecules on the surface of the SWCNTs, which are in dynamic equilibrium with free SC molecules in solution, are continually removed from the solution, resulting in a net desorption of surfactant from the SWCNT surface. Van der Waals forces drives the immobilization of GOx on the exposed, hydrophobic SWCNT surface to yield the formation of an adsorbed protein monolayer, as reported previously [13]. Free GOx was subsequently removed from the suspension through a second dialysis step. Over the course of ~24 h, a single laboratory-scale batch of this synthesis procedure yields ~2 mL of solution, enough to fill over 6 000 of 0.3 µL implantable capillaries [131].

GOx is expected to form a loosely packed corona around the SWCNT, which was verified through both Fourier transform infrared (FTIR) spectroscopy (**Figure 2.2a**) and NIR fluorescence spectroscopy (**Figure 2.2b**). A comparison of FTIR spectra taken before and after corona formation shows the disappearance of the 2930, 1555, and 1416 cm^{-1}SC peaks and the appearance of peaks around 1638, 1618, and 1540 cm^{-1} associated with the amide groups

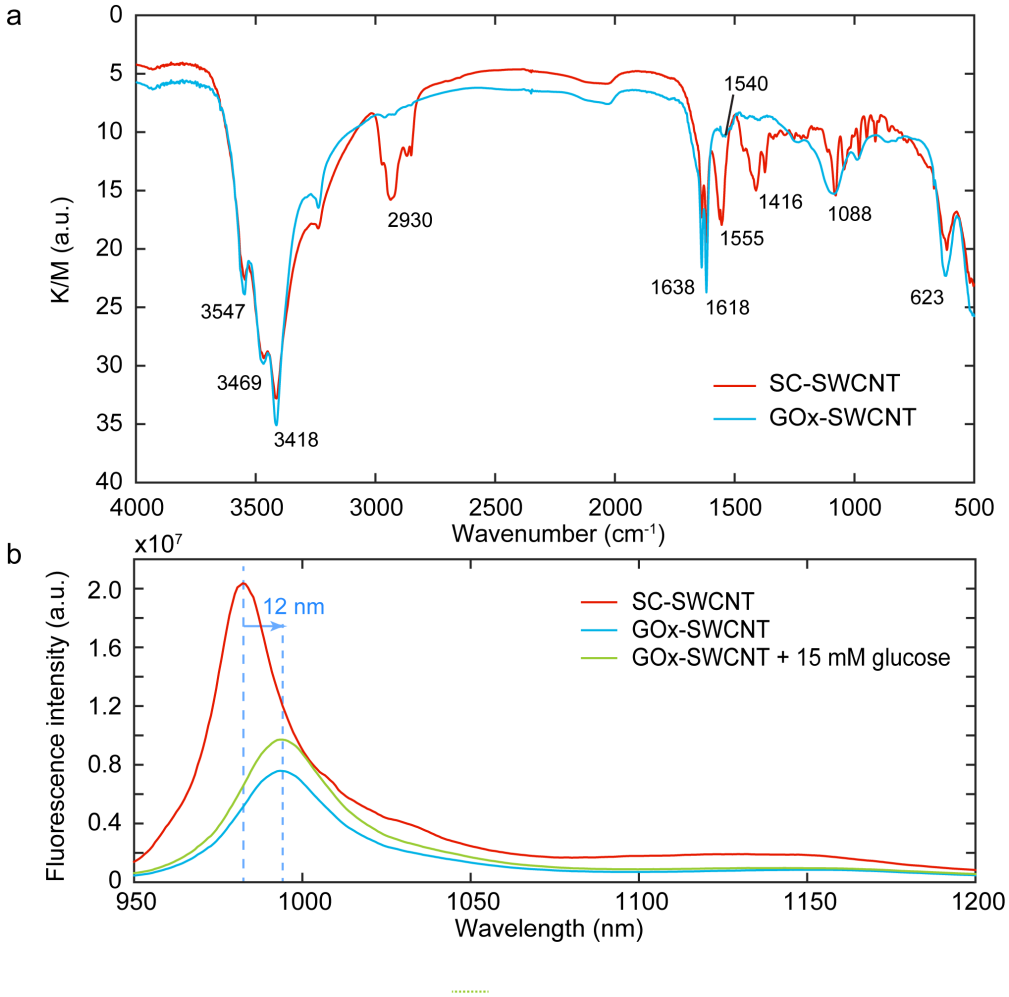

Figure 2.2 – Spectroscopic characterization of GOx-functionalized SWCNTs. **(a)** Kubelka–Munk transformed diffuse-reflectance infrared Fourier-transform (DRIFT) powder spectra of SC-SWCNT (red) and GOx-SWCNT (blue). **(b)** NIR fluorescence spectra for SC-SWCNTs before (33 ± 1 mg L^{-1}, red) and after adsorption of GOx (21 ± 1 mg L^{-1}, blue) and upon the subsequent addition of 15 mM glucose (green).

of the GOx (**Figure 2.2a**) [132]. Compared to the tightly packed SC surface, a GOx-modified surface promotes increased water accessibility that is expected to yield a solvatochromic red-shift of SWCNT fluorescence [13]. In agreement with this theory, a 12 nm red-shift of the (6,5) SWCNT peak was observed after the first dialysis step (**Figure 2.2b**) [22, 23]. The reduced fluorescence observed after GOx functionalization is attributed to the dilution of SWCNTs during dialysis. The results of this spectroscopy analysis is in agreement with those performed in previous studies that have also confirmed protein corona formation through atomic force microscopy (AFM) [13, 133]. The AFM images show monolayer coverage of GOx on SWCNTs following dialysis-driven immobilization.

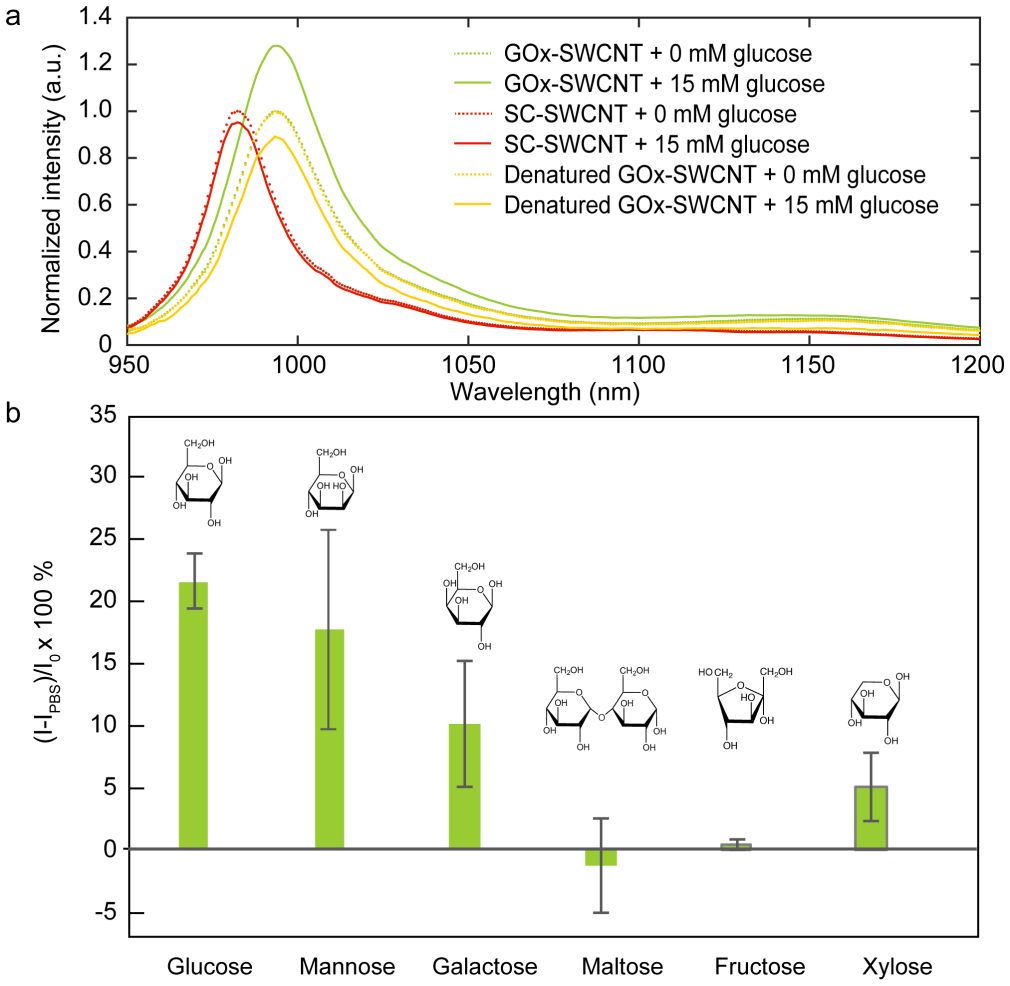

Figure 2.3 – GOx-SWCNT selectivity toward various saccharides. **(a)** Fluorescence intensity of GOx-SWCNTs (green), SC-SWCNTs (red), and thermally deactivated GOx-SWCNTs (yellow) in response to 15 mM of glucose. Fluorescence spectra are normalized with respect to the maximum fluorescence peak in the absence of glucose. **(b)** Changes in normalized fluorescence intensity of GOx-SWCNTs after addition of 15 mM of glucose, mannose, galactose, maltose, fructose, and xylose. Measurements were taken in triplicates for the (6,5) SWCNT peak (emission at 995±1 nm) 3 min after saccharide addition. The values represent the percentage change between the initial I_0 and final I fluorescence intensities of the (6,5) peak after subtracting a PBS background: $(I - I_{PBS})/I_0 \times 100\%$. All measurements were recorded using 575±5 nm laser excitation.

When 15 mM of glucose is added to the GOx-SWCNT suspension, the shifted (6,5) fluorescence peak increases in intensity (**Figure 2.3a**). To verify the enzymatic response, SWCNTs were also functionalized with GOx that had been thermally deactivated prior to surface functionalization (denatured GOx-SWCNT) by incubating the enzyme at 62 °C for 15 min [129]. The denatured GOx-SWCNTs show diminished fluorescence due to aggregation and no fluorescence increase in response to glucose; instead, a slight decrease is observed. Since the increased agglomeration state of the denatured GOx-SWCNT may itself inhibit a glucose response, an additional negative control was run with SC-SWCNTs, which readily disperse in solution. The SC-SWCNT

shows no fluorescence increase in the presence of glucose, but a slight fluorescence decrease can be observed, as in the case of denatured GOx-SWCNT. The observed fluorescence decrease in both cases is largely attributed to the dilution of the SWCNT solution upon glucose addition. The direct addition of analyte to the SWCNT solution increases the solution volume, and the dilution of the SWCNTs results in a slight decrease in fluorescence. As shown in **Figure B.3**, the decrease in fluorescence is statistically insignificant when accounting for the fluorescence decrease due to PBS addition. This fluorescence decrease is not observed when glucose is administered through the membrane setup shown in **Figure 2.4a**, in which the SWCNT concentration remains constant. Though a fluorescence decrease is also likely present in the positive control measurements, the dilution effects appear masked by the increase in fluorescence due to glucose sensing. Taken together, these results show that GOx presence is essential for a response, and that this response can be attributed to enzymatic activity.

2.4.2 Selectivity of the GOx-SWCNT sensors

Table 2.1 – GOx selectivity toward various saccharides in literature, and as measured in this study based on a horseradish peroxidase (HRP)/o-dianisidine colorimetric assay

Saccharide	**Relative reactivity in %**			
	Ref. [134]$^{(a)}$	**Ref. [135]**$^{(b)}$	**Ref. [136]**$^{(c)}$	**In this study**
Glucose	100	100	100	100
Mannose	0.98	-	3	11 ± 2
Maltose	-	1	-	1 ± 1
Galactose	0.14	-	0	7 ± 2
Fructose	-	-	-	1 ± 1
Xylose	-	3	0	11 ± 2

$^{(a)}$Colorimetric, pH 5.6, 20 °C; $^{(b)}$Colorimetric, pH 5.0, 37 °C;
$^{(c)}$Electrochemical, pH 7.0, 25 °C.

To investigate the selectivity of the sensor's response to glucose, NIR fluorescence spectra of the GOx-SWCNT suspension were recorded before and 3 min after the addition of six selected saccharides: glucose, mannose, galactose, maltose, fructose, and xylose (spectra shown in **Figure B.5**). A comparison of the normalized fluorescence shows that the fluorescence intensity of GOx-SWCNTs increases by 22±2% after the addition of glucose. A smaller increase is detected for mannose (18±8%), galactose (10±4%), and xylose (5±3%), while no significant change was observed for maltose (-1±4%) and fructose (1±1%) (**Figure 2.3b**). The fluorescence response toward these saccharides is in agreement with the substrate specificity determined in a colorimetric assay for free GOx and with previous reports on the GOx-catalyzed oxidation of different saccharides (**Table 2.1**) [134, 137]. These observations indicate that the sensor's selectivity is conferred by the affinity of GOx toward specific saccharides. In addition, a comparison of the catalytic efficiency shown in **Figure B.4** shows that although mannose is catalyzed to a measureable extent, its catalytic turnover is over 20 times slower than that of

glucose, requiring over an hour of incubation to achieve a fraction of the activity achieved in 3 min with glucose. This observation is in agreement with previous reports of GOx having a k_{cat}/K_M for mannose that is 42 times smaller than that of glucose [138], and it is conferred by the preferred oxidation of glucose in the presence of other sugars [139–141]. This catalytic selectivity, combined with the fact that hexoaldose concentrations of competing sugars are typically two orders of magnitude below that of glucose, indicate adequate glucose specificity of the GOx-SWCNT sensors for *in vivo* applications [142, 143].

2.4.3 Reversible glucose monitoring using the GOx-SWCNT sensors

To characterize the sensor's kinetics and reversibility, GOx-SWCNTs were incorporated into the custom-made membrane device shown in **Figure 2.4a**. The device consists of two compartments separated by a 14 kDa MWCO membrane that remains permeable to glucose while retaining the GOx-SWCNTs in an enclosed volume. The bottom of the device is a glass slide that is transparent to excitation and emission wavelengths. This device is in many ways similar to the porous dialysis capillaries or small diameter dialysis tubing previously used to enclose SWCNT sensors [13], but in this case, the sensor is confined between the membrane and an optically transparent window for enhanced light transmission. The sensor is continuously excited with a 575±5 nm laser, and the (6,5) chirality emission peak (995 ± 1 nm) is recorded in the epi-direction.

The addition of 30 mM glucose to the top compartment of the sensor device leads to an increase of the (6,5) fluorescence intensity, approaching a maximum increase of 32% after 12 min (**Figure 2.4b**). The concentration dependence of this kinetic response was monitored over 25 min in the presence of glucose concentrations ranging between 0 and 30 mM. These measurements were done with the same device, which was washed between measurements (**Figure 2.4c**). The sensor even showed a discernible response toward the lowest glucose concentration tested (3 mM), requiring a sensor response time of up to 15 min over the range of glucose concentrations tested. The addition of glucose results in a sigmoidal increase of fluorescence over time, ultimately achieving a maximum normalized intensity change of about 37% for 10, 20, and 30 mM glucose and 10% for 3 mM glucose. The rate of the fluorescence change increases with higher glucose concentrations, with rates of 0.009, 0.034, 0.047, and 0.060 min^{-1} observed for 3, 10, 20, and 30 mM glucose additions (see **Figure B.7** on the calculation of the rates).

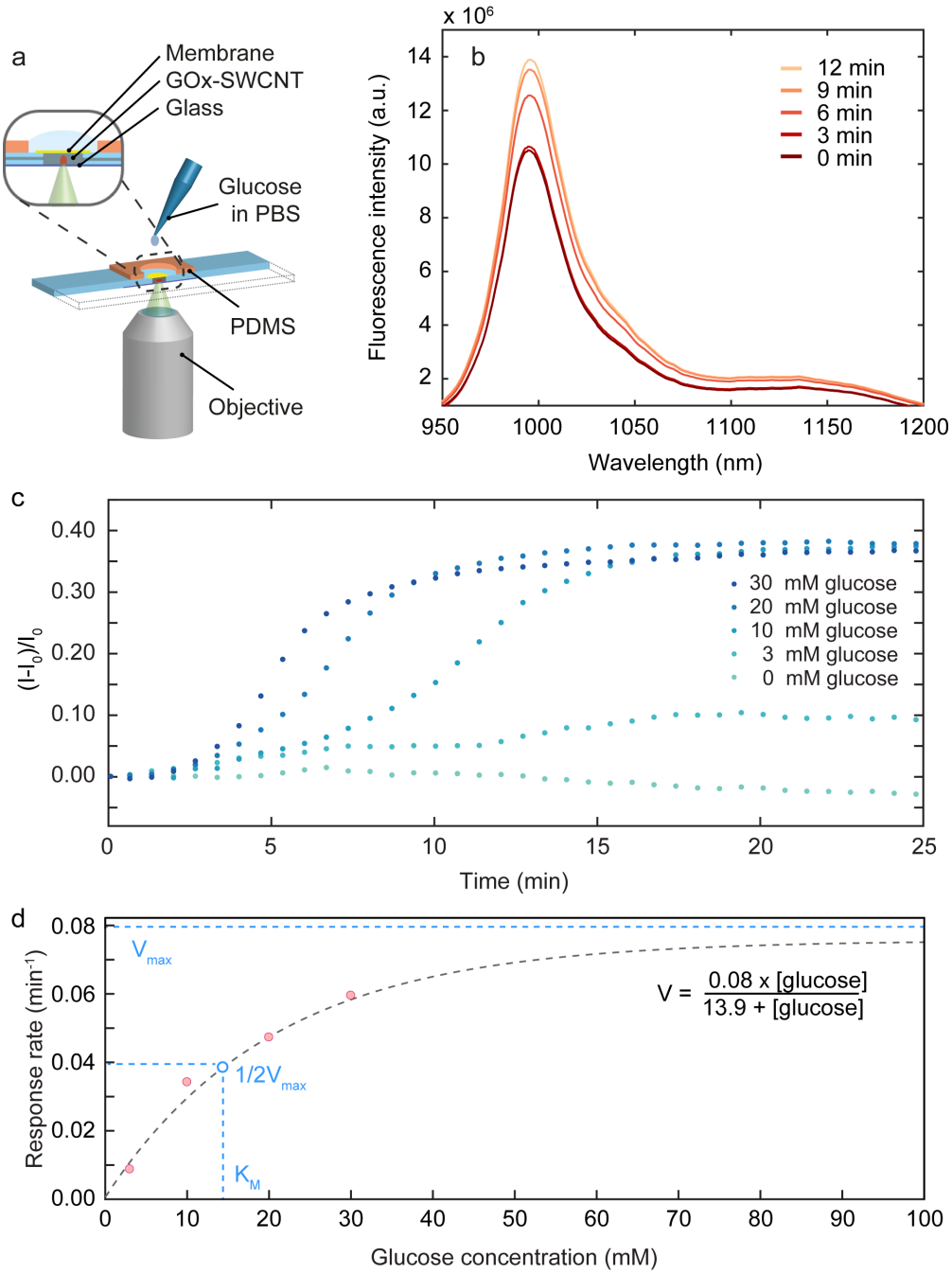

Figure 2.4 – Kinetic response of GOx-SWCNTs toward glucose. **(a)** The measurement device consists of a sensing compartment between a glass surface and a 14 kDa MWCO membrane containing a GOx-SWCNT solution (21 ± 1 mg L^{-1}) and a PDMS mold on top of the membrane for the addition of analyte or washing solutions. The sensing compartment is illuminated from below with an excitation source (575 ± 5 nm), and NIR emission is collected in the epi-direction. **(b)** GOx-SWCNT fluorescence spectra recorded 0, 3, 6, 9, and 12 min after administration of 30 mM glucose onto the semipermeable membrane. **(c)** Intensity changes of GOx-SWCNT (6,5) fluorescence (emission 995 ± 1 nm) over time after addition of 0, 3, 10, 20, and 30 mM glucose. Intensity I was normalized against the initial intensity I_0: $(I - I_0)/I_0$. **(d)** The response rate of the sensor is calculated from the maximum rate of fluorescence intensity change for each of the glucose concentrations shown in (c).

A plot of the sensor response rate as a function of substrate concentration shows a Langmuir-like concentration dependence of the sensor's response rate toward glucose (**Figure 2.4d**). These flux-based measurements provide a quantitative basis for glucose detection that is comparable to previous glucose sensors [144, 145]. Such flux-based sensors, including electrochemical sensors widely used for glucose sensing, do not measure glucose directly. As mentioned by *Barone et al.*, these sensors instead measure the flux of glucose from a limiting membrane [42]. In this setup, the change in glucose concentration in the sensing compartment can be attributed to glucose permeation across the membrane and its subsequent reaction with GOx. Assuming 1D diffusion in the epi-direction (z-direction) perpendicular to the device membrane, the corresponding change in glucose concentration is captured by the equation:

$$\frac{\delta[glucose]}{\delta t} = D\frac{\delta^2[glucose]}{\delta z^2} + R \tag{2.1}$$

where $[glucose]$ is the glucose concentration, D is the diffusion coefficient of glucose, R is the reaction rate of glucose consumption, and t is time. Glucose must diffuse from the top compartment, across the membrane, and into the sensing compartment to trigger a response. Since the molecular weight of glucose is two orders of magnitude below the MWCO of the membrane, a uniform bulk diffusivity of $D \approx 10^{-6}\,\mathrm{cm^2\ s^{-1}}$ can be assumed in this system [146].

We consider three primary factors that may affect enzymatic response in the sensing compartment: diffusion of glucose into the GOx-SWCNT compartment, diffusion of oxygen across the air–liquid and membrane interfaces to the GOx-SWCNT, and the reaction kinetics of immobilized GOx with the substrate. In the absence of a membrane, a saturating fluorescence response is achieved within 1 min (see **Figure B.6**), while 15-20 min are required to approach a saturated response toward the same concentration of glucose in the membrane setup (**Figure 2.4c**). If we consider the former to be a well-mixed system not limited by glucose or oxygen diffusion through the membrane, these results suggest that diffusion plays a major role in determining the sensor response kinetics. Additionally, GOx reaction kinetics may be reduced by the orientation of GOx on the SWCNT surface, inhibiting access to the active site of the adsorbed protein and reducing catalytic activity.

Oxygen is needed for the re-oxidation of GOx and a continuous catalytic turnover of glucose. Previous reports have shown GOx-carbon nanotube electrochemical sensors to be unresponsive toward glucose in oxygen-free ($<5 \times 10^{-6}$ M) environments [147]. Under atmospheric pressure, the expected oxygen concentration is 0.7×10^{-3} M [137], which is one order of magnitude below the glucose concentrations added to the device. The sensor is therefore sensitive to both glucose and oxygen diffusion limits, and we hypothesize that glucose concentration modulates the flux-based response with oxygen concentration ultimately limiting the maximum intensity achieved.

Despite these limits, the device shows an effective affinity that lies within and above the expected range of healthy blood glucose concentrations in patients (4-8 mM) [47], enabling

a variable, concentration-dependent sensor response over a physiologically relevant range of glucose levels. The Michaelis–Menten constant for non-immobilized GOx measured at room temperature lies between K_M = 23 and 33 mM [148–150], depending on the reaction conditions, and it is reported to be two to three times lower for immobilized enzymes [151, 152]. The overall apparent Michaelis–Menten constant for the sensor device is $K_{M(app)} \approx 13.9$ mM (**Figure 2.4d**), which not only lies within the 7-18 mM range of K_M's reported for immobilized GOx [151–153], but also within the range needed for physiological detection.

The underlying signal transduction mechanism was studied using NIR fluorescence, steady-state absorption, and Raman spectroscopy (**Figure 2.5**). The GOx-SWCNT fluorescence response observed in previous studies occurs *via* a two-step mechanism: electron withdrawal by a mediator ($K_3Fe(CN)_6$) from the highest occupied valence band of the SWCNT followed by subsequent reduction of the mediator by the enzyme product, H_2O_2 [13]. The mechanism depends on the susceptibility of large-diameter SWCNTs to electron withdrawal by $K_3Fe(CN)_6$, which leads to fluorescence quenching that is reversed upon H_2O_2 addition. To study the contribution of these mechanisms to this system, fluorescence changes were compared in the presence of glucose, H_2O_2, and $K_3Fe(CN)_6$ (**Figure 2.5a**). In agreement with previous studies, $K_3Fe(CN)_6$ and H_2O_2 are each shown to independently diminish fluorescence [13, 154, 155]. These results show that the observed fluorescence increase in response to glucose is not due to H_2O_2 formation. A possible contribution from pH was also studied by comparing the solution pH before and after glucose addition. The pH was shown to remain constant at a measured value of 7.25 (within an instrument error of ±0.01). In fact, the fluorescence change observed by varying pH over a wide range of values (from pH 3 to pH 10) is negligible compared to the intensity change observed in the presence of glucose (see **Figure B.8**). These observations suggest that the fluorescence enhancement is not likely due to variations in pH.

Figure 2.5b shows the absorption spectrum of GOx in PBS (15 mg mL^{-1}) with characteristic peaks at 380 and 455 nm corresponding to GOx cofactor flavin adenine dinucleotide (FAD) absorption in the oxidized state [156]. These absorption peaks decrease upon glucose addition as a result of FAD cofactor reduction to $FADH_2$ during the enzymatic cycle summarized below [137]:

$$GOx + glucose \xrightarrow{k_1} GOx_{red} \cdot P \tag{2.2}$$

$$GOx_{red} \cdot P \xrightarrow{k_2} GOx_{red} + P \tag{2.3}$$

$$GOx_{red} + O_2 \xrightarrow{k_3} GOx \cdot H_2O_2 \tag{2.4}$$

$$GOx \cdot H_2O_2 \xrightarrow{k_4} GOx + H_2O_2 \tag{2.5}$$

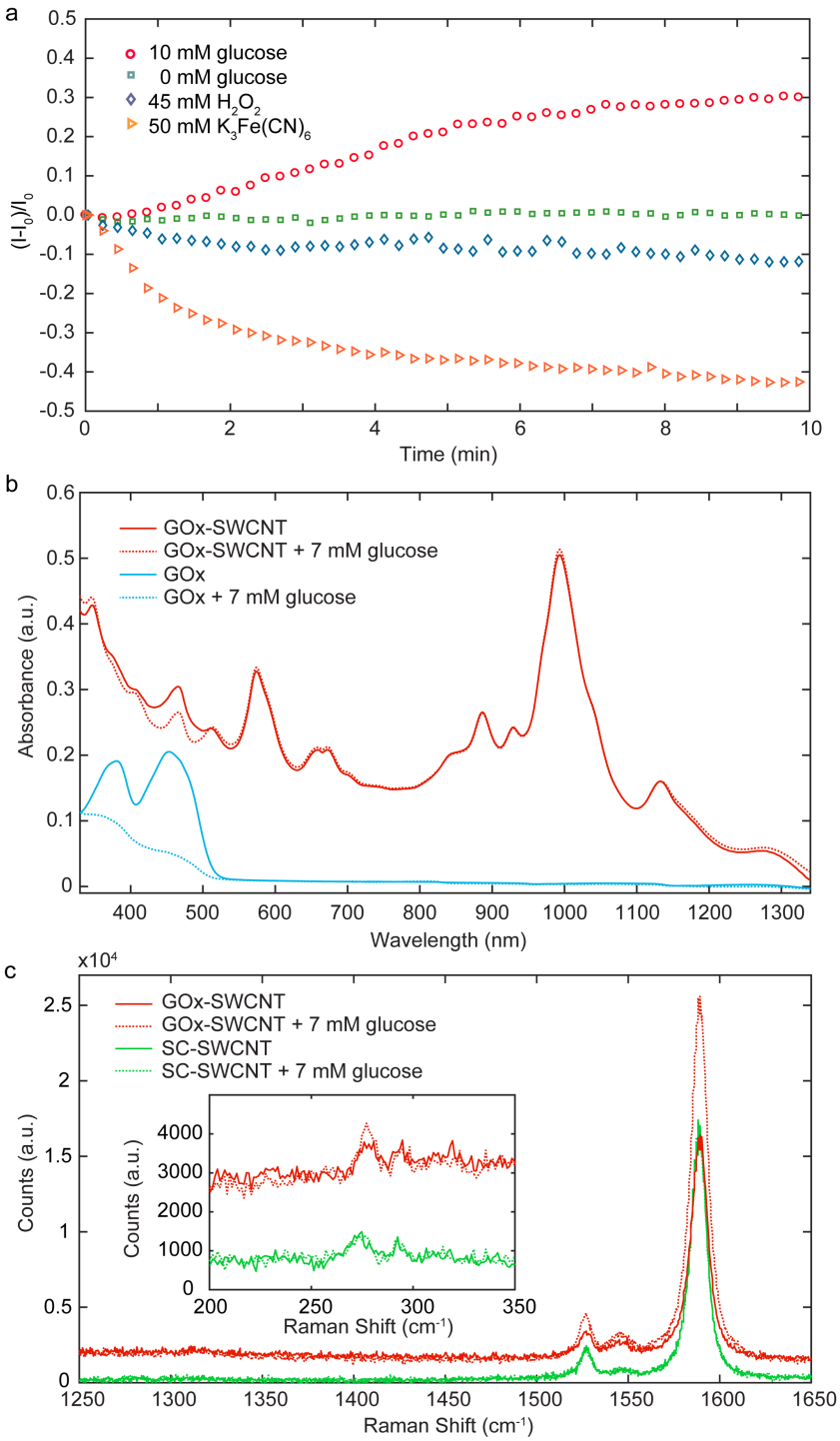

Figure 2.5 – Spectroscopic characterization of the charge transfer mechanism. **(a)** Normalized changes of integrated NIR fluorescence emission of the (6,5) SWCNT (excitation at 575±5 nm, emission at 995±1 nm) over time for GOx-SWCNT in the presence of glucose (red circles), H_2O_2 (blue diamonds), $K_3Fe(CN)_6$ (orange triangles), and in PBS buffer (green squares). **(b)** Absorbance spectra of 15 mg mL^{-1} GOx (blue) and GOx-SWCNT (red) before (solid) and after (dotted) the addition of 7 mM glucose. **(c)** Raman spectra for GOx-SWCNT (red) and SC-SWCNT (green) before (solid) and 15 min after (dotted) the addition of 7 mM of glucose. The insert focuses on the spectral range between 200 and 350 cm^{-1}.

where k_1, k_2, k_3, and k_4 are the reaction rate constants, GOx represents GOx with the oxidized FAD cofactor, GOx_{red} represents reduced GOx containing $FADH_2$, P is the product (gluconolactone), and $GOx_{red} \cdot P$ and $GOx_{red} \cdot H_2O_2$ are reaction intermediates of the reduced and oxidized enzymes bound to their corresponding products, respectively. The semiquinone radical form of GOx, which broadly absorbs between 530 and 650 nm [156, 157], is not observed under these conditions. Similarly, GOx-SWCNTs undergo a decrease in absorption in the region overlapping with FAD cofactor absorption (between 300 and 520 nm) upon glucose addition, indicating that some fraction of the bound enzyme is present in the reduced form after glucose addition.

Direct electron transfer between GOx and SWCNTs, which is the prevailing mechanism reported for electrochemical glucose detection [158], typically occurs through appropriate redox matching. The two-electron reduction potential of the FAD cofactor has been reported to be −0.219 V versus normal hydrogen electrode (NHE) in the unbound state at pH 7.0 [159]. The sensitivity of the FAD reduction potential to its environment is partly responsible for the range of values reported for GOx. A shift from pH 4.5 to 8.5 alone has been shown to vary the GOx reduction potential between −126 and 30 mV versus NHE, with a potential of −97 mV reported for pH 7.4 [156]. Early studies have even reported values as low as −240 mV versus NHE for the semiquinone radical intermediate at high pH that is believed to stabilize the radical anion [157]. Similar variability in reduction potentials have also been reported for SWCNTs, whose redox properties are shown to strongly depend on the SWCNT chirality as well as the SWCNT environment, including the solvent and wrapping molecules used to suspend the SWCNTs. The (6,5) SWCNTs are predicted to have reduction potentials on the order of −480 mV versus NHE [160], and previous electrochemical characterizations of SWCNTs interfaced with GOx have reported reduction potentials of ∼ −480 mV [147]. A large overpotential is often needed for charge transfer, and it is not uncommon to require applied potentials on the order of 400 − 600 mV for the electrochemical detection of glucose using carbon nanotubes [158, 161, 162]. These reports suggest that spontaneous, direct electron transfer from GOx to the (6,5) SWCNT following oxidation of glucose is thermodynamically unfavorable, favoring oxygen as the most likely terminal electron acceptor. In addition, from a kinetic standpoint, an extracted electron from the FAD site of GOx may need to overcome tunneling distances on the order of 15 − 20 Å, which, according to Marcus theory, would result in negligible electron-transfer contributions to the observed response [163].

Since direct electron transfer is unlikely to be the dominating mechanism, we speculate that fluorescence may be altered through the passivation of defect sites on the SWCNT surface that are hole-doped *via* oxygen adsorption [164]. Although the overall SWCNT potential is quite low, the reduction potential of a SWCNT defect site may be as high as 0.8 V versus NHE [165], allowing the catalytically active GOx to serve as a transient reducing agent for these sites. GOx activation with glucose may allow bound GOx to behave as an electron donor to oxygen-induced p-doped sites. Previous studies have shown that these p-doped sites behave as exciton trap sites that decrease SWCNT fluorescence [166, 167]. The addition of reducing agents, such as dithiothreitol, Trolox, and β-mercaptoethanol have been shown to reduce p-

doped defect sites, and this reduction leads to SWCNT brightening [7]. Following an analogous mechanism, transient reduction is achieved in this system through enzymatic doping of these sites, yielding the fluorescence enhancement schematically shown in **Figure 2.1**. Such a mechanism is not only consistent with previous reports of fluorescence enhancement [7], but also with the Raman measurements shown in **Figure 2.5c**. The intensity ratio of the D peak (1360 cm^{-1}) compared to the G peak (1588 cm^{-1}) is a measure of the overall defect state of the SWCNTs [168]. The addition of glucose decreases this ratio from 0.12 to 0.07, suggesting an overall decrease in defect density. The radial breathing mode (RBM) at 277 cm^{-1}, which is a low frequency mode that reflects doping-driven changes in resonance enhancement, also increases by 14% in the presence of glucose [169–171]. Since the adsorption of oxygen induces p-type doping [172], the successive neutralization of defect sites due to the enzymatic activity of GOx may contribute to the observed increase in RBM intensity [171, 173]. In contrast, no changes in RBM intensity or the D to G band ratios were observed for control experiments using SC-SWCNTs.

The reversibility of oxygen doping effects observed in previous studies is consistent with the fluorescence attenuation observed after glucose removal (**Figure 2.6a**) [164]. After addition of 7 mM glucose, the (6,5) SWCNT peak undergoes an increase in fluorescence after 90 s, achieving a normalized intensity change of 8% within 17 min. Removing glucose by replacing the bulk glucose solution in the upper chamber with PBS buffer triggers a fluorescence decrease, leading to complete fluorescence recovery after ~20 min. To evaluate its use for continuous sensing applications, the sensor was subjected to iterative glucose addition and removal cycles (**Figure 2.6b**). The addition of 15 mM glucose on the device membrane results in a fluorescence increase that plateaus after 18 min. As described above, the glucose solution was then replaced with PBS. The fluorescence decreases after 10 min, achieving a baseline fluorescence intensity after 20 min. After recovery of the initial fluorescence intensity, the PBS was replaced again with 15 mM glucose, and the sensor was subjected to an additional recovery cycle. As shown in the figure, the second response and recovery cycle behaves similarly to the first.

To demonstrate the use of this sensor in the presence of complex biological media, the reversibility measurements were also performed in the presence of glucose-containing human serum (3.3 – 7.8 mM). As shown in **Figure 2.6c**, a fluorescence increase is initially observed in the presence of glucose. The replacement of glucose with PBS is shown to decrease the fluorescence, as observed in **Figure 2.6a**. When PBS is subsequently replaced with human blood serum, a fluorescence increase comparable to that observed for glucose is observed. It is noted that a longer incubation time is required to achieve the saturated fluorescence response observed for glucose. This delay is believed to be partly due to decreased diffusivity in the more viscous biological media.

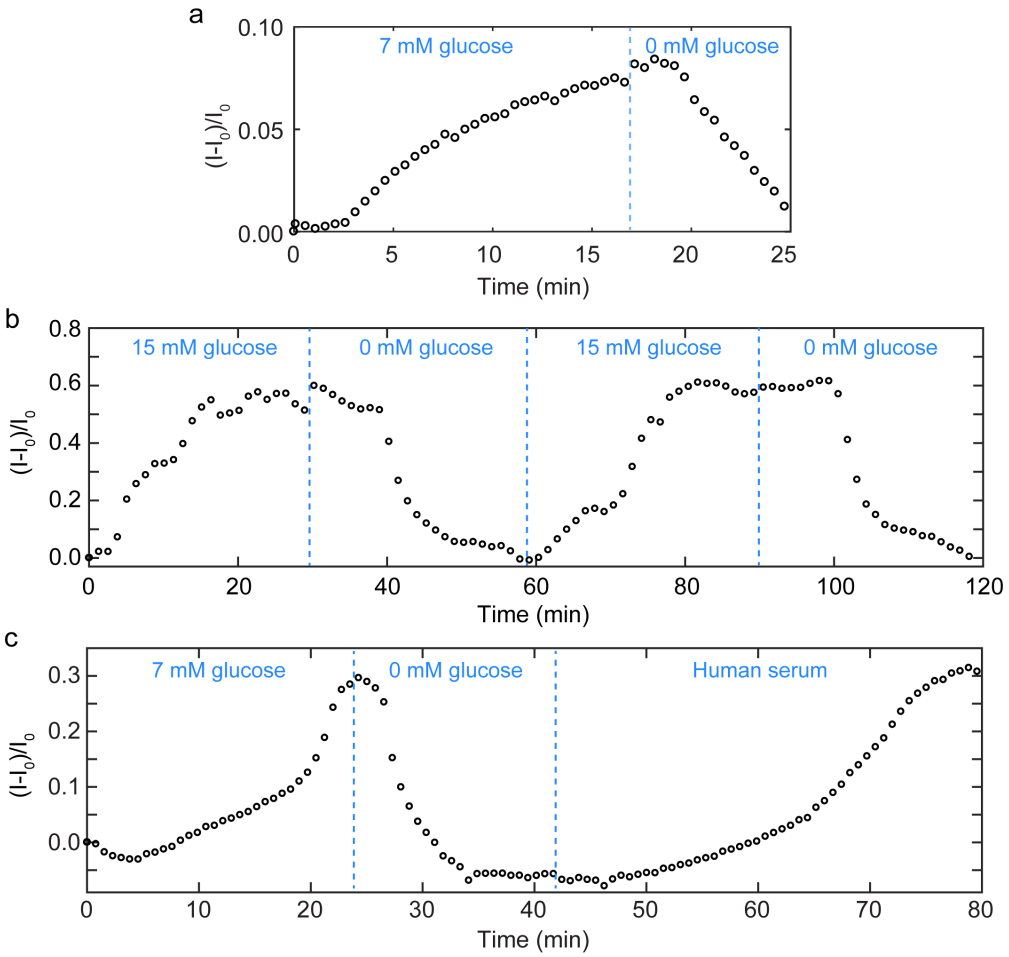

Figure 2.6 – Reversibility of the GOx-SWCNT sensor. (a) Normalized fluorescence intensity increases in the presence of 7 mM glucose. Removal of glucose after 17 min results in a fluorescence decrease. **(b)** Normalized fluorescence intensity is shown to increase and decrease upon the cyclical addition and removal of 15 mM glucose, respectively. All measurements were carried out in PBS (excitation at 575 ±5 nm, emission at 995 ±1 nm). **(c)** Normalized fluorescence intensity increases after addition of 7 mM glucose, decreases upon addition of PBS, and again increases when male human serum containing glucose in AB plasma is added (excitation at 575 ±5 nm, emission at 995 ±1 nm).

2.5 Conclusion

In previous work [13], physiological detection of glucose by GOx-SWCNTs was achieved through the addition of exogenous mediators that allows for favorable redox matching while compromising the reversibility of the system. This work highlights an unexplored optical sensing mechanism based on the localized passivation of oxygenated sites through enzymatic pocket doping. Although pocket doping has been used for electrochemical devices in previous works [174, 175], enzymatic pocket doping, especially with regard to optical SWCNT sensors,

has yet to be reported. Enzymatic pocket doping has been shown to not only enable a response in the absence of added mediators, but also confer sensor reversibility.

Despite these advantages, the sensor has a minimum response time of ~3 min, though up to 15 min can be required to achieve signal saturation. Future endeavors must therefore focus on improving response times to capture fluctuating glucose levels in real time. The current immobilization procedure relies on nonspecific adsorption of GOx onto the SWCNT, resulting in heterogeneity in protein orientation and activity [163]. One approach to enhancing the sensor's response is developing new bioconjugation strategies that not only improve enzymatic activities, but also provide a facilitated pathway for charge transfer between the GOx and SWCNT. In conjunction with improved bioconjugation strategies, techniques such as protein engineering can extend beyond introducing individual attachment sites to altogether reprogramming enzymes to perform optimally in non-native environments. Such biochemical approaches to tuning nanoparticle physics have long proven successful in engineering electronic devices [72], and they serve as a promising avenue for unlocking the coveted continuous, optical glucose sensor.

3 Non-covalent bioconjugation of proteins to SWCNTs

This chapter consists of a manuscript prepared for submission in a journal. The co-authors of this work are: S.-J. Wu, S. Y. Rahnamaee, N. Schuergers, A. A. Boghossian.

Author contributions: *V.Z., S.-J.W. and A.A.B. participated in experimental design. N.S. performed cloning. V.Z. and A.S.R. expressed and purified the proteins. V.Z. performed the experiments. V.Z., N.S., and A.A.B. wrote the manuscript. V.Z. and A.A.B. conceived and designed the research.*

3.1 Abstract

In this chapter, we explore non-covalent functionalization of SWCNTs using proteins through linker molecules. Site-specific immobilization of an enhanced yellow fluorescent protein (EYFP) with a single engineered cysteine residue was performed using either ssDNA or a pyrene-containing linker. Here, we present for the first time a surfactant-exchange method to functionalize SWCNTs by pyrene-protein conjugates. Non-covalent linkage of EYFP and SWCNTs *via* the PM linker was confirmed using absorbance and fluorescence spectroscopies and reformed a time-resolved NIR spectroscopy to analyze adsorption of the proteins onto the SWCNT surface. The site-specific protein immobilization using the PM linker allows achieving higher protein retention on the SWCNT surface in comparison to the ssDNA linker-based approach. Protein immobilization *via* a PM-linker is not limited to specific peptides and could be applied on a wide range of proteins, opening new avenues for engineering biocomposites for optical sensing.

3.2 Introduction

NIR fluorescence and photostability of SWCNTs motivated their use as optical sensors in applications that require long-term sensing in visibly opaque environments, such as *in vivo* monitoring. As sensors, SWCNTs require specificity towards the target analyte. This specificity is achieved through non-covalent surface functionalization that retains the intrinsic nanotube fluorescence. Thus far, optical SWCNT sensors have been non-covalently functionalized with surfactants, lipids, synthetic polymers, oligonucleotides, peptides, and proteins [8, 18, 23, 41, 176]. Proteins, in particular, serve as distinguished molecular recognition elements due to their exceptionally selective interactions with a variety of biomolecules.

Four non-covalent protein immobilization methods for SWCNTs have been reported to date. The first method is direct protein adsorption onto the nanotube sidewall [22, 23]. Despite the simplicity of this approach, the degree of functionalization is protein-specific and depends in part on the hydrophobicity of the protein's surface [24]. Moreover, the adsorption can disrupt protein conformation, leading to a significant reduction in activity [25–27]. Two other functionalization methods include surface adsorption of synthetic polymers [177, 178] or ssDNA followed by conjugation to the amine groups of a protein. Chemical modifications of the adsorbed polymers can populate the nanotube surface with functional groups that can accommodate a large number of proteins. Disadvantages of these approaches include low protein conjugation efficiency and subsequent interactions of the polymer with certain analytes, ions, or its backbone that could interfere with protein-analyte or protein-SWCNT interactions [8, 29, 179]. The last method includes protein conjugation to a pyrene-containing linker that can stack onto the SWCNT surface through $\pi - \pi$ interactions [18–21]. Thus far, this approach has been used to conjugate gold nanoparticles to SWCNTs [180] and detect biomolecule interactions electrochemically [30, 31]. Few studies have used pyrene linkers to conjugate proteins to SWCNTs [30, 31, 35]. However, these studies rely on non-specific conjugation to amines that are populated on the protein surface, and they have yet to demonstrate optical detection.

In this chapter, we perform site-specific immobilization of a bioengineered EYFP, a model fluorescent protein, onto a SWCNT through bioconjugation of cysteine residues located on the amino-terminus (EYFP(N)-Cys) or carboxy-terminus (EYFP(C)-Cys) of the protein. We compare two immobilization schemes based on bioconjugation to a chemically modified ssDNA wrapping (EYFP-ssDNA-SWCNT in **Figure 3.1a**) and to an adsorbed pyrene linker, PM (EYFP-PM-SWCNT in **Figure 3.1b**). Both immobilization procedures rely on non-covalent interactions of the ssDNA or PM to the SWCNT surface, retaining the sp^2 lattice of the nanotube and the SWCNT autofluorescence intact.

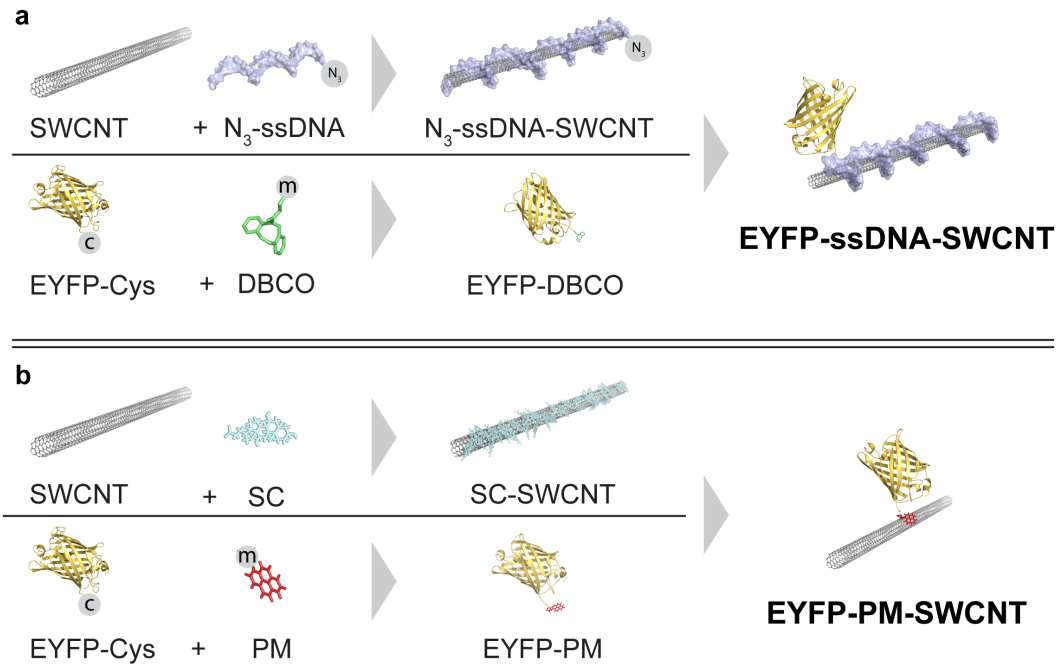

Figure 3.1 – Site-specific, non-covalent immobilization of EYFP onto SWCNTs. **(a)** SWCNTs were wrapped with ssDNA containing a reactive azide functional group (-N_3). An EYFP variant harbouring a cysteine mutation was cross-linked with DBCO. **(b)** An EYFP variant harbouring a cysteine mutation was site-specifically cross-linked with PM. The EYFP-PM conjugates were used to replace adsorbed SC on the surface of SC-suspended SWCNTs. In both panels, "c" denotes the cysteine residue and "m" denotes the reactive maleimide group.

3.3 Materials and methods

Construction of recombinant EYFP plasmids. The *eyfp* gene from the pEYFP vector (Clontech Laboratories, Inc. CA, USA) was amplified using Phusion DNA Polymerase (M053S, New England Biolabs) with primer pairs Nde-N-EYFP-F/Xho-N-EYFP-R, Nde-C-EYFP-F/Xho-C-EYFP-R, or Nde-C-EYFP-F/Xho-N-EYFP-R (**Table C.1**), generating NdeI and XhoI restriction sites at the 5' and 3' ends, respectively. The fragments were sub-cloned into a pJET 1.2 cloning vector, excised with the respective restriction enzymes, and ligated into a likewise cut expression vector, pET21a(+). All amplified and restriction fragments were purified by gel electrophoresis using a QIAEX II Gel Extraction Kit (QIAGEN). Transformants were selected on LB agar containing 100 µg mL^{-1} carbenicillin, and plasmid DNA was isolated with a Zyppy Plasmid Miniprep Kit (Zymo Research). The final constructs were verified by sequencing (GATC, Germany).

EYFP expression and purification. Chemically competent *E. coli* BL21(DE3) were transformed with the expression constructs by heat shock. Selected colonies were cultivated in LB yeast extract-tryptone medium (**Table C.3**) in 2 L culture flasks at 30 ^{o}C and 180 rpm. Heterol-

ogous protein expression was induced with 0.25 mM isopropyl β-D-1-thiogalactopyranoside (IPTG) (Sigma Aldrich). Cells were harvested after 4 h by centrifugation at 10 000 × g for 10 min, and pellets were lysed in 10-volume excess of B-PER Bacterial Protein extraction reagent (Thermo Scientific) supplemented with 500 µg mL^{-1} lysozyme, 2 µg mL^{-1} deoxyribonuclease (DNase), 4 mM $MgSO_4$, 1 mM EDTA (Sigma), and 1 mM phenylmethylsulfonyl fluoride (PMSF). The cell extract was filtered through a 0.2 µm porous sterile filter and stored at 4 ^{o}C in PBS buffer. Proteins were purified by affinity chromatography (HisTrap HP 1 mL column, GE Healthcare; loading buffer: 20 mM PBS at pH 7.4 with 500 mM NaCl and 20 mM imidazole (the sample was washed with 5 column volumes of the loading buffer); elution buffer: 20 mM PBS at pH 7.4 with 500 mM NaCl and 500 mM imidazole), followed by size-exclusion chromatography (HiPrep 16/60 Sephacryl S-300 High Resolution column, GE Healthcare; elution buffer: 10 mM PBS at pH 7.4 with 140 mM NaCl) in an AKTA Start setup (GE Healthcare). The purified proteins were concentrated using a 10 kDa Amicon Ultra - 15 mL centrifugal filter (Merck Millipore) and the solvent was exchanged with a 10 mM EDTA in PBS (pH 7.0). A protein's molecular weight of 28.0 kDa was confirmed by mass spectrometry (6530 Accurate-Mass Q-TOF LC/MS, Agilent Technologies) shown in **Figure C.2**. The concentration of EYFP in stock solutions was adjusted to 1.2 - 1.3 mg mL^{-1} based on absorbance measurements using a Nanodrop 2000 spectrometer (Thermo Scientific) and a molar extinction coefficient of ϵ_{514nm} = 83 400 $M^{-1}cm^{-1}$ (or 2.98 mL $mg^{-1}cm^{-1}$) [181]. The purified proteins were stored at 4 ^{o}C.

Cysteine reactivity with EYFP variants. EYFP(N)-Cys, EYFP(C)-Cys, and wild type EYFP were reduced using 10 mM TCEP (abcr) in 10 mM EDTA and PBS at pH 7.0 for 1 h while shaking at 500 rpm in an Eppendorf ThermoMixer (Eppendorf) at 5 ^{o}C. The product was purified using a PD midiTrap G-25 desalting column (GE Healthcare) eluted with the EDTA-containing PBS buffer. The protein concentrations were adjusted to 0.5±0.1 mg mL^{-1} (NanoDrop 2000, Thermo Scientific) and 195 µL of each sample was mixed with 5 µL of freshly prepared 20 mM SPDP (Abcam) in DMSO (Sigma) in a 96-well plate. Absorbance spectra were measured using a Varioskan LUX plate reader (ThermoFisher Scientific) before and 30 min after SPDP addition. During incubation, the 96-well plate was shaken at room temperature. Measurements were also performed in the absence of proteins (with PBS buffer) as a control. The reduced protein solutions were stored at 4 ^{o}C.

SDS-PAGE analysis. The wild type, mutated, and TCEP-reduced proteins were diluted in PBS and mixed 1 : 1 with 2x SDS-containing loading buffer (BlueJuice, invitrogen). The samples were heated to 95 ^{o}C for 6 min while shaking at 500 rpm in a thermomixer. Next, 15 µL of each sample was separated on a 12% Tris-glycine SDS-polyacrylamide gel run at 100 V for 10 min and 250 V for 30 min in a Mini-PROTEAN Tetra cell system (Bio-Rad Laboratories). The gel was stained for 2 h using a 0.25% Coomassie Brilliant Blue dye (ITW Reagents) in 40% ethanol and 10% acetic acid. The gel was immersed in a destaining solution (4:1:5 ratio of ethanol:acetic acid:water) for 4 h and imaged using a Fusion Solo S gel imager (Vilber Loumat).

Absorbance spectroscopy. Absorbance spectra of SC-SWCNTs, EYFP-SWCNTs, and EYPF-PM-SWCNTs between 250 and 1400 nm were recorded in a quartz cuvette (10 mm, Quartz

SUPRASIL, Hellma Analytics) using a UV-vis-NIR spectrophotometer (UV-3600 Plus, SHIMADZU). SWCNT concentration was determined using an extinction coefficient of $\epsilon_{739\,nm}$ = 25.3 mL mg^{-1} cm^{-1} [127]. The absorbance of EYFP, EYFP-PM, and PM solutions were measured in a NanoDrop 2000 (Thermo Scientific). For these measurements, the PM was dissolved in DMSO. The protein samples were diluted in order to record the absorbance spectra shown in the figures, the concentration of proteins are indicated in figure captions. EYFP and PM concentrations were calculated based on absorbance at 514 nm ($\epsilon_{514\,nm}$ = 83 400 M^{-1} cm^{-1}) [181] and 338 nm ($\epsilon_{338\,nm}$ = 40 000 M^{-1} cm^{-1}) [182], respectively.

Functionalization of SWCNTs with ssDNA. A 5'-N_3-$(GT)_{15}$-3' (ssDNA) sequence was purchased from Microsynth. 1 mg of (7,6)-enriched CoMoCAT SWCNTs (Sigma Aldrich) was added to 1 mL of 100 µM ssDNA in 0.1 M NaCl. The mixtures were kept in an ice bath and sonicated using a cup-horn Q700 sonicator (QSonica) at 1% for 60 min. The ssDNA-SWCNT suspensions were centrifuged for 3 h at 21 130 × g in an Eppendorf 5424R centrifuge. To remove the free ssDNA, the supernatants were collected and centrifuged in a 100 kDa MWCO centrifugal filter at 3 220 × g (Amicon Ultra-2 mL, Merck Millipore). Fresh PBS (pH 7.4) was added every time to the suspension in the device dropped below ~300 µL. This filtration step was repeated 6 times before the suspensions were collected and once more centrifuged in tubes at 21 130 × g for 30 min. The supernatants were collected, and the concentration of the SWCNTs in the suspensions was calculated as described above. The resulting ssDNA-SWCNT suspensions were stored at 4 ^{o}C.

EYFP conjugation to DBCO and ssDNA. Freshly prepared 20 mM DBCO (Tokyo Chemical Industry) in DMSO was mixed with reduced EYFP(C)-Cys (0.05 mM, 1.3 mg mL^{-1}) in an 8:1 molar ratio. The sample was shaken overnight at 5 ^{o}C. The unreacted DBCO was subsequently removed using a desalting column (PD midiTrap G-25, GE Healthcare). The fraction containing the EYFP-DBCO conjugate was collected and concentrated to 0.005 mM (0.13 mg mL^{-1}) in PBS (pH 7.4) using an Amicon Ultra - 0.5 mL 10 kDa MWCO (Merck Millipore) column. The EYFP-DBCO was mixed with ssDNA-SWCNTs in a 4:1 molar ratio and shaken at 500 rpm overnight at 5 ^{o}C. Unreacted protein was removed with a 300 kDa MWCO dialysis device (Spectra/Por Float-A-Lyzer, Spectrum Laboratories) over 24 h. The dialysis buffer was changed three times during dialysis. The procedure was repeated with the unconjugated EYFP(C)-Cys. Absorbance spectra were taken after the dialysis and normalized to absorbance values at 739 nm.

SC-suspended SWCNTs. 50 mg of (7,6)-enriched CoMoCAT carbon nanotubes (Sigma Aldrich) were mixed with 50 mL of 2 wt% SC (Sigma Aldrich). The solution was sonicated for 60 min using a tip sonicator (1/4 in. tip, QSonica Q700) at 1% amplitude in an ice bath. Next, the SC-SWCNT suspension was centrifuged at 16 4000 × g for 3 h (Beckman Optima XPN-80), and the supernatant was collected. The resulting SC-SWCNT stock solution had a SWCNT concentration of 43 mg L^{-1} (ϵ_{739nm} = 25.3 mL mg^{-1} cm^{-1}) and was stored at room temperature [127].

EYFP conjugation to PM and functionalization of SWCNTs. To conjugate reduced EYFP(C)-Cys with PM (abcr), 5 µL of freshly-prepared 40 mM PM solution in DMSO was added to

995 µL of a ~0.045 mM EYFP(C)-Cys solution and kept overnight at 5 ^{o}C while shaking at 500 rpm. The unreacted PM was removed using the desalting column, and the eluted protein was concentrated using a 10 kDa MWCO centrifugal filter (Amicon Ultra - 0.5 mL 10 kDa, Merck Millipore). The obtained concentration of the protein solution was ~1.6 mg mL^{-1}. The conjugated pyrene concentration was calculated from spectrophotometric measurements using the following equation:$(A_{\text{EYFP-PM 338 nm}}\text{-}A_{\text{EYFP 338 nm}})/(L \times \epsilon_{338\text{ nm}})$, where A is measured absorbance value, L is the pathlength, and $\epsilon_{338\text{ nm}}$ = 40 000 M^{-1} cm^{-1} [182]. EYFP-PM were mixed with the SC-SWCNT suspension and dialyzed at 5^{o}C in a 14 kDa MWCO dialysis tubing (cellulose membrane, D9277, Sigma Aldrich) for 4 h against 2 L of PBS. The suspension was loaded in a 300 kDa MWCO dialysis device and dialyzed for 24 h. Next, the samples were transferred to new dialysis devices, and dialyzed for another 24 h (changing the dialysis buffer two times). The EYFP-SWCNT sample was prepared in a procedure that excluded protein reduction and conjugation steps. The EYFP-PM-SWCNT and EYFP-SWCNT suspensions were stored at 4 ^{o}C.

Fluorescence spectrometry. EYFP and EYFP-PM fluorescence spectra were measured in a Varioskan LUX plate reader in a bottom-scanning plate reading mode. Excitation was performed at 345±2.5 nm and 514±2.5 nm.

CD spectroscopy. UV-CD spectra of EYFP, EYFP-SWCNTs, and EYFP-PM-SWCNTs were taken using a J-810 CD spectropolarimeter (Jasco) relative to a reference cuvette containing PBS. The composition of the protein's secondary structure was predicted using BeStSel software [183, 184].

NIR fluorescence spectroscopy and SWCNT wrapping exchange. NIR fluorescence measurements were taken in a 96-well plate on a custom-built NIR epifluorescence spectrofluorometer (IsoPlane SCT-320 spectrometer with NIRvana 640 ST camera, Princeton Instruments). The 96-well plate was illuminated with a 660±10 nm (or 660±5 nm in the (7,6) chirality measurements) laser (SuperK Extreme EXR-15 and SuperK Varia, NKT Photonics) through a 20x objective (M Plan Apo NIR, Mitutoyo Corporation). Fluorescence spectra were acquired at a frame rate of 0.5 fps at a focal point near the bottom of a well. Wells were filled with 49.5 µL of the ssDNA-SWCNT, EYFP-SWCNT, or EYFP-PM-SWCNT suspensions. 0.5 µL of freshly-prepared 10 wt% SDC (Sigma Aldrich) or SDS (Acros Organics) solutions in PBS were added ~1 min after the beginning of the acquisition, and the wells were carefully mixed by pipetting up and down three times. Fluorescence spectra were analyzed and plotted using a custom MATLAB code.

3.4 Results and discussion

3.4.1 Synthetic engineering of EYFP variants

We studied site-specific immobilization of a protein onto SWCNTs. For that purpose, we genetically engineered two EYFP variants by introducing a cysteine residue at either the N- or C-terminus of the coding sequence. Both variants, along with wild type EYFP, were

cloned into a pET21 expression vector harbouring a C-terminal His-tag, expressed in *E. coli* BL21(DE3), and purified using affinity and size-exclusion chromatography. The proteins were analyzed using a SDS-PAGE (**Figure C.1**). An EYFP monomer band at ~28 kDa was detected in all samples. In the cysteine-containing variants, the additional band at ~55 kDa appeared, which we attribute to the dimer formation through the disulfide bond. Hence, the purified proteins were reduced by the addition of TCEP (**Figure 3.2a**). The TCEP was removed and the suspension buffer was changed to PBS with 10 mM EDTA using a desalting column. Finally, we performed a thiol cross-linking reaction with thiol-specific SPDP. By monitoring the absorption of the reaction product, pyridine-2-thione, at 343 nm, we could confirm the reactivity of the thiol group in the EYFP variant with the C-terminal cysteine, which we used in all further experiments (**Figure 3.2b**).

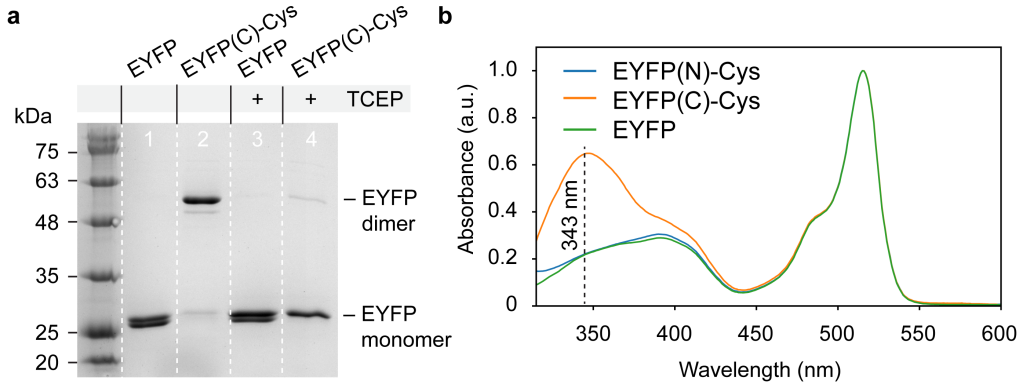

Figure 3.2 – Reactivity of free thiols in engineered EYFP variants. (a) SDS-PAGE analysis of EYFP(C)-Cys before and after reduction with TCEP. The samples were stored for two weeks at 4°C before the analysis. Non-reducing gel electrophoresis was performed on a 12% polyacrylamide gel at 100 V for 10 min and at 250 V for 30 min. The gel was stained with the Coomassie Brilliant Blue dye, and a protein marker IV ladder (molecular weight 11-245 kDa, AppliChem) was used for size reference. **(b)** Absorbance spectra of reduced EYFP(N)-Cys (blue line), EYFP(C)-Cys (orange line), and EYFP (green line) 30 min after reaction with SPDP. The spectra were normalized to the absorbance values at 514 nm. The protein concentrations were 0.5±0.1 mg mL^{-1}.

3.4.2 EYFP immobilization onto SWCNTs using ssDNA

Bioconjugation of the EYFP-DBCO and azide-containing ssDNA-SWCNT was confirmed through absorption and florescence spectroscopy. **Figure 3.3a** shows UV-Vis absorption spectra of EYFP(C)-Cys before (green line) and after conjugation (orange line) to DBCO. The spectra show EYFP absorbance peaks at 514 and 280 nm. The DBCO absorption peak at ~309 nm in the EYFP-DBCO fraction suggests successful linker conjugation to EYFP(C)-Cys. We observed an increase in absorbance at 514 nm upon EYFP-DBCO conjugation to the ssDNA-SWCNT (orange line, **Figure 3.3b**). In the absence of DBCO (green line), the absorption value matches that of the negative control containing only ssDNA-SWCNT in the absence of the protein (blue line). We note that the overlapping peak around 514 nm for the ssDNA-SWCNT sample corresponds to the absorption peaks of metallic nanotubes [91]. The absorption

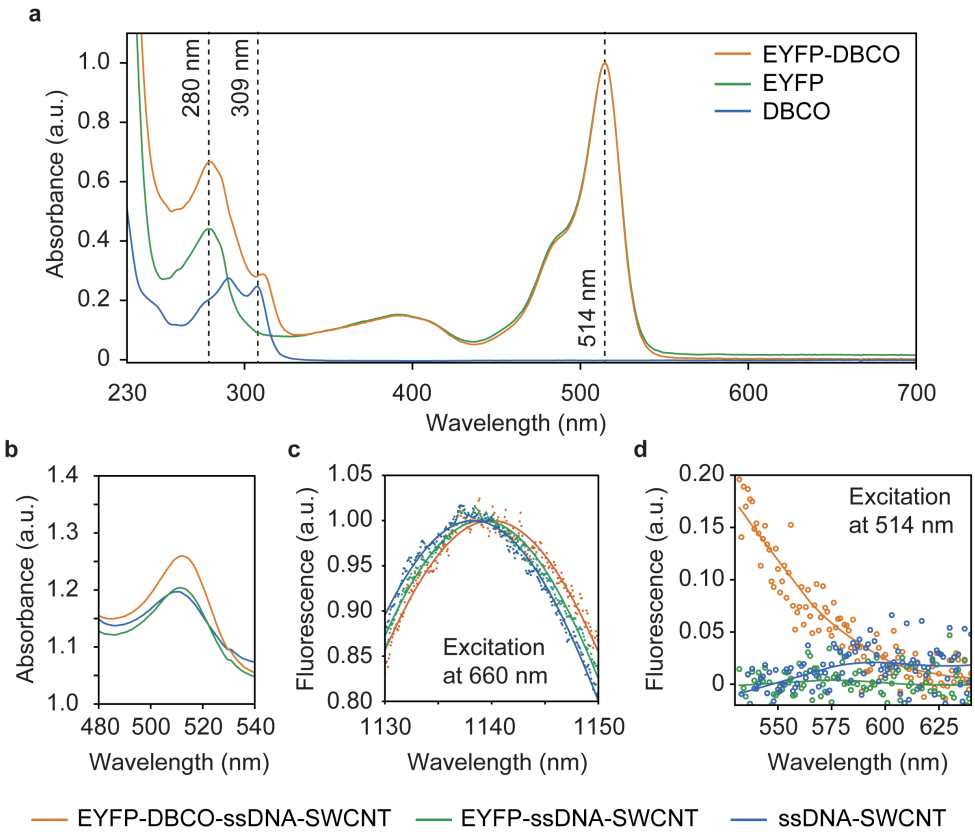

Figure 3.3 – EYFP immobilization onto SWCNTs using a ssDNA wrapping. **(a)** UV-Vis absorbance spectra of the EYFP-DBCO conjugate (orange line) (0.13 mg mL^{-1}), EYFP (green line) (0.13 mg mL^{-1}), and DBCO (blue line) (20 µM). The dotted lines represent the EYFP absorbance peaks at 280 and 514 nm and DBCO absorbance peak at 309 nm. The EYFP and EYFP-DBCO spectra were normalized to the absorbance values at 514 nm. **(b)** Absorbance spectra of EYFP-DBCO-ssDNA-SWCNTs (orange line) and EYFP-ssDNA-SWCNTs (pristine protein) (green line) after dialysis, and ssDNA-SWCNTs (blue line). The spectra were normalized to SWCNTs absorbance at 739 nm. **(c)** NIR fluorescence spectra of EYFP-DBCO-ssDNA-SWCNTs (orange dots), EYFP-ssDNA-SWCNTs (green dots), and ssDNA-SWCNTs (blue dots). The spectra were fitted with Gaussian functions and normalized to the maxima of fluorescence intensities (lines). Excitation at 660±5 nm. **(d)** Visible light fluorescence spectra of EYFP-DBCO-ssDNA-SWCNTs (orange circles), EYFP-ssDNA-SWCNTs (green circles), and ssDNA-SWCNTs (blue circles). The lines show fitted spectra using a LOWESS function. Excitation at 514±2.5 nm.

enhancement in the presence of conjugate protein indicates that the DBCO is needed for a successful immobilization, and unspecific adsorption of the protein on the ssDNA-SWCNT surface can be mostly excluded after dialysis. In addition, the corresponding SWCNT fluorescence emission for the conjugated and pristine protein samples is shown in **Figure 3.3c**.

The (7,6) fluorescence peak at 1138.3±0.1 nm underwent a red-shift to 1400.0±0.1 nm when EYFP-DBCO was conjugated to the ssDNA-SWCNTs. This red-shifting is suggestive of a change in the dielectric constant of the environment in the vicinity of the SWCNT surface [185]. The protein lacking the DBCO linker had the emission maxima at 1139.1±0.1 nm, indicating that

the proteins presumably were adsorbed onto the ssDNA-SWCNTs areas which remained uncovered with the ssDNA. However, the adsorbed proteins were not fluorescent upon excitation at 514 nm (green line, **Figure 3.3d**), that was not the case for the conjugated proteins in the EYFP-DBCO-ssDNA-SWCNT sample (orange line and dots). We hypothesize that the non-specifically adsorbed proteins onto the SWCNT surface have distorted folding, therefore, they are not fluorescent and do not adsorb at 514 nm (green line, **Figure 3.3b**).

3.4.3 EYFP immobilization onto SWCNTs using PM

An alternative site-specific immobilization procedure was achieved through pyrene-based linking (**Figure 3.1b**). Bioconjugation of the protein was confirmed through absorption, fluorescence, and mass spectrometry (**Figure 3.4**). **Figure 3.4a** shows that the characteristic absorbance peaks of the PM at 267, 278, 315, 329, and 345 nm appear in the conjugated protein spectrum after removal of free PM. Furthermore, pyrene fluoresces at 376 and 396 nm (excitation at 345 nm) when a covalent bond is formed between the PM's maleimide and the protein's thiol group [186]. As shown in **Figure 3.4b**, the expected emission peaks of PM are observed at 376 and 396 nm, along with the EYFP emission peak at 531 nm, for the EYFP-PM spectrum (orange line), confirming bioconjugation to the protein. In addition, the EYFP-PM sample was analyzed through mass spectrometry (**Figure 3.4c**), which confirms an expected peak at 28.3 kDa corresponding to the EYFP-PM complex.

Absorbance measurements were also used to confirm the conjugation of the EYFP-PM complexes to SWCNTs (**Figure 3.5a**). Upon conjugation, both the non-specifically adsorbed EYFP-SWCNT samples and bioconjugated EYFP-PM-SWCNT samples show solvatochromic shifting of the chirality peaks relative to the correspondent peaks in the SC-SWCNTs. The red-shifting is indicative of increased accessibility to water when the SC is displaced with less tightly wrapped coatings, in agreement with the literature [187, 188]. The EYFP-PM-SWCNT undergoes more substantial shifting than the EYFP-SWCNT, which could indicate that either the PM linker water accessibility to the SWCNT surface or the direct protein absorbance is limited by the π-stacking of the linker onto the SWCNT surface. Furthermore, compared to SC-SWCNTs, we observe an ~180% increase in absorbance at 514 nm for EYFP-PM-SWCNTs and EYFP-SWCNTs, in correspondence with EYFP immobilization. This substantial increase relative to the observed for the EYFP-DBCO-ssDNA-SWCNTs (~5%) suggests more effective immobilization of the protein through non-specific adsorption and PM linker-based conjugation than the ssDNA-based.

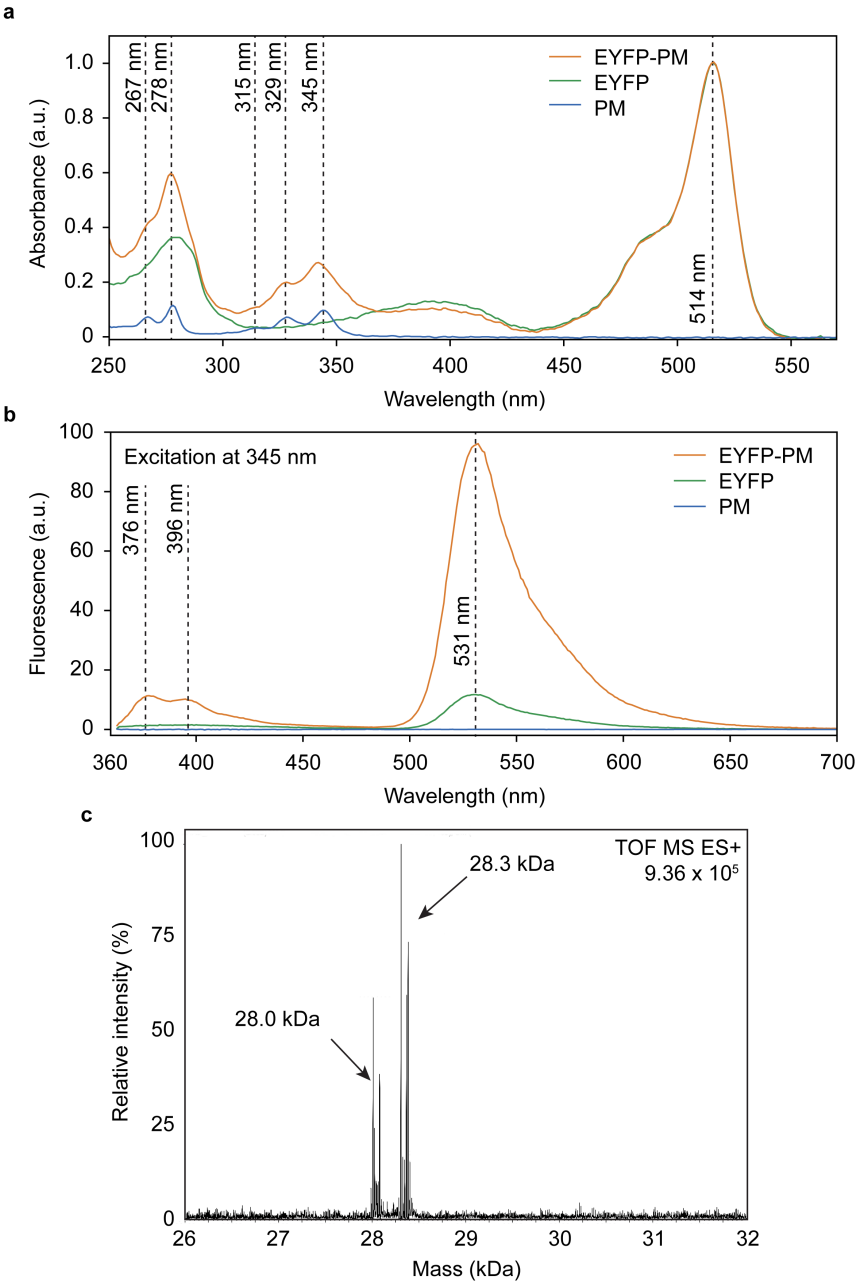

Figure 3.4 – Conjugation of EYFP to a PM linker. **(a)** Absorption spectra of EYFP-PM conjugate (orange line), pristine EYFP (green line), and PM (blue line). The PM was dissolved in DMSO. The dotted lines at 267, 278, 315, 329, and 345 nm show PM absorbance peak maxima, and the dotted line at 514 nm the EYFP absorbance peak maximum. The EYFP and EYFP-PM spectra were normalized to the absorbance values at 514 nm. **(b)** Emission spectra of EYFP-PM conjugate (orange line) and pristine EYFP (green line), and PM (blue line). The PM sample prepared in PBS and treated in the same way as the EYFP-PM and EYFP solutions. Emissions (dotted lines) are shown for bioconjugated PM at 376 and 396 nm, as well as the EYFP absorbance peak at 531 nm. Excitation at 345±2.5 nm. **(c)** Mass spectrum of EYFP-PM solution showing unconjugated EYFP(C)-Cys (28.0 kDa) and EYFP-PM (28.3 kDa). The size of the PM linker is 0.297 kDa. The 28.0 kDa peak indicates that free EYFP(C)-Cys present in the solution.

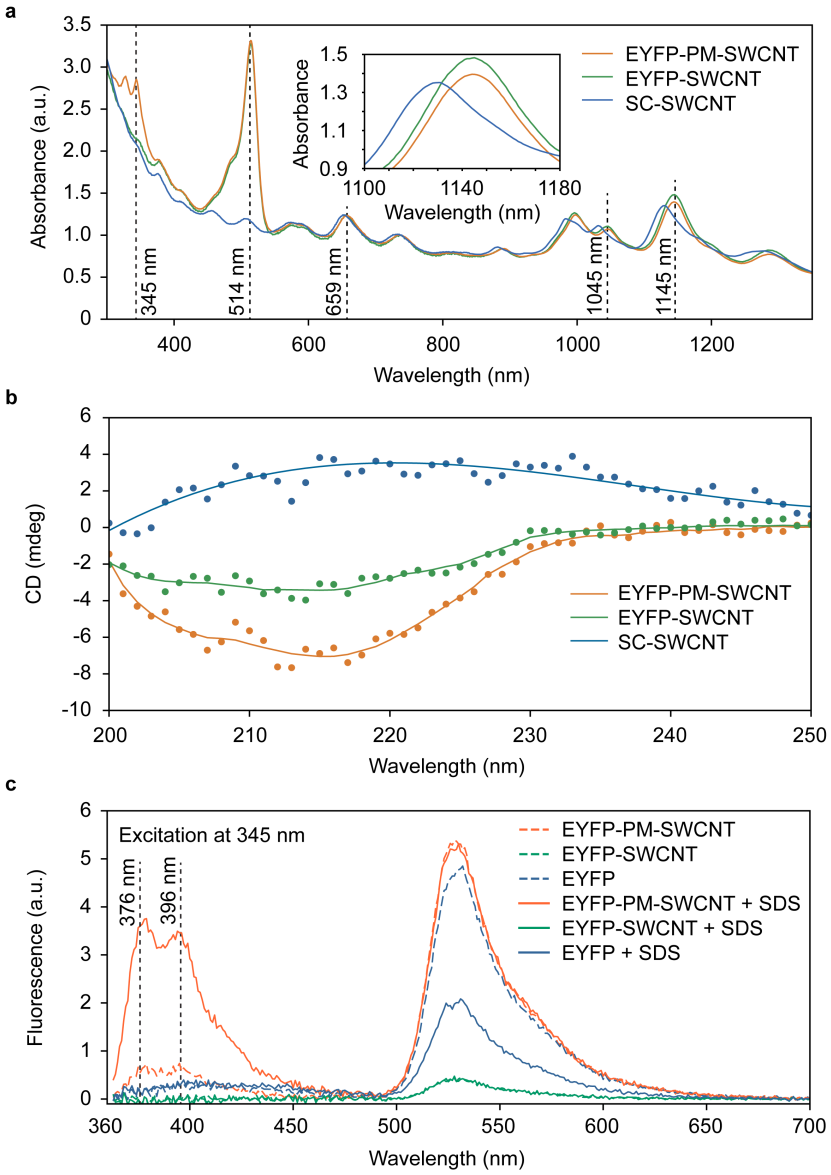

Figure 3.5 – EYFP immobilized onto SWCNTs using a PM linker. (a) Absorption spectra of SC-SWCNTs (blue line) before dialysis and the resulting EYFP-PM-SWCNT (orange line) and EYFP-SWCNT (green line) suspensions after dialysis. The inset shows the absorbance region between 1100 and 1180 nm. The spectra were normalized to SWCNT absorbance at 739 nm. The dotted lines show the absorbance peak of PM at 345 nm, EYFP at 514 nm, EYFP-PM-SWCNT E_{22} (7,5) and E_{22} (7,6) peaks at 659 nm, EYFP-PM-SWCNT E_{11} (7,5) at 1045 nm, and the EYFP-PM-SWCNT E_{11} (7,5) peak at 1145 nm. **(b)** CD spectra of EYFP-PM-SWCNTs (orange dots), EYFP-SWCNTs (green dots), and SC-SWCNTs (blue dots). The suspensions were prepared in PBS. The EYFP-PM-SWCNT and EYFP-SWCNT spectra were fitted using a secondary structure prediction software BeStSel [183, 184], and the SC-SWCNT spectrum was fitted with the third order polynomial function (solid lines). **(c)** Fluorescence spectra of EYFP-PM-SWCNTs (orange lines), EYFP-SWCNTs (green lines), and EYFP (blue lines) before (dashed lines) and after (solid lines) addition of SDS (to final concentration of 0.1 wt%). The concentration of EYFP was 1.2 mg mL^{-1}. Excitation at 345±2.5 nm. Dotted lines show the emission maxima of bioconjugated PM at 376 and 396 nm.

The effects of the PM linker on protein conformation was further studied through the CD measurements shown in **Figure 3.5b**. The percentage of the β-strands in the secondary structure of the protein was analyzed using BeStSel software [183, 184]. In the EYFP-PM-SWCNT sample was predicted for 10% more of an antiparallel β-strands content in the secondary structure of the protein in comparison to the EYFP-SWCNTs, which had the amount of antiparallel β-strands of 30%. Better preservation of protein's folding through polymer-based linkers was already reported in literature [26, 27]. We hypothesize that PM could reduce unfolding of EYFPs due to their different average distance from the SWCNT and more regular spatial organization on the SWCNT surface that protects the protein's amino acids from direct adsorption onto the SWCNTs.

The interaction of the PM linker with a SWCNT surface was studied by monitoring the fluorescence emission of the PM in the presence and absence of SDS, which preferentially binds to the SWCNT surface. As discussed for **Figure 3.4b**, PM fluoresces when conjugated to EYFP. However, in the vicinity of the SWCNT surface, the PM fluorescence was quenched (**Figure 3.5c**, orange dashed line) [189]. The addition of a 0.1 wt% SDS displaces the EYFP-PM from the SWCNT surface, recovering the PM fluorescence at 376 and 396 nm (solid orange lines). Additionally, we observed a decrease in EYFP fluorescence at 531 nm on the addition of SDS (blue line), which we attribute to denaturation of the proteins by SDS, in accordance with the previous studies [190]. Interestingly, the denaturation of EYFP was not observed when SWCNT is present.

3.4.4 SWCNT interaction with the wrapping molecules

The positions of the (7,5) SWCNT peak maxima are compared for (**i**) SDS-SWCNTs, (**ii**) SDC-SWCNTs, (**iii**) ssDNA-SWCNTs, (**iv**) EYFP-SWCNTs, and (**v**) EYFP-PM-SWCNTs in **Figure 3.6a**. The surfactant-coated SWCNTs show the fluorescence at a lower wavelength in comparison to the protein-functionalized SWCNTs. The emission peak of EYFP-PM-SWCNTs was red-shifted by 2 nm compared to the EYFP-SWCNT peak (1 tailed t-Test $p = 4 \times 10^{-5} < 0.05$). This observation is in agreement with the absorbance measurements presented in **Figure 3.5a**, which show distinct optoelectronic characteristics between the adsorbed EYFP and EYFP-PM.

The apparent binding affinity of the protein and ssDNA to SWCNTs was evaluated by monitoring the exchange of the SWCNT wrappings with surfactants using NIR spectroscopy [191–193]. The binding affinities of surfactants to SWCNTs vary for different chiralities [193, 194]. We compared apparent binding affinities, K_A, of ssDNA, EYFP, and PM-EYFP for the E_{11} peak of the (7,5) chirality. As a model system in this experiment were used the ssDNA-SWCNTs, EYFP-SWCNTs, and EYFP-PM-SWCNTs. 0.1 wt% SDS was added to the ssDNA-SWCNT, EYFP-SWCNT, and EYFP-PM-SWCNT suspensions, and the peak position was monitored over time (**Figure 3.6b**). After addition of the SDS solution, we observed blue-shifts for the EYFP-SWCNTs and EYFP-PM-SWCNTs. However, the peak position of the ssDNA-SWCNTs remained unchanged. The fluorescence shifts co-occurred with fluorescence intensity increase through

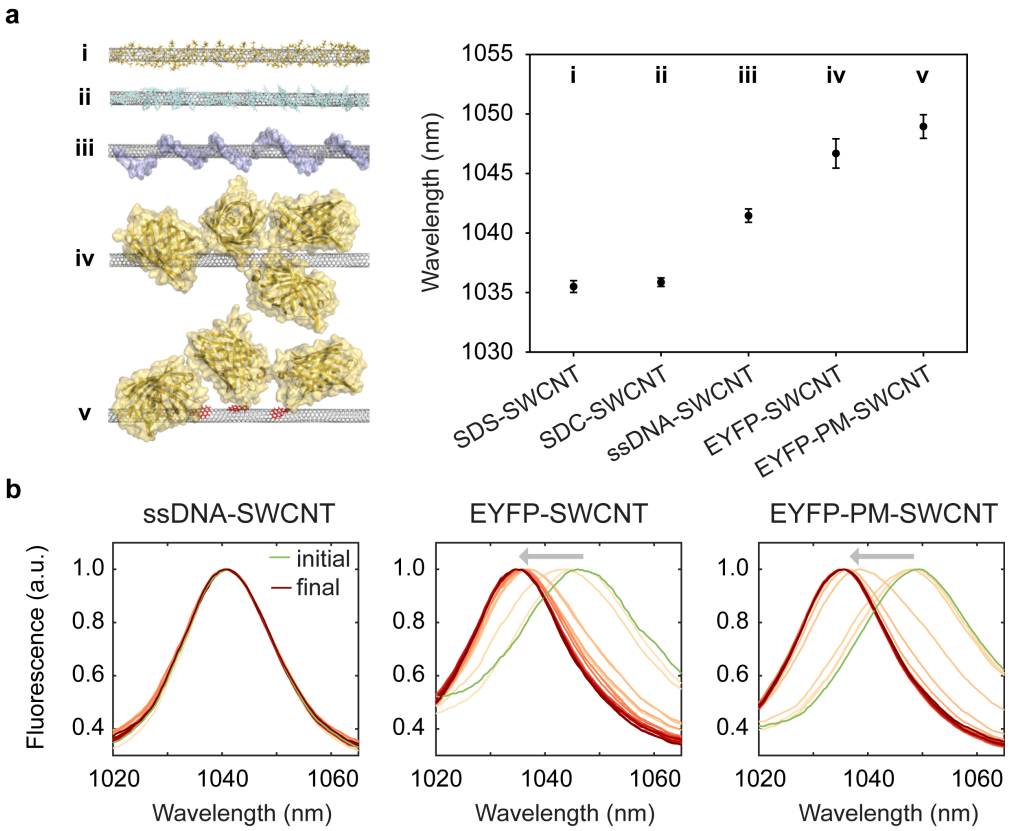

Figure 3.6 – Fluorescence shifting of the (7,5) SWCNT peak. (a) Starting wavelength positions of SWCNTs wrapped with (**i**) SDS, (**ii**) SDC, (**iii**) ssDNA, (**iv**) EYFP, and (**v**) EYFP-PM. Excitation at 660±10 nm. **(b)** Time laps of fluorescence spectra before (green line) and after (yellow to brown colour gradient) addition of SDS with the final concentration 0.1 wt%. The traces are shown with 10 s time intervals. Excitation at 660±10 nm.

the surfactant exchange process (**Figure C.3**). *Zheng et al.* have reported that this change is caused due to increased surface coverage and oxygen exclusion [164]. Next, we repeated the experiments using SDC instead of 0.1 wt% SDS, which exhibited stronger binding affinity to SWCNTs and exchanged the ssDNA, EYFP, and EYFP-PM wrappings (**Figure C.4**). These results allowed us to identify the order of apparent binding affinities relative to each of the wrappings: $K_{A\ SDC} > K_{A\ ssDNA} > K_{A\ SDS} > K_{A\ EYFP} \sim K_{A\ EYFP\text{-}PM}$. However, the difference in the binding affinities between EYFP and EYFP-PM still remain unresolved. Nevertheless, this is the first example of an association between a thermodynamic parameter and wavelength changes during SWCNT surface exchange applied to a protein study.

3.5 Conclusion

In this chapter, we compared two methods for site-specific functionalization of a SWCNT surface. We engineered EYFP containing single cysteine mutations at either the N- or C-terminus for two different bioconjugation strategies. In the first functionalization approach,

SWCNTs were wrapped with azide-ssDNA and the azide group was reacted with cysteine using a DBCO crosslinker. The second method was achieved through C-terminal cysteine bioconjugation to the PM linker. A combination of absorbance, fluorescence, and mass spectroscopy was used to verify the conjugation. A comparison of ssDNA-based and PM-based methods suggest that using the PM-linking was achieved 180% increase in protein's absorbance peak in comparison to 5% for the EYFP-PM-SWCNT conjugates that indicates higher protein retention on the SWCNT surface in comparison to the ssDNA conjugation approach.

Moreover, CD measurements show that the PM linker better retains protein fold compared to the non-specifically adsorbed EYFP. The site-specific PM conjugation can be readily applied to other proteins containing accessible cysteine residues. The efficiency of this approach, combined with the ability to help preserve protein structure, unlocks an unexplored experimental avenue towards achieving protein-based optical diagnostics based on SWCNT fluorescence.

4 GOx-PM-SWCNT sensors for continuous glucose monitoring

This chapter consists of a manuscript prepared for submission in a journal. The co-authors of this work are: N. Schuergers and A. A. Boghossian.

Author contributions: *V.Z., N.S., and A.A.B. participated in experimental design. N.S. performed cloning. V.Z. expressed the proteins and performed the experiments. V.Z., N.S., and A.A.B. wrote the manuscript. V.Z. and A.A.B. conceived and designed the research.*

4.1 Abstract

In this chapter, we used the protein immobilization method described in **Chapter 3** and developed an optical glucose sensor by linking genetically engineered GOx and SWCNTs using the PM linker. Variants of GOx with rationally-engineered cysteines were expressed in *Pichia pastoris*. A GOx(70C) variant with the surface thiols was cross-linked with PM and immobilized onto SWCNTs. The GOx-PM-SWCNT sensors were characterized using absorbance and NIR fluorescence spectroscopy. We demonstrated an application for continuous glucose monitoring in the NIR-II optical region using the GOx-PM-SWCNT conjugates.

4.2 Introduction

Advancements in optical glucose detection have led to continuous and long-term non-invasive sensors [52, 53]. Despite the advantages of dye-based sensors offer in terms of specificity and accuracy, conventional dyes photobleach under prolonged illumination. Fluorophores such as SWCNTs offer photostability that can further extend the lifespan of optical sensors required for continuous *in vivo* monitoring. Furthermore, they have demonstrated biocompatibility in long-term *in vivo* measurements with proper functionalization and encapsulation [41]. The fluorescence of SWCNTs show single-molecule sensitivity to the surrounding environment, and this sensitivity serves as the mechanism for enabling an optical sensor response [195].

The selectivity of these SWCNT-based sensors can be modulated by nanotube surface func-

tionalization with proteins, such as glucose-binding protein, glucose dehydrogenase, concanavalin A, or GOx [19, 20, 55, 56]. Among these proteins, GOx represents the gold standard for glucose sensing because of its stability and high specificity to glucose [57]. The oxidation of glucose and release of free electrons occur at the reaction centre of the protein in the presence of a FAD cofactor. The key challenge for effective glucose sensing lies with the bioconjugation strategy of the protein [18]. While non-specific protein adsorption provides a facile, scalable approach towards achieving adequate immobilization, the adsorption efficiency is protein-specific and depends on the surface chemistry of the proteins [196, 197]. The disruption in adsorbed protein conformation may also result in loss of activity. Moreover, the sensor response is limited to only correctly oriented proteins. In the case of GOx, proteins oriented with active sites in close proximity to the SWCNT, for example, could be involved in optical modulation through an enzymatic pocket doping [19]. Addressing these challenges through improved and novel bioconjugation strategies is the focus of recent studies [20, 23, 185].

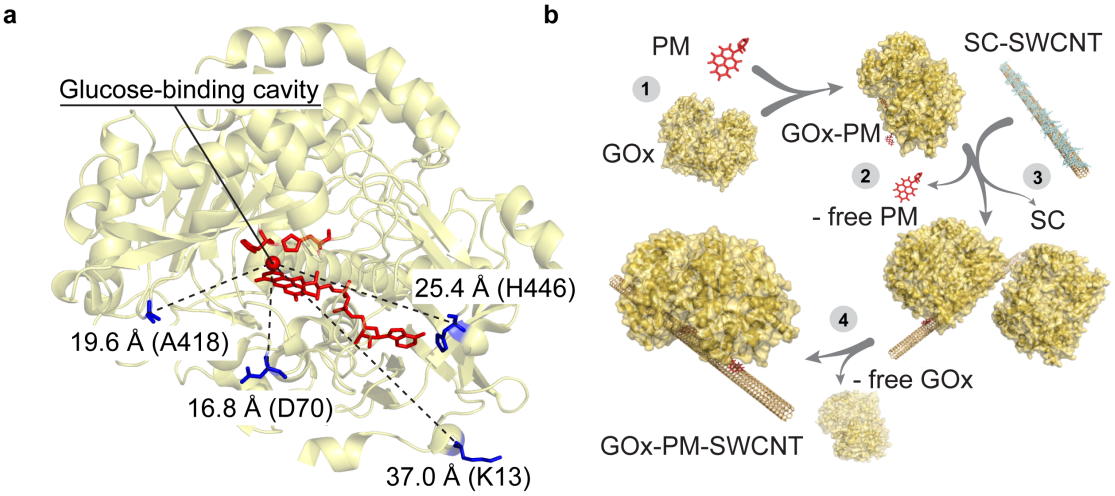

Figure 4.1 – Selected residues for site-directed GOx mutagenesis. (a) Indicated distances are shown between the glucose-binding cavity above the *si*-face of the flavin ring (tricyclic isoalloxazine) [198], which is shown as a red sphere, and the mutated cysteine residues shown in blue. FAD (shown in red) and glucose capturing amino acids above the glucose-binding cavity (His559 and His516) are shown in red (PDB 3QVP). **(b)** Illustration of GOx-PM-SWCNT reparation steps. (1) Reduction of a GOx mutant and its conjugation to PM. (2) Purification of GOx-PM from the unreacted PM. (3) Wrapping of SC-suspended SWCNTs with GOx-PM and dialysis of SC. (4) Removal of free GOx in the final dialysis step.

In this work, we immobilize GOx using a hydrophobic crosslinker that is covalently conjugated to engineered cysteine residues. While wild type GOx has three native cysteines, these residues are not accessible for conjugation; two cysteines form a disulfide bond (Cys164-Cys206), and the third (Cys521) is buried within the protein [129, 199]. We engineered four variants with single-cysteine mutations **(Figure 4.1a)**. The selected ampholytic crosslinker, PM, contains a maleimide group that can covalently conjugate to the cysteine residues, while the pyrene moiety at the other end can stack onto a SWCNT surface with a binding energy of 32.34 kcal mol^{-1}

(**Figure 4.1b**) [200]. As this binding energy exceeds that for aromatic or aliphatic amino acids (which are in order of 10 kcal mol^{-1} and 5 kcal mol^{-1} respectively), this linker can provide a favored approach for achieving oriented protein binding [24, 200, 201]. Furthermore, the crosslinking approach, summarized in **Figure 4.1b** can lead to improved retention of protein structure and function. This bioconjugation was used to demonstrate a continuous glucose monitoring sensor in the NIR-II optical region.

4.3 Materials and methods

Construction of recombinant plasmids for GOx expression. Positions for non-conserved amino acids were identified using ConSurf software [202]. GOx expression plasmids were constructed using a puC57 vector harbouring a synthetic gene of *A. niger* GOx (GeneBank X16061, **Table D.1**) that lacks the signal peptide. Site-directed mutagenesis for the amino-acid exchanges was performed by two single primer reactions according to a protocol by *Oded et al.* [203], with the exception of the Pwo polymerase, which was substituted by Q5 polymerase. The wild type and mutant variants of the synthetic *gox* gene were amplified using primer pairs from **Table D.2** that add a SapI restriction site, and the gene was ligated into the SapI digested expression vector, pBSYA3S1Z. The ligation fused the coding sequence to an α-factor secretion signal. The resulting vectors were subcloned into *E. coli* and verified by sequencing (GATC, Germany). The PCR was performed in 0.2 mL MicroAmp reaction tubes (applied Biosystems, Life technologies) in a SimpliAmp Thermal Cycler (Thermo Fisher Scientific). Briefly, the 50 µL reaction mix included 5 µl of a 40 pM primer, 4 µL (or 500 ng) of the plasmid DNA, 2 µL of 0.2 mM dNTPs, 1 µl (or 1.5 U) of Q5 Polymerase, 10 µL of 5x Q5 buffer from a cloning kit (M0491S, New England Biolabs), and 28 µL of ddH_2O water. The PCR protocol included denaturation for 15 s at 98 ^oC, annealing for 15 s at 60 ^oC, and elongation for 2 h 30 min at 72 ^oC. This procedure was repeated over 33 cycles. Next, the 40 µL of two single-primer PCR products with forward and reverse primers were combined in a PCR tube, and they were denatured for 5 min at 98 ^oC to separate the synthesized DNA from the plasmid template DNA. The tubes were gradually cooled from 98 ^oC to 16 ^oC. The non-mutated DNAs were digested by 1 µL of 20 U DpnI in 2.5 µL of FD Buffer for 3 h at 37 ^oC and incubated overnight at 10 ^oC. The digested PCR products were analyzed by agarose gel electrophoresis and purified from the gel using a QIAEX II Gel Extraction Kit. Finally, we obtained ~140 ng μL^{-1} expression plasmids, as measured with a NanoDrop 2000 spectrometer (Thermo Fisher Scientific). The plasmids were stored at 20 ^oC.

***P. pastoris* transformation**. Prior to transformation, *P. pastoris* BG11 competent cells were prepared according to a protocol by *J. Lin-Cereghino et al.* [204] 100 µL of competent *P. pastoris* cells were mixed with 3 µg of pBSYA3-GOx-K13C, pBSYA3-GOx-D70C, pBSYA3-GOx-A418C, pBSYA3-GOx-H446C plasmids and wild type pBSYA3-GOx plasmid (bisy e.U.), which was kindly provided by Prof. A. Glieder. Competent *P. pastoris* BG11 cells were transformed with 3 µg plasmid DNA by electroporation at 1.25 kV (Eppendorf Eporator) and transformed colonies were selected on YPD agar plates with 100 µg mL^{-1} Zeocin. 12 randomly selected

clones from each strain were inoculated in 250 µL of BMD 1% growth medium in a sterile 96-deep well plate covered with a gas-permeable 114 µm Rayon film (VWR International) at 30 °C while shaking at 300 rpm. After three days, 250 µL of BMM2 medium was added to the wells. After 12 additional hours, 50 µL of BMM10 medium were added, and this step was repeated two times after an additional 12 and 24 h of incubation. The media preparation protocols are shown in **Table D.3**. After four days, the optical densities of the cultures was measured at 600 nm, and the cultures were centrifuged at 3 220 × g for 10 min. The supernatants were collected to test for GOx activity, and the cell pellets were stored at 4 °C.

Colorimetric GOx enzymatic activity assay. Enzymatic activity was measured colorimetrically using ABTS (BioChemica, ITW Reagents) (**Figure D.3**) [205]. Briefly, 119.8 µL of 50 mM sodium citrate buffer (pH 5.75) was mixed with 80 µL of 1 M glucose (β-D-glucose, AB 136302, ABCR GmbH & CO. KG). Also, 40 µL of 20 mM ABTS was prepared using the sodium citrate buffer. 0.2 µL of 2 mg mL^{-1} horseradish peroxidase type VI (P6782, Sigma) was added before transferring the mixture to 15 µL of the cell culture supernatant. Absorbance at 414 nm was continuously measured in a plate reader (Varioskan LUX). Changes in absorbance were normalized to the optical density of the original expression cultures.

GOx expression in *P. pastoris*. Recombinant GOx was produced in *P. pastoris*, which can achieve yields greater than those using *A. niger* strains [206]. Selected GOx clones (K13C, D70C, A418C, H446C) and wild type GOx were used for protein expression in 2 L Erlenmeyer flasks with cotton tissue plugs. The cells were added to flasks containing 75 mL of BMD 1% medium, and they were incubated at 30 °C while shaking at 300 rpm for two days. On the third day, 75 mL of BMM2 medium was added to induce protein expression. After 12 h, 15 mL of BMM10 medium was added to the flask, and this step was repeated two times. The cell cultures were then centrifuged at 3 220 × g for 10 min, and the supernatants were filtered through a 0.2 µm porous filter. The supernatants were kept on ice and concentrated to ~30 mL using a Vivaflow 50R 30 kDa MWCO crossflow dialysis device (Sartorius). The solutions were further concentrated in an Amicon Ultra centrifugal filter unit (Merck Millipore) with a 10 kDa MWCO, and the buffer was exchanged with PBS (pH 7.4). Finally, ~6 mL of each solution was filtered through a 0.2 µm porous filter and stored at 4 °C.

GOx purification. Purification and extraction of GOx from the protein mixture were performed using the AKTA Start setup (GE Healthcare) at 5 °C. A HiPrep 16/60 Sephacryl S-300 high-resolution column (GE Healthcare) was used for size-exclusion protein purification (**Figure D.1**). 5.5 mL of the protein mixtures were loaded onto the column and eluted using a 10 mM PBS at pH 7.4 with 140 mM NaCl. The protein presence in each eluted fraction was confirmed using the colorimetric GOx enzymatic activity assay, and the GOx-containing fractions were collected and concentrated to ~1 mL in a 10 kDa MWCO Amicon Ultra centrifugal unit. During concentration, the buffer was changed with 10 mM PBS (pH 7.0) with 10 mM EDTA (Sigma) and 150 mM NaCl (PBS-EDTA). The concentration of GOx in the stock solutions were measured in a NanoDrop 2000 (flavin extinction coefficient at 450 nm is 14 000 M^{-1} cm^{-1}) [149, 205] and adjusted to 3 mg mL^{-1} (molecular weight of GOx was determined from SDS-PAGE

analysis to be ~85 kDa). The final protein yields ranged between 8 to 15 mg L^{-1} of cell culture media. GOx solutions were stored at 4 ^{o}C in PBS-EDTA (EDTA is an antimicrobial agent) [207].

SDS-PAGE analysis. 1 µL of each protein solution was diluted in 9 µL of PBS and the combined solution was added to 10 µL of a 2x BlueJuice loading buffer (invitrogen) containing SDS and 20 mM 1,4-dithiothreitol (Carl Roth GmbH). A wild type GOx solution was prepared in PBS using commercially available GOx from *A. niger* (Type II, 19 440 U g^{-1}, Sigma Aldrich). This solution was also mixed with the loading buffer. The proteins were heated to 95 ^{o}C for 6 min while shaking at 500 rpm in 1.5 mL tubes. After, 15 µL of each solution was loaded in a gel. Gel electrophoresis was performed in a Mini-PROTEAN Tetra cell system (Bio-Rad Laboratories) at 100 V for 10 min and 250 V for 50 min. The gel was stained with a 0.25% Coomassie brilliant blue R-250 (ITW Reagents) solution in 40% ethanol and 10% acetic acid for 2 h at room temperature. The gel was then destained for 4 h in an ethanol:acetic acid:water solution prepared in a 4:1:5 ratio. The gel was imaged in a Fusion Solo S gel imager (Vilber Loumat).

CD spectroscopy. UV-CD spectra of GOx was measured between 195 and 250 nm with a J-810 CD spectropolarimeter (Jasco). The reference cuvette was filled with PBS-EDTA. Spectra were smoothed using a convolution filter kernel from the "convolve" function. The spectra were analyzed using BeStSel software to identify differences in the folding of the proteins [183, 184].

Thiol reactivity assay. The wild type and mutant GOx were reduced by 10 mM TCEP (abcr) for 1 hour at 5 ^{o}C while shaking at 500 rpm. The TCEP was removed using a PD midiTrap G-25 desalting column (GE Healthcare) and eluted with PBS-EDTA to minimize the formation of GOx oligomers. The concentrations of GOx were adjusted to 0.87±0.04 mg mL^{-1} using a NanoDrop 2000 spectrometer. 195 µL from each protein solution was transferred to a 96-well plate and absorption spectra were measured in the plate reader. Next, 5 µL of freshly prepared 20 mM SPDP (abcam) in DMSO (Sigma) was mixed with the solutions. The absorbance spectra were repeatedly measured 1, 8, 30, 60, and 120 min after addition of SPDP (**Figure D.5**). The difference between the final absorbance and absorbance before SPDP addition at 343 nm was compared between the proteins. The number of moles of SPDP per mole of GOx was calculated according to the equation, $(\Delta A \times MW)/(c_{GOx} \times \epsilon_{343\,nm})$, where ΔA is the absorbance difference at 343 nm, MW is a molecular weight of GOx, c_{GOx} is concentration of GOx in mg mL^{-1}, and $\epsilon_{343\,nm}$ is the extinction coefficient for pyridine-2-thione at 343 nm ($\epsilon_{343\,nm}$ = 8 080 $M^{-1}cm^{-1}$) [208].

GOx cross-linking with PM. The GOx(D70C) stock solution was reduced with TCEP (as described before) and removed using a PD midiTrap G-25 desalting column. Next, 5 µL of freshly prepared 30 mM PM in DMSO (abcr) was added to 995 µL of the freshly reduced protein solution (~1 mg mL^{-1}); the PM was added in approximately 10 times excess. The reaction was performed at pH 7.0, where the maleimide can predominantly react with free thiols [209]. The sample was incubated overnight at 4 ^{o}C and shaken at 500 rpm. The free PM was removed from the GOx(70C)-PM solution using a PD midiTrap G-25 desalting column with PBS (pH 7.4) (gibco, Life Technologies) equilibration buffer. The samples were stored at 4 ^{o}C.

Fluorescence spectrometry. GOx and GOx(70C)-PM fluorescence spectra were measured in a Varioskan LUX plate reader (ThermoFisher Scientific) in bottom-scanning plate reading mode. The samples were excited at 345±2.5 nm.

Preparation of GOx(70C)-PM-SWCNTs. 50 mg of SWCNTs (CoMoCAT (7,6)-enriched carbon nanotubes, Sigma Aldrich) were mixed with 50 mL of 2 wt% SC (Sigma Aldrich) and sonicated for 60 min using a tip sonicator (1/4 in. tip, QSonica Q700) at 1% amplitude in an ice bath. The SC-SWCNT suspension was ultracentrifuged at 164 000×g for 3 h (Beckman Optima XPN-80). Approximately 80% of the supernatant was collected and stored at room temperature. 0.5 mL of the 25 mg L^{-1} SC-SWCNT stock solution was mixed with 0.5 mL of ~3 mg mL^{-1} GOx(70C)-PM (or GOx). The suspension was subsequently dialyzed at 5 °C in a 14 kDa MWCO dialysis tube (D9777, Sigma Aldrich) in 2 L of PBS for 4 h. The dialyzed mixture was transferred to a 300 kDa MWCO dialysis device (Spectra/Por Float-A-Lyzer, Spectrum Laboratories) and dialyzed against 2 L PBS buffer for two days (during which, the buffer was replaced four times). The GOx(70C)-PM-SWCNTs were stored at 4 °C.

Absorbance spectroscopy. Spectra were acquired between 200 and 1350 nm using a UV-vis-NIR spectrophotometer (UV-3600 Plus, SHIMADZU). All measurements were performed in a quartz cuvette (10 mm, Quartz SUPRASIL, Hellma Analytics). SWCNT concentration was calculated using the extinction coefficient at 739 nm ($\epsilon_{739\text{nm}}$ = 25.3 mL mg^{-1} cm^{-1}) [127].

NIR fluorescence spectroscopy. A 96-well plate (costar 3590, Croning Incorporated) was filled with 49 µL of GOx(70C)-PM-SWCNT and GOx-SWCNT suspensions in PBS. NIR fluorescence spectra were taken between 950 and 1400 nm (75 l mm^{-1} grating) using the NIR micro-spectrometer described previously [19]. The samples were illuminated at 660±5 nm laser (SuperK Extreme EXR-15 and SuperK Varia, NKT Photonics). Fluorescence spectra were continuously acquired while 1 µL of 1 M glucose in PBS (pH 7.4) was added to the well. The fluorescence of the GOx(70C)-PM-SWCNT sensor in response to the addition and removal of a 20 mM glucose solution in PBS was performed in a glass-bottom device with a 14 kDa MWCO cellulose membrane (Sigma Aldrich) on top, as described in our previous work [19].

4.4 Results and discussion

4.4.1 Mutagenesis and expression of GOx

For the selected mutation sites were targeted non-conserved surface-exposed residues that were identified using sequence alignments of GOx homologues and the GOx crystal structure (PDB: 3QVP) [198]. We selected four positions (D70, H446, A418, and K13) that represent different distances from the glucose-binding cavity of the enzyme (**Figure 4.1a**).

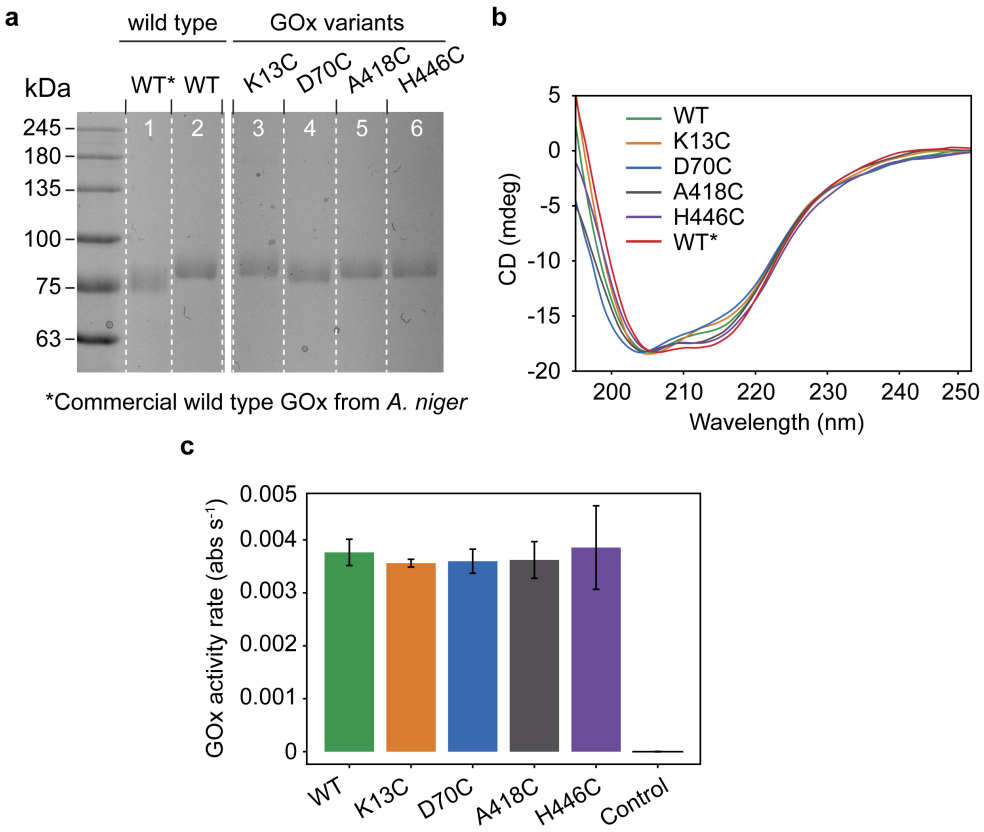

Figure 4.2 – Characterization of expressed and purified GOx variants. **(a)** Coomassie-stained SDS-PAGE of purified GOx (lanes 2 - 6) from *P. pastoris* compared with the commercial wild type GOx from *A. niger* (lane 1) (denoted as WT*). **(b)** CD spectra of GOx variants from *P. pastoris* and a commercially available wild type GOx from *A. niger*. **(c)** Relative activity rates of GOx towards glucose as measured by the ABTS colorimetric assay. The enzyme was omitted in the control sample. The error bars indicate standard deviations among technical triplicates.

Wild type GOx and the K13C, D70C, A418C, and H446C variants were expressed in an optimized *P. pastoris* production yeast strain [210, 211], which contains a protein N-glycosylation pathway that is similar to that found in human cells [212]. The SDS-PAGE analysis results shown in **Figure 4.2a** confirm an expected protein size of (~85 kDa). The recombinant GOx from *P. pastoris* show a slight increase in the apparent molecular compared to the commercial GOx from *A. niger* (~80 kDa) (lane 1). This difference is attributed to the greater degree of glycosylation [213]. The secondary structure was characterised with the CD measurements shown in **Figure 4.2b**. All structures, including the expressed wild type, commercial wild type, and mutants, share similar CD spectra. The expressed proteins contain 17 - 28% α-helices and 16 - 22% β-strands (**Figure D.2**), in accordance with values reported for the commercial GOx (24% and 17% for α-helixes and β-strands, respectively) and with the protein crystal structure (PDB 1CF3, 27% and 19% α-helixes and β-strands, respectively) [199]. These results confirm that the mutations did not significantly disrupt protein folding. The preservation of enzymatic activity was also confirmed by comparing activities measured with the colorimetric

ABTS assay (**Figure 4.2c)**. As shown in the figure, the enzymatic activity towards glucose does not significantly differ between wild type GOx and the mutants, indicating that the mutations had no significant effect on activity.

4.4.2 Bioconjugation of GOx with thiol reactive crosslinkers

The accessibility of the targeted residues was compared based on their reactivity towards SPDP, which releases a conjugation reaction product, pyridine-2-thione, that absorbs at 343 nm [214]. Absorption spectra were measured over 120 min (**Figure D.5**) and the reactivity of free thiols was monitored through the increase of absorption at 343 nm (**Figure 4.3a**). A418C was identified as the most reactive cysteine mutant, with ~0.4 moles of SPDP reacted per mole of GOx, followed by the D70C (~0.3 moles of SPDP reacted per mole of GOx), and the K13C and H446C mutants (~0.2 moles of SPDP reacted per mole of GOx). As expected, the reduced wild type GOx did not react with SPDP.

Based on these results, the D70C variant was selected for immobilization onto the SWCNT using the conjugation strategy shown in **Figure 4.1b**. The absorbance measurements shown in **Figure 4.3b** confirm the presence of PM in the purified conjugated protein fractions. The conjugation of the PM linker to the GOx is also confirmed by the PM fluorescence measurements shown in **Figure 4.3c**. In agreement with previous observations, the PM linker emits fluorescence at 376 and 396 nm upon 345 nm excitation when a covalent bond is formed between the PM maleimide and the protein thiol [186]. Broad emission peaks at 480 and 495 nm also appear due to the proximity of the two pyrenes to one another (~10 Å) [215], indicating that the GOx(70C)-PM monomers were folded into dimers. In contrast, the wild type GOx showed no fluorescence.

Protein conjugation to the SWCNT surface was confirmed through both absorbance spectroscopy. Compared to SC-SWCNTs, both non-specifically adsorbed GOx(WT)-SWCNTs and GOx(70C)-PM-SWCNTs show red-shifted absorption peaks for the (7,5) and (7,6) chiralities (**Figure 4.3d**). The convoluted absorption peak of E_{22} (7,5) and E_{22} (7,6) SWCNTs shifted from 657 to 660 nm. The E_{11} (7,5) and E_{11} (7,6) SWCNT peaks shifted from 1045 to 1047 nm and from 1135 to 1138 nm, respectively. This shifting is attributed to the change in solvation due to the protein corona. In contrast to the GOx(WT)-SWCNTs, the GOx(70C)-PM-SWCNT sample shows additional absorption peaks that correspond to absorption of the PM linker. A comparison of the SWCNT fluorescence spectra shown in **Figure 4.3e** similarly shows distinct spectra for the GOx(WT)-SWCNT and GOx(70C)-PM-SWCNT samples. The E_{11} emissions of the (7,6) chirality were observed at 1153±1 nm, for GOx(70C)-PM-SWCNTs on 660 nm excitation. The emission peak of the GOx(WT)-SWCNTs was red-shifted 4±1 nm more than the GOx(70C)-SWCNT peak. This red-shifting suggests slightly increased surface coverage of GOx(70C)-PM-SWCNTs compared to the GOx-SWCNTs [188, 216].

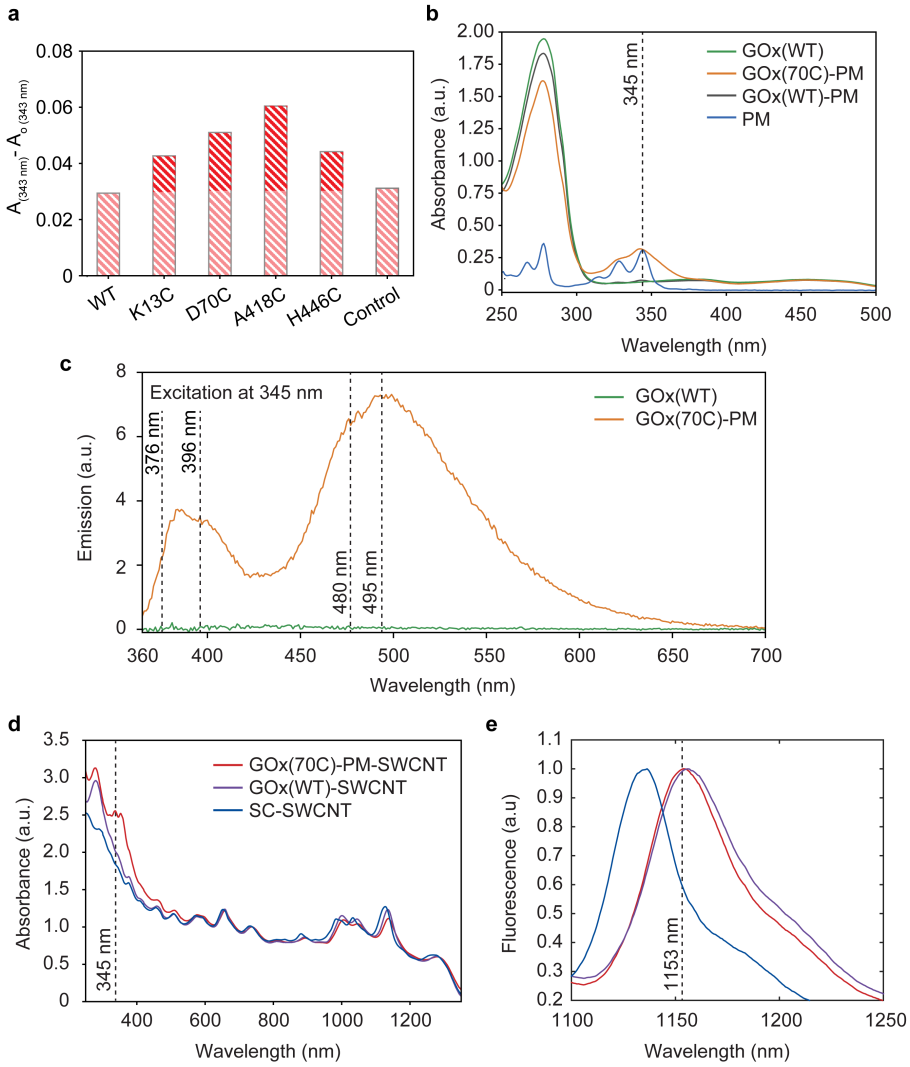

Figure 4.3 – Preparation and characterization of GOx-PM-SWCNTs. **(a)** Changes in absorbance at 343 nm for GOx variants measured before and after the addition of SPDP. The control sample contains the reaction mix without GOx. **(b)** UV-Vis absorbance spectra of GOx(WT) (green line), GOx(70C)-PM (orange line), GOx(WT)-PM (gray line), and PM (blue line). The absorption of the aromatic protein residues is seen at 280 nm. The broad peak at 450 nm corresponds to the absorption of FAD. GOx concentration in the samples was 0.5 mg mL^{-1}. The dotted line shows the PM absorbance peak maximum at 345 nm. **(c)** Emission spectra of GOx(WT) (green line), and GOx(70C)-PM (orange line) upon excitation at 345 nm. The GOx concentration in the samples was 0.5 mg mL^{-1}. The dotted lines show pyrene fluorescence peak maxima at 376 and 396 nm, and the pyrene excimer fluorescence at 480 and 495 nm. **(d)** UV-Vis-NIR absorbance spectra of GOx(70C)-PM-SWCNTs (red line) in comparison to the suspensions obtained with the non-specifically adsorbed GOx(WT)-SWCNTs (purple line), and SC-SWCNTs (blue line). The spectra were normalized to the SWCNT absorbance at 739 nm. The dotted line at 345 nm shows the PM absorbance peak. **(e)** Normalized fluorescence emission spectra of GOx(70C)-PM-SWCNTs (red line), GOx(WT)-SWCNTs (purple line), and SC-SWCNTs (blue line). Excitation at 660±5 nm. The dotted line shows GOx(70C)-PM-SWCNT fluorescence maxima of the E_{11} (7,6) SWCNT peak at 1153 nm.

4.4.3 Glucose detection using the GOx(70C)-PM-SWCNT sensor

The performance of the GOx(70C)-PM-SWCNT sensors was evaluated by monitoring the (7,6) fluorescence intensity peak at 1153±1 nm upon glucose addition (**Figure 4.4a**). In the presence of 20 mM glucose, we observe an increase in the fluorescence intensity. On the other hand, no fluorescence response was observed for the SC-SWCNTs. We explored the reversibility of this response using a device with a permeable membrane, as described in previous work (**Figure 4.4b**) [19]. A 20 mM glucose solution was added to the top of the device to trigger a response, and the device was washed with PBS after the signal reached a plateau to revert the response. Approximately 10 min after the addition of glucose, the fluorescence intensity increased by 60%, and buffer washing diminished the fluorescence back to its initial intensity. The experiment was repeated with the SC-SWCNTs (purple line). As expected, the intensity of SC-SWCNTs remained at the same level after the addition of the 20 mM glucose solution.

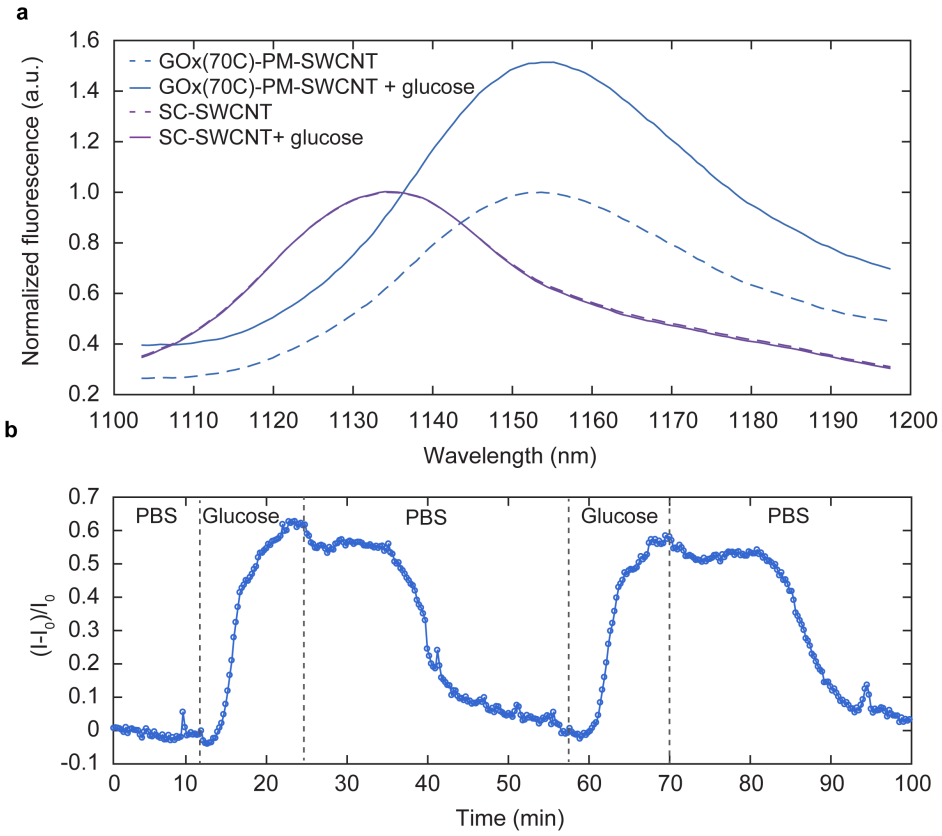

Figure 4.4 – NIR fluorescence response of the GOx-PM-SWCNT sensor towards glucose. **(a)** NIR fluorescence spectra of the GOx(70C)-PM-SWCNTs (blue line) and SC-SWCNTs (purple line) before (dashed lines) and 2 min after addition of 20 mM glucose (solid line). The (7,6) peaks were normalized to their maxima of the intensity before the addition of the glucose solution. Excitation at 660±5 nm. **(b)** The (7,6) peak intensity monitoring of GOx(70C)-PM-SWCNTs in a device with a glucose-permeable membrane. The 20 mM glucose solution in PBS was added on the top of the membrane and washed with PBS after the fluorescence reached a plateau. The fluorescence (I) was normalized to the intensity at 0 min (I_0) as: $(I\text{-}I_0)/I_0$.

4.5 Conclusion

In this chapter, we developed a glucose sensor using genetically-engineered GOx, which was immobilized site-specifically onto SWCNTs. Successful immobilization of GOx(70C)-PM onto SWCNTs was confirmed using absorbance and NIR fluorescence measurements. The slightly blue-shifted position the (7,6) SWCNT peak of the GOx(70C)-PM-SWCNTs in comparison to GOx(WT)-SWCNTs indicates denser coverage of the GOx(70C)-PM onto SWCNTs compared to the non-specifically adsorbed GOx. Moreover, the results reported in **Chapter 3** showed that the secondary structure of the protein is less when proteins attached to SWCNTs *via* the linker, which could be the case also for the GOx(70C)-PM-SWCNTs. The sensor shows a reversible response to a change of glucose, allowing the implementation of this sensor for continuous monitoring. Furthermore, the conjugation method proposed herein can be used to immobilize a range of bioengineered enzymes in an oriented manner to develop new SWCNT-based sensors.

5 Outlook towards portable fluorescence monitoring device

5.1 Abstract

In this chapter is demonstrated a portable device for fluorescence monitoring of SWCNT-based sensors. Production costs and its dimensions are requirements for the commercial realization of NIR point-of-care diagnostics, therefore, we address that in this study. The NIR light detection is enabled through the total internal reflection (TIR)-based illumination of SWCNTs by a generated evanescent wave. The NIR fluorescence from the SWCNTs is detected through a Dove prism by an InGaAs photodetector. The prototype demonstrated its application for SWCNT-based sensing and a cost-effective solution for NIR fluorescence monitoring. This versatile device can be used with a variety of SWCNT sensors for detecting analytes in blood or serum.

5.2 Introduction

Autonomous health monitoring systems can help not only in treating diseases but also in improving the everyday life of healthy people. These systems provide a means for monitoring important biomolecules in clinics or at homes using point-of-care devices. Fluorophores such as semiconducting SWCNTs offer increased photostability and have been demonstrated as versatile sensing materials. SWCNTs have enhanced optoelectronic properties, fast kinetics, and a large surface area, that can be used for immobilization of analyte-selective

molecules. Therefore, SWCNT-based sensors typically have higher sensitivities and lower limits of detection compared to conventional fluorescence sensors [178].

Furthermore, SWCNT-based sensors show a wide range of sensing applications. SWCNT sensors were successfully employed to detect dopamine, cholesterol, insulin, and glucose [19, 217, 218]. Until now, the responses of these sensors were monitored using large laboratory devices, such as the NIR fluorescence microscopes presented in **Chapter 1**. To date, only two research groups have demonstrated epi-fluorescence optical sensing devices employing SWCNTs [219, 220], and to the best of our knowledge, studies so far have yet to demonstrate SWCNT-based optical sensing using a portable setup suitable for point-of-care diagnostics. In this work, we present a new concept towards achieving portable detection based on TIR NIR fluorescence from SWCNTs.

5.3 Materials and methods

TIR NIR fluorescence detection device. The device has a LuxX 660 nm laser illumination source (Ocean Optics). The laser beam goes through a polished Dove prism (Thorlabs) to illuminate a SWCNT suspension using an evanescent wave, which is generated on the surface of a coverslip (Electron Microscopy Sciences). The SWCNT suspension is administrated into a well that is made on the top of the coverslip. The cover glass is placed on the top of the Dove prism after adding a drop of immersion oil (Type A, Nikon) between the glass surfaces. The SWCNT fluorescence was monitored through the prism using a 30 mm lens (AC254-030-C, Thorlabs) that is optimized for transmission of the light between 1050 and 1700 nm. A long-pass 980 nm filter (Semrock) was inserted in the optical path. The 30 mm lens focuses the light on an InGaAs photodiode PDA10C/M (Thorlabs), and the recorded fluorescence signal is digitalized using an Arduino UNO microcontroller (Arduino). The signal is continuously read out and transmitted to a computer, where it is analyzed using a custom-built Python script which was developed in collaboration with the group of Prof. B. S. Sreeja from the Sri Sivasubramaniya Nadar (SSN) College of Engineering in India. A DFK 72AUC02 camera (The Imaging Source Europe) was used for the alignment of the illumination beam and focusing.

SWCNT fluorescence monitoring. (7,6)-Enriched CoMoCAT carbon nanotubes were mixed with 2 wt% SC (Sigma Aldrich) to yield the final concentration of 1 mg per 1 mL of the solution. The mixture was sonicated for 60 min using a QSonica Q700 (using 1/4 in. tip) sonicator in an ice bath. The resulting SC-SWCNT suspension was ultra-centrifuged at 164 000 × g for 3 h (Beckman Optima XPN-80). The collected supernatant had a SWCNT concentration of 43 mg L^{-1} (ϵ_{739nm} = 25.3 mL mg^{-1} cm^{-1}) [127]. Next, 29 µL of the SC-SWCNT suspension was added to the well on the coverslip. The SWCNT fluorescence was continuously monitored using the TIR NIR device. 1 µL of freshly prepared 1 M $K_3Fe(CN)_6$ solution (Sigma) or 1 µL of water (control) was added to the well. The recorded SWCNT fluorescence intensity (I) was normalized to the intensity before the addition of the solution (I_0): $(I-I_0)/I_0$.

5.4 Results and discussion

The TIR NIR device was assembled according to the illustration shown in **Figure 5.1a**, and a photo of the setup is shown in **Figure 5.1b**. The device was used to demonstrate fluorescence quenching of the SC-SWCNT suspension after the addition of 33 mM $K_3Fe(CN)_6$. The SC-SWCNT suspension was loaded in the well on the coverslip placed of the top of the Dove prism, as it is shown in **Figure 5.1c**. The suspension was continuously illuminated with the 660 nm light, and the SWCNT fluorescence was monitored in the NIR-II window above 1050 nm. When $K_3Fe(CN)_6$ solution was added to the SC-SWCNTs the fluorescence of SWCNT was gradually decreasing. $K_3Fe(CN)_6$ adsorb onto the SWCNT surface and withdraws electrons from SWCNTs that causes quenching of the fluorescence intensity [13]. ~80 s after the addition of $K_3Fe(CN)_6$, the signal intensity decreased by 7% from the initial intensity I_0 (orange line, **Figure 5.1d**). To confirm that the addition of a solution itself does not induce a decrease of the signal (dilution of the SC-SWCNT suspension) we added the same volume of water to the new SC-SWCNTs sample. As expected, the fluorescence signal remained at its initial intensity level (green line). Were observed fluctuations in the signal intensity during the addition of the solutions due to the mixing of the SC-SWCNT suspension with a pipette tip (the first 10 s of signal recording).

Recently, epi-fluorescence NIR setups were demonstrated for measuring protein dissociation constants or enzymatic activities *via* SWCNT sensors [219, 220]. Here, for the first time, was demonstrated the portable TIR NIR device for monitoring fluorescence of SWCNTs that benefits from several advantages:

First, the generated evanescent wave propagates ~100 nm from the surface of the glass, and SWCNTs that are present within this layer are excited and fluoresce. Therefore, the TIR configuration can reduce the volume of SWCNTs needed for a single measurement by coating the coverslip with a few hundreds of nanometers thick the sensing layer. The immobilization of the SWCNTs on disposable glass coverslips could allow making cost-effective test carriages for analyte detection.

Second, the TIR layout minimizes the risk of exposure from the laser beam when the device is enclosed in a case isolates the laser beam, and only the top of the Dove prism is accessible to the end-user for sample administration. This configuration is not possible with epi-florescence detection devices, where the illumination beam is passing through the sample. This advantage could be necessary for the safety of the device user.

Finally, the price of the device can be affordable for small size clinics or pharmacies that perform point-of-care tests. Compared to a conventional NIR microscope, which costs around 100 000 CHF, our TIR NIR device offers a cost-effective options that costs ~7 000 CHF (**Table 5.1**). The product costs could be further reduced by simplifying the layout of the device and negotiating better deals with optical component manufactures.

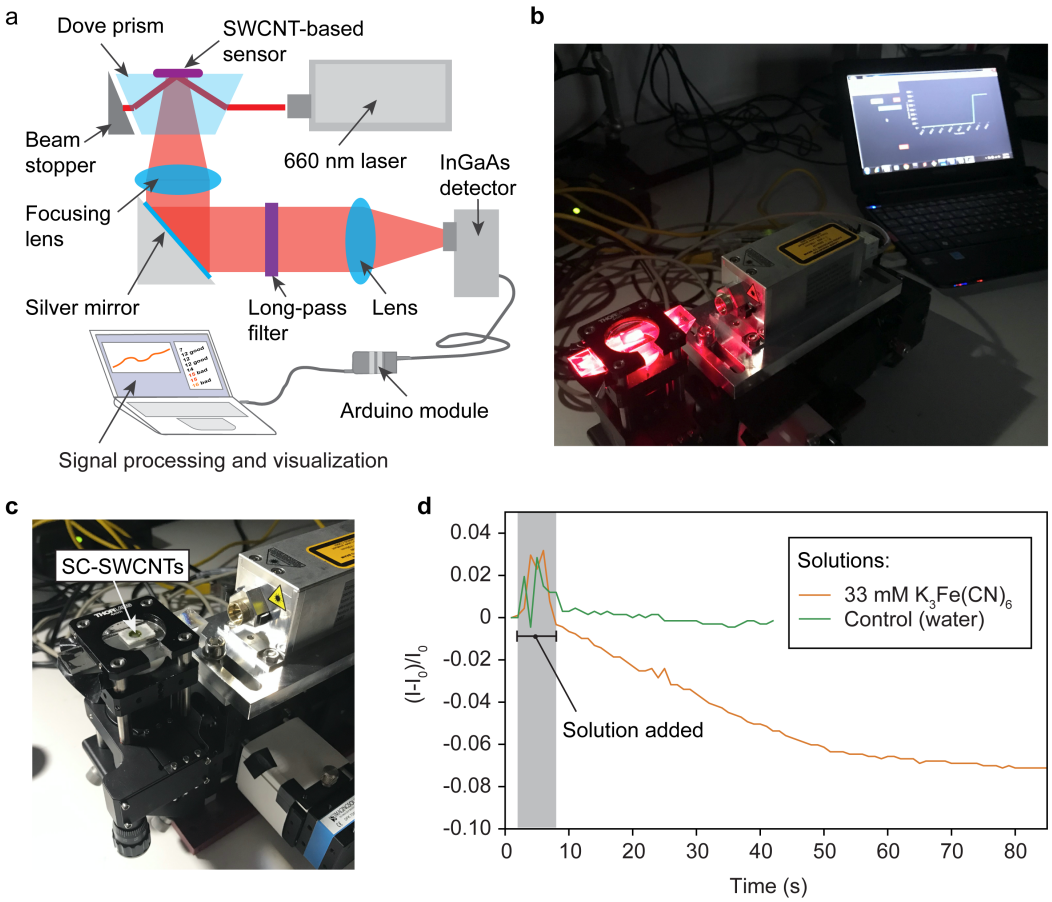

Figure 5.1 – TIR NIR fluorescence monitoring device. **(a)** Illustration of the optical layout for the TIR NIR fluorescence device. **(b)** Photo of the working prototype of the device. **(c)** The photo showing the SC-SWCNT suspension which was loaded in the well on coverslip placed on the Dove prism. **(d)** Fluorescence response of SC-SWCNTs after addition of $K_3Fe(CN)_6$ to a final concentration of 33 mM (orange line). The control experiment was performed by adding the same volume of water to the SC-SWCNTs (green line).

Although this prototype offers a powerful demonstration for a commercial realization, several modifications are needed to optimize the device further.

First, in the commercial prototype, the laser power output characteristic can be downgraded since good signal-to-noise can be obtained using a cheaper and lower power laser. The device can be upgraded with a customized focusing optics that will reduce the costs and provide better control of the illumination beam.

Second, the optical components of the device could be isolated from ambient light exposure. It will improve the signal-to-noise and protect the user from accidental exposure by the illumination beam.

Third, the fluorescence intensity of SWCNT-sensors can be enhanced using covalently doped

SWCNTs, which have significantly higher QYs compared to the ones used in this study [221]. However, covalently doped SWCNTs is not yet commercially available, but this could change soon.

Table 5.1 – Prices of the optical components used in the TIR NIR device

Nb.	Item	Price in CHF
1	InGaAs detector PDF10C/M (Thorlabs)	706
2	Two AC254-030-C lenses (Thorlabs)	200
3	Polished Dove prism (Thorlabs)	181
4	980 nm long-pass filter (Semrock)	425
5	LuxX 660 nm laser (Ocean Optics)	4770
6	Silver mirror (Thorlabs)	70
7	Axial translation mount	200
8	Filter mount	160
9	Silver mirror holder	200
10	Cage system mounts	170
	Total price:	**7082**

5.5 Conclusion

In this chapter, we show the proof-of-concept device for NIR fluorescence monitoring. The device could be employed in point-of-care testing using a variety of SWCNT-based sensors. We have consulted the cost of the demonstration prototype, and the device could be affordable for small clinics or pharmacies. We hope that SWCNT-based sensors will be soon available for users and will improve the quality of healthcare.

General conclusion and perspectives

In this thesis, non-covalent methods for carbon nanotube surface functionalization were explored. One advantage of using non-covalent functionalization is that it preserves the fluorescence properties of the SWCNTs. These methods were used to develop SWCNT-based sensors for optical glucose monitoring.

Throughout this project, I developed customized optical setups for monitoring fluorescence of SWCNTs, explored methods for SWCNT surface functionalization, carried out the expression of bioengineered proteins, and demonstrated the application of SWCNT-based sensors for continuous glucose detection. The results presented within this thesis demonstrate various experimental techniques for functionalizing the carbon nanotube surface. Nanotubes prepared using these methods can be applied in areas beyond optical sensing, for example, as NIR imaging agents (when coated with proteins), therapeutic agents for cancer treatment, electrochemical sensors, or targeted protein-based carbon nanotube intra- or extra-cellular delivery [72].

Future research on the sensors developed in this thesis will focus on demonstrating their biocompatibility. That involves, creating protocols for protein-nanoparticle sterilization and storage of the sensor under sterile conditions. Promising approaches for this purpose include UV light or radiation-based sterilization techniques. However, these sterilization methods might reduce the activity of the protein-based sensor. Therefore, this investigation remains the subject of further research. Following promising results from *in vitro* testing, it will be necessary to test the sensor embodiment *in vivo* on animal models (e.g. rodents). For this purpose, I propose immobilizing GOx-PM-SWCNTs into capsules with a glucose permeable membrane or embedding them within a hydrogel matrix. An important objective of this study will be to find out whether the sensitivity of the sensor will be affected due to the immune system's response.

The site-specific crosslinker-based immobilization was identified as the most promising method for attaching a protein onto the sidewall of the SWCNT. This method achieved a higher degree of protein retention onto SWCNTs in comparison to the ssDNA-linker-based immobilization approaches. Moreover, the use of these PM-linkers is advantageous over the non-specific protein adsorption because it reduces the degree of its unfolding. In this work, protein immobilization was demonstrated on EYFP and bioengineered GOx variants.

Nevertheless, this technology is not limited to application with these proteins and can be extended to other proteins, for example, cholesterol oxidase (ChOx) or lactate oxidase (LaOx), to develop new optical sensors. In combination with high throughput screening and protein engineering, new SWCNT-based sensors could be identified in a time-effective way. For example, our laboratory recently proposed directed evolution as a method for optimizing the optical properties of ssDNA-SWCNT composites [222], this method could be adapted for screening activity of protein-SWCNT sensors.

Protein and SWCNT composites can also be used in creating multianalyte-sensing platforms. SWCNTs have different chiralities exhibiting discrete fluorescence peaks, which can be functionalized with different analyte-specific molecules. That can enable the detection of numerous responses simultaneously by spectroscopic means. Similar to the multi-peak detection approach was demonstrated by *Heller et al.* [223]. Recent progress in SWCNT synthesis and purification methods has enabled higher yields for particular chirality species [14, 224]. Single-chirality SWCNTs are required for their chirality-dependent functionalization for the multianalyte-sensing platforms.

In **Chapter 5**, I designed and assembled a prototype of the TIR NIR fluorescence device. The proof-of-concept was shown in the SC-SWCNT fluorescence quenching experiment in the presence of $K_3Fe(CN)_3$. The component costs for the device assembly were significantly reduced in comparison to the conventional NIR fluorescence microscopes that are typically used for monitoring SWCNT-based sensors. This portable device can potentially be used for rapid blood sample analysis in clinics or pharmacies. The next objective is to demonstrate the allocation of this optical device for glucose detection using the GOx-PM-SWCNT sensor.

In conclusion, the work reported in this thesis expanded our knowledge on protein-SWCNT functionalization and demonstrated the application of the SWCNT-based optical sensors towards continuous glucose monitoring. This technology is promising for long-lasting glucose sensors, which can be used for automatic, closed-loop insulin delivery pumps, and can revolutionize the way people with diabetes manage their disease. Moreover, versatile SWCNT sensors can be used for analyte testing in the portable TIR NIR device, as it has been demonstrated in this thesis.

Appendix

A Optical systems for NIR imaging and spectroscopy

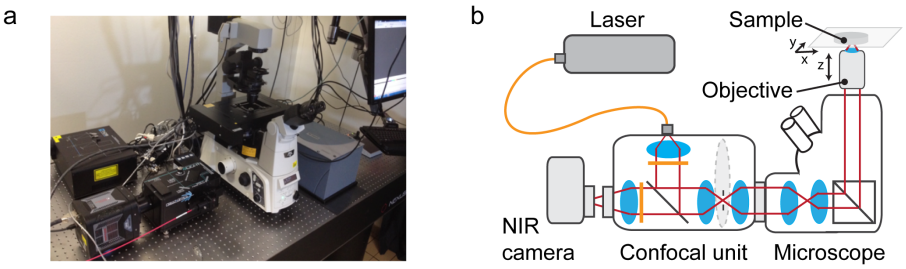

Figure A.1 – Spinning-disc confocal NIR microscope. (a) An image and **(b)** optical layout of the confocal spinning-disc NIR microscope.

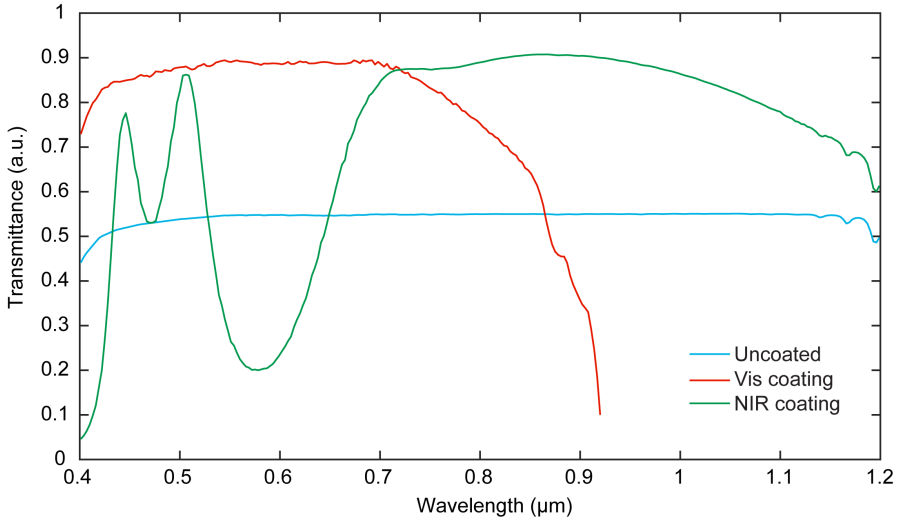

Figure A.2 – Transmission of the excitation light paths. Measured for a standard production unit, IR optimized unit, and IR unit with uncoated lenses. Glass absorption, Fresnel losses, and mirror coatings are considered.

Table A.1 – Data obtained from fitting the lateral FWHM of the NIR beads using PSFj software in the wide-field and confocal microscope settings

Nb. of beads	Wide-field FWHMx (µm)	Confocal FWHMx (µm)
1	0.823	0.377
2	0.542	0.758
3	0.524	0.456
4	0.523	0.497
5	0.591	0.337
6	0.471	0.556
7	0.526	0.415
8	0.525	0.466
9	0.449	0.451
10	0.450	0.411
11	0.438	0.353
12	0.492	0.401
13	0.445	0.377
14	0.448	0.406
15	0.434	0.507
16	0.506	0.389
17	0.874	0.387
18	1.095	0.402
19	0.619	0.384
20	0.635	0.398
21	0.790	0.526
22	0.720	0.466
23	0.641	0.798
24	0.588	0.539
25	0.481	0.542
26	0.601	0.387
27	0.475	0.768
28	0.569	0.670
29	0.691	0.540
30	0.470	0.588
31	0.515	0.486
32	0.572	0.405
Average FWHM (µm)	**0.6**	**0.5**
Standard deviation (µm)	**0.1**	**0.1**

Table A.2 – Data obtained from fitting the axial FWHM of the NIR beads using PSFj software in the wide-field and confocal microscope settings

Nb. of beads	Wide-field FWHMz (µm)	Confocal FWHMz (µm)
1	1.115	0.481
2	0.982	0.678
3	1.019	0.550
4	1.154	0.568
5	0.953	0.591
6	0.937	0.843
7	1.141	0.516
8	1.067	0.556
9	0.814	0.517
10	1.069	0.601
11	0.878	0.498
12	1.238	0.531
13	0.971	0.513
14	1.066	0.581
15	1.113	0.585
16	1.319	0.515
Average FWHM (µm)	**1.1**	**0.6**
Standard deviation (µm)	**0.1**	**0.1**

The signal-to-noise ratio (SNR) was calculated according to **Equation A.1** [225], where n_s is the intensity of a single NIR bead, n_b is the mean intensity of the background, and σ_b is the standard deviation of the background intensity.

$$SNR = \frac{n_s - n_b}{\sigma_b} \tag{A.1}$$

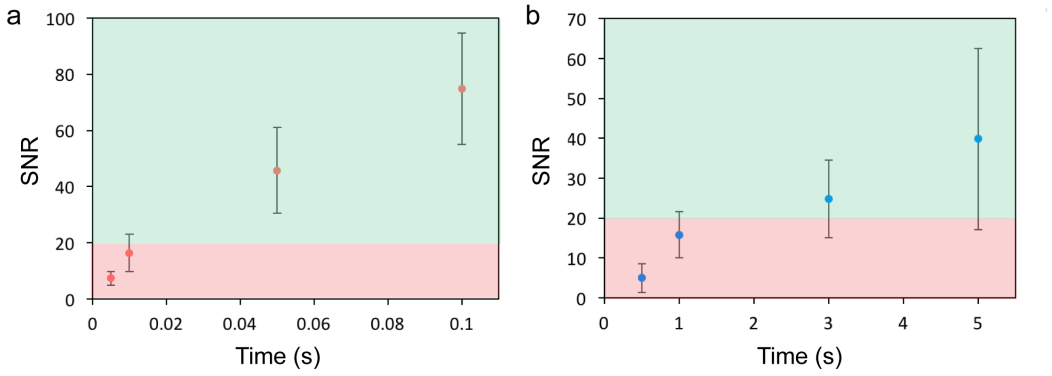

Figure A.3 – SNR dependence on a frame acquisition time. Demonstrated for **(a)** single NIR beads and **(b)** single SWCNTs. Images were recorded in the confocal configuration (excitation at 780 nm, laser illumination power was 1.8 W cm^{-2}). Images that have SNRs greater than 20 (indicated in the green region) are considered suitable for fluorescence microscopy measurements.

B Mediator-free optical GOx-SWCNT glucose sensor

0.3, 1.3, 5.0, 15.0, and 30.0 mg of the dry GOx powder from *A. niger* (batch SLBN9716V, Type II, 19440 U g^{-1}, Sigma Aldrich) were each dissolved in 1 mL of the SC-suspended SWCNT and stirred for 2 h at room temperature. The mixtures were then transferred into wet dialysis tubes with a 14 kDa MWCO (cellulose membrane, Sigma Aldrich) and dialyzed against 1.5 L PBS (pH 7.4, Sigma Aldrich) for 4 h at room temperature to remove SC, allowing the nonspecific adsorption of GOx. The suspensions are shown in **Figure B.1**.

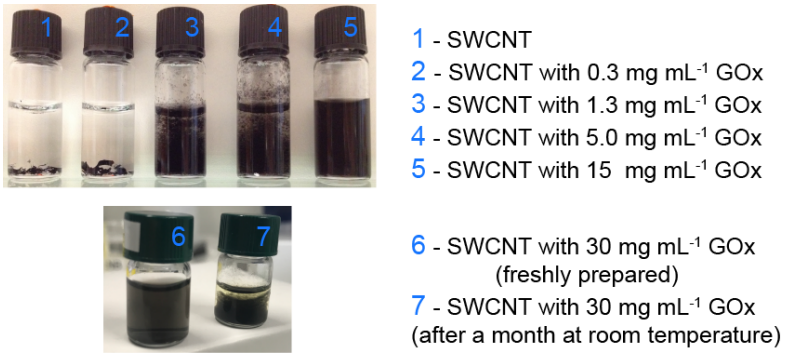

Figure B.1 – Dialysis of the GOx-SWCNT suspensions. The suspension prepared by varying concentrations of the dry GOx powder dissolved in PBS. The amount of GOx units in the dry GOx powder was 19440 U g^{-1}.

The results show that GOx can disperse SWCNTs (33 ± 1 mg L^{-1}) at concentrations above 0.3 mg mL^{-1}. While enzyme concentrations between 1.3 and 15.0 mg mL^{-1} can disperse SWCNTs, we found that the SWCNTs in these suspensions formed aggregates few days after preparation. The 30.0 mg mL^{-1} solution exhibited the strongest fluorescence. If a SWCNT surface area of 1315 m^2 g^{-1} is assumed and GOx was modeled as a spherical particle with a diameter of 8.6 nm, the minimum concentration required to solubilize the SWCNTs is approximated to be over 100 times the amount of GOx needed to cover the SWCNT surface with GOx completely [226].

The solution was stored at 4 °C and equilibrated to room temperature before the measurement.

After incubation at room temperature for one month, the GOx-SWCNT suspension showed signs of aggregation and sedimentation (**Figure B.1**, 7).

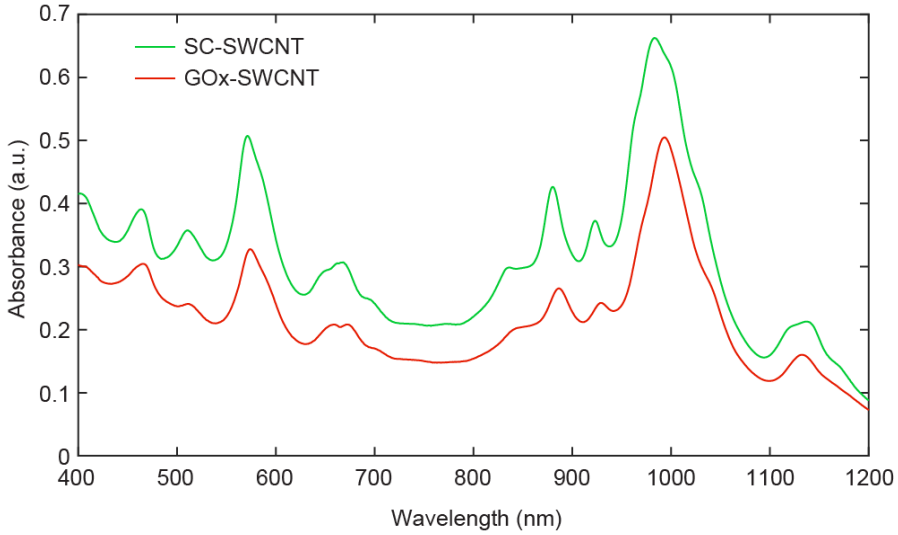

Figure B.2 – Absorbance spectra of SC-SWCNTs (green) and GOx-SWCNTs (red).

To remove the free enzyme from the suspension, the 30.0 mg mL^{-1} GOx-SWCNT solution was transferred to a 300 kDa dialysis device (Spectra/Por®Float-A-Lyzer®, Spectrum Laboratories), and the sample was dialyzed overnight at room temperature against 1.5 L of PBS. Absorbance spectra (UV-3600 Plus, SHIMADZU) of the SWCNT suspensions were recorded before and after dialysis (**Figure B.2**). Previous studies have reported that GOx adsorption on the SWNCT surface increases the accessibility of water to the SWCNT surface, causing a shift of the absorbance and fluorescence peaks [13]. Our results are in agreement with these reports, as we observed a 10±1 nm and 3±1 nm red-shifting of the E_{11} (6,5) and E_{22} (6,5) absorbance peak maxima, respectively.

The direct addition of glucose solution to the sensor diluted the SWCNT suspension and yielded in a slight decrease of the fluorescence intensity due to dilution. The dilution effect can be accounted for by subtracting the fluorescence decrease upon PBS addition in the absence of glucose. Accounting for dilution in this manner shows that the observed decrease in the negative controls (SC-SWCNT) is statistically negligible (**Figure B.3**).

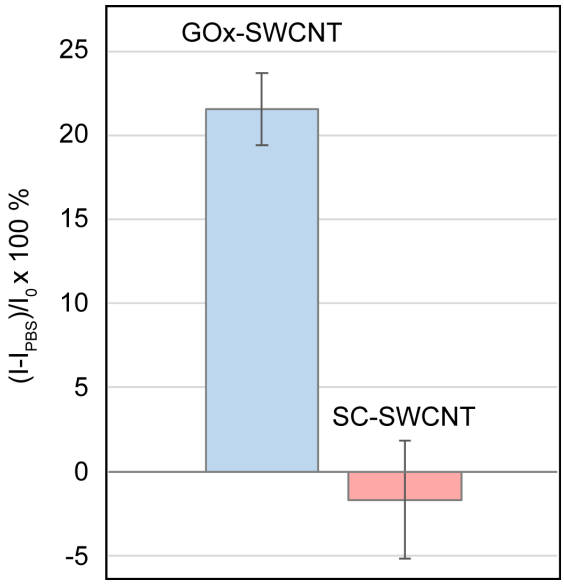

Figure B.3 – Changes in normalized fluorescence intensity of GOx-SWCNTs and SC-SWCNTs 3 min after the addition of 15 mM glucose. The change (6,5) SWCNT peak intensity maxima at 995±1 nm were calculated using the following equation: $(I - I_{PBS}) / I_0 \pm 100\%$, where (I_0) is the initial intensity and (I) is the intensity measured after 3 min. Measurements were taken in technical triplicates. Excitation at 575±5 nm.

The ABTS colorimetric assay was used to determine GOx activity in response to different saccharides. Briefly, the test solution was prepared by mixing a GOx solution (15 µL, 30 mg mL^{-1}), sodium citrate buffer (119.8 µL, 50 mM, pH 5.75, Sigma Aldrich), ABTS (40 µm, 20 mM, Bio-Chemica) in 20 mL sodium citrate buffer (pH 5.75), horseradish peroxidase solution (0.2 µL, 2 mg mL^{-1}, HRP, Type-VI-A, Sigma Aldrich), and 80 µL of different saccharide solutions (30 mM, D-glucose, D-mannose, D-maltose monohydrate, D-fructose, D-xylose) were each added to the different wells of a 96-well plate. The plate was incubated for 1 h, and photos of the wells were taken after 3 min, 15 min, 30 min, and 1 h (**Figure B.4**). The intensity of green color indicates the level of GOx enzymatic activity towards the tested saccharides.

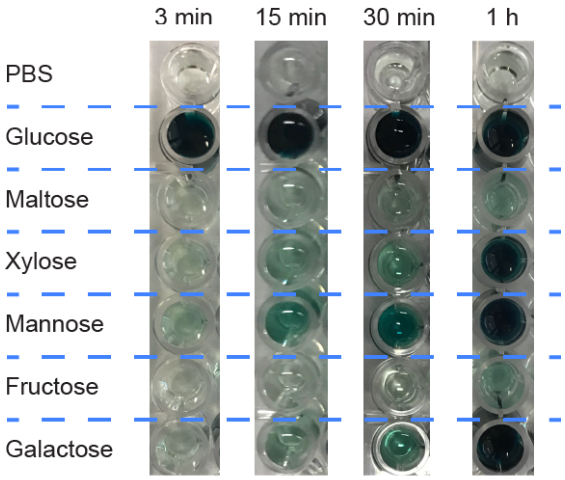

Figure B.4 – Images of wells in the absence (PBS) and presence of glucose, maltose, xylose, mannose, and fructose in PBS. Images were taken 3 min, 15 min, 30 min and 1 h after the saccharides were added to the ABTS colorimetric assay.

Figure B.5a shows fluorescence spectra of the GOx-SWCNTs after addition of 15 mM glucose, mannose, galactose, maltose, fructose, and xylose solutions. Control measurements only in the presence of PBS ("0 mM glucose") were also taken, and a comparison of the (6,5) SWCNT peak intensities is shown in **Figure B.5b**. The measurements were performed in triplicates shown in **Figure 2.3b**. The evolution of the (6,5) SWCNT peak intensity after addition of 50 µL PBS or 30 mM saccharide (to the final concentration of 15 mM) to the wells with 50 µL of the GOx-SWCNTs is shown in **Figure B.6**.

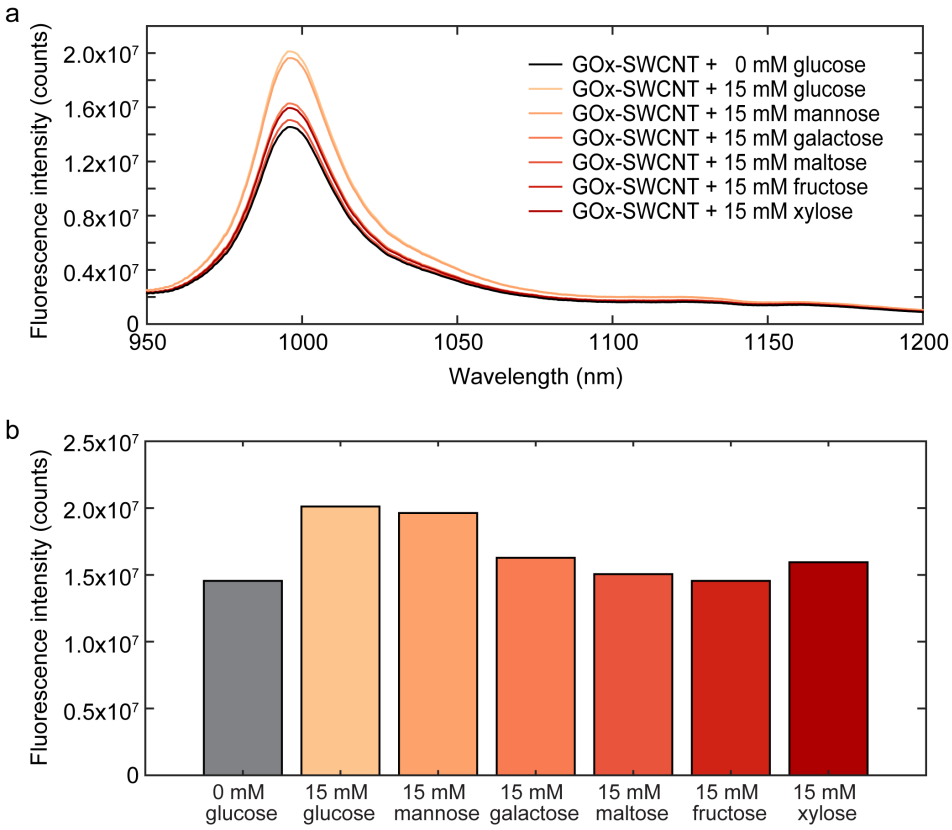

Figure B.5 – Response of the GOx-SWCNT sensor to the saccharides. (a) Fluorescence spectra of GOx-SWCNTs recorded 3 min after addition of 15 mM glucose, mannose, galactose, maltose, fructose, or xylose. **(b)** Comparison of the (6,5) SWCNT peak intensities shown in (a). Excitation at 575 ±5 nm.

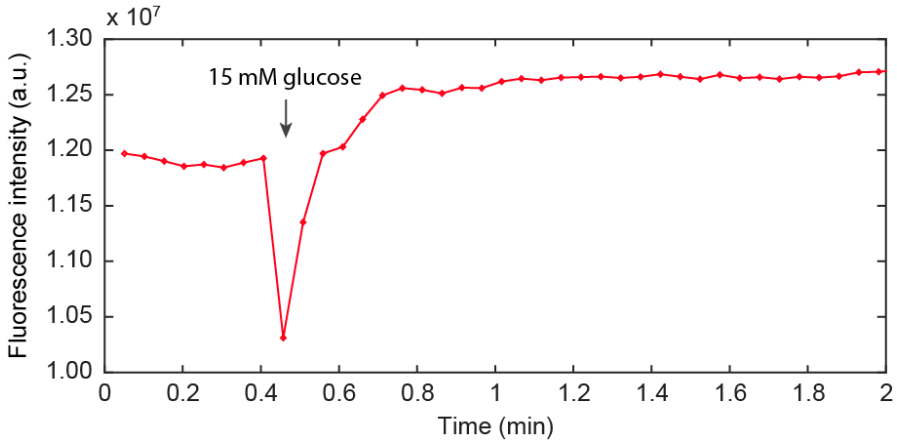

Figure B.6 – Response of the GOx-SWCNT sensor to glucose. Fluorescence intensity of the GOx-SWCNTs plotted over time. 50 µL of 30 mM glucose was added to the well containing 50 µL of the GOx-SWCNTs (the final concentration of glucose was 15 mM). Excitation at 575 ±5 nm.

The normalized fluorescence intensities of the GOx-SWCNTs were derived, and the values were fitted to a Gaussian function (MATLAB *'gauss1'*) (**Figure B.7**). The maxima of the Gaussian fit were used to calculate the rate of change in fluorescence intensity.

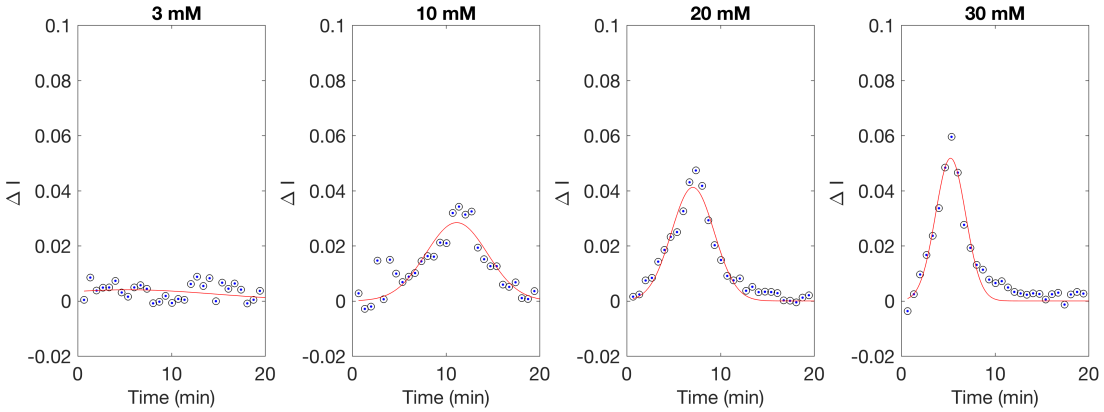

Figure B.7 – Derivatives (blue dots) and fitted curves (red lines) of the GOx-SWCNTs after addition of 3, 10, 20, and 30 mM glucose.

The device with a glucose permeable membrane was attached to the bottom of a polypropylene beaker (**Figure B.8a**). The beaker had an opening in its bottom to which the device was glued. GOx-SWCNTs were loaded in the sensor device. The 14 kDa MWCO membrane separated the buffer (30 mL of PBS) in the beaker and the sensor element. The device was illuminated from the bottom at 575±5 nm. A pH sensor (InLab®Expert Pro-ISM pH, Seven Compact pH meter, Mettler Toledo) was immersed into the buffer, which was mixed at 2 000 rpm (Polytron®PT 1300 D, Metrohm). During the measurements the buffer's pH was changed from 7.40 to 9.81 using 0.5 M NaOH (Sigma Aldrich) and from 9.81 to 3.68 using 0.5 M HCl (Merck KGaA). Fluorescence spectra were recorded throughout at different pH (the buffer was mixed for 4 min at each pH point before taking the measurement). Maxima of the GOx-SWCNT (6,5) peak intensities were plotted *vs.* pH values (**Figure B.8b**). Finally, the pH was set to 7.25 and glucose powder was added to the buffer which stimulated an increase in the fluorescence intensity (the red point on **Figure B.8b**).

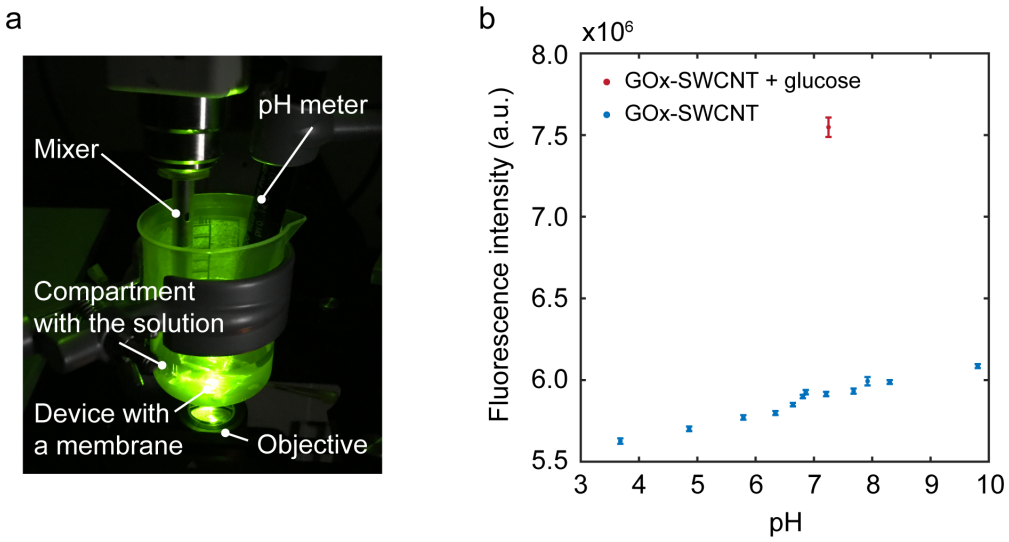

Figure B.8 – Fluorescence of the GOx-SWCNTs at different pH values. (a) Image of the setup used to perform the measurements. The beaker had a hole at the bottom with the sensor device attached to it, where the GOx-SWCNT suspension was loaded to. A glucose permeable membrane separated the buffer in the beaker and the device. **(b)** Fluorescence intensities of the GOx-SWCNTs at different pH (blue) and after addition of glucose (red). The pH was equilibrated for 4 min before each measurement. Excitation at 575±5 nm.

In **Figure B.9**, Raman spectra are shown. They were measured before (0 min) and 5, 10, 15, 20 min after addition of 7 mM glucose (0.1 µL of 3.5 M glucose added to 50 µL of the GOx-SWCNTs). The sample was illuminated with the 532 nm laser, achieving the 3.7 mW power at the sample plane (a 50x objective (Leica), 1800 lines mm^{-1} grating, Renishaw inVia Raman Microscope). 20 min after the glucose solution was added the RBM peak at 275 cm^{-1} down-shift for 1.2 cm^{-1}.

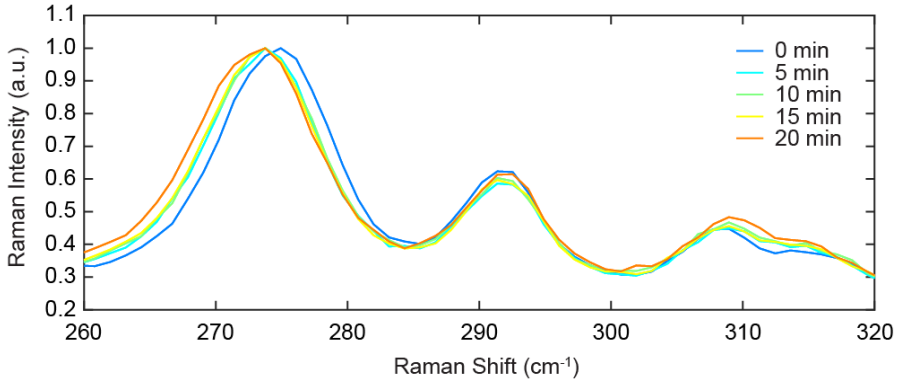

Figure B.9 – Raman spectra in the RBM region (between 260 and 320 cm^{-1}) for GOx-SWCNTs before (0 min) and 5, 10, 15, 20 min after addition of 7 mM glucose. The sample was illuminated at 532 nm.

C Non-covalent bioconjugation of proteins to SWCNTs

Table C.1 – Primers used for construction of recombinant plasmids in EYFP expression

Primer	Primer sequence (5' to 3')	Size (bp)
Xho-N-EYFP-R	ATA CTC GAG CTT GTA CAG CTC GTC CAT G	28
Nde-N-EYFP-F	ATA CAT ATG GTG AGC AAG GGC GAG GAG	27
Nde-C-EYFP-F	ATA CAT ATG TGC GTG AGC AAG GGC GAG GAG	30
Xho-C-EYFP-R	ATA CTC GAG GCA CTT GTA CAG CTC GTC CAT G	31

Table C.2 – PCR methods for plasmid preparation

Nb.	PCR method
Method 1	Step 1: 98 ^{o}C for 30 s Step 2 (33 cycles): 98 ^{o}C for 10 s; 52 ^{o}C for 15 s; 72 ^{o}C for 30 s Step 3: 72 ^{o}C for 3 min; 4 ^{o}C
Method 2	Step 1: 95 ^{o}C for 3 min Step 2 (33 cycles): 95 ^{o}C for 15 s; 55 ^{o}C for 15 s; 72 ^{o}C for 15 s Step 3: 72 ^{o}C for 30 s; 4 ^{o}C

Table C.3 – Protocols for preparation of media used for cell cultures

Type	Preparation protocol
LB growth medium (for 1 L):	10 g of tryptone (Sigma) 5 g of yeast extract (Becton Dickinson and Company) 10 g of NaCl (Sigma) pH adjusted to 7.0 and sterilized in an autoclave
LB medium and agar:	agar added to the LB medium at concentration of 15 g L^{-1}

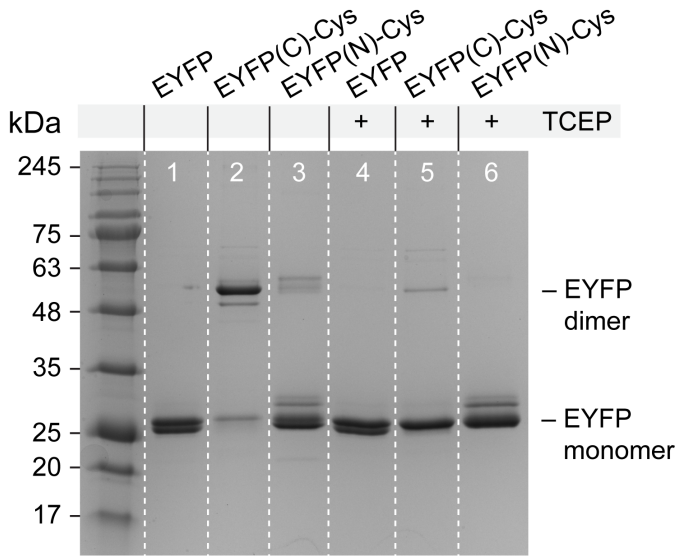

Figure C.1 – SDS-PAGE analysis of purified EYFP, EYFP(C)-Cys, and EYFP(N)-Cys before and after reduction with 10 mM TCEP. The non-reducing gel electrophoresis performed on the 12% polyacrylamide gel at 100 V for 10 min and at 250 V for 30 min. The gel was stained with the Coomassie Brilliant Blue dye (ITW Reagents). A protein marker IV was used as the reference (AppliChem).

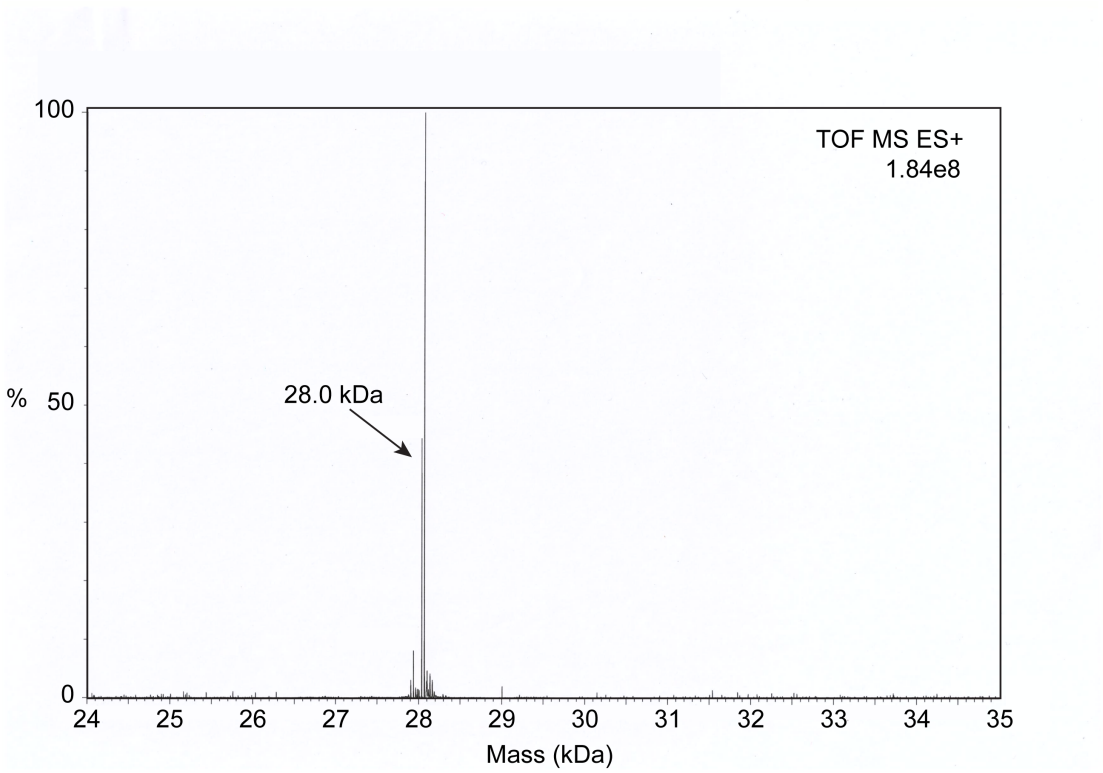

Figure C.2 – Mass spectrum of wild type EYFP. The measured molecular weight of the protein was 28.0 kDa.

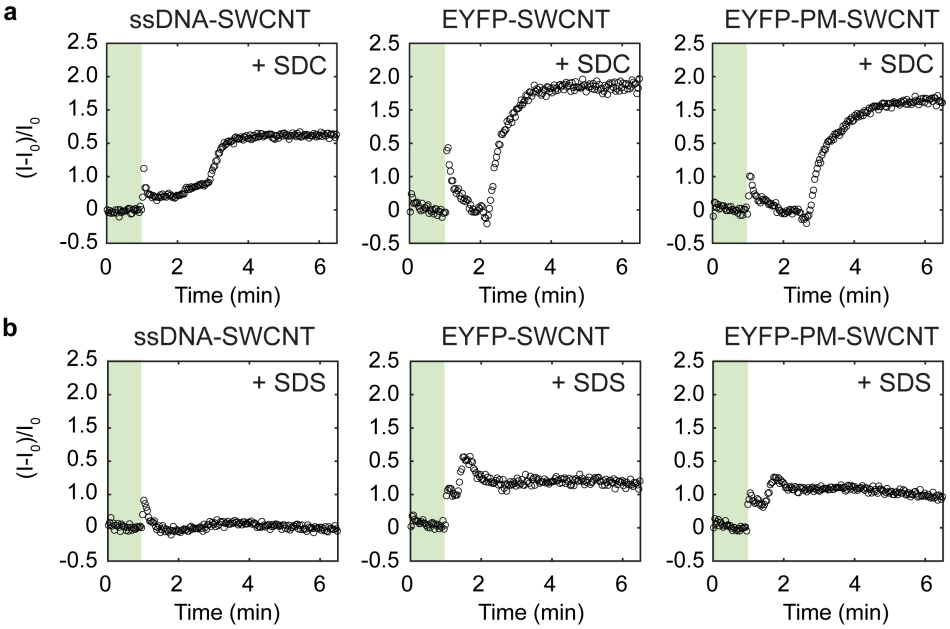

Figure C.3 – ssDNA, EYFP, and EYFP-PM displacement from the SWCNTs by SDC or SDS. Change of the (7,5) SWCNT peak fluorescence intensity in time after addition of SDC **(a)** or SDS **(b)**. The final concentration of the surfactants was 0.1%. The green regions indicate the intensity before the addition of the surfactants. A sharp increase of the intensity was observed when the surfactants were introduced to the SWCNT suspension through mixing by a pipette tip (after the green region). All solutions and suspensions were prepared in PBS. Excitation at 660±10 nm.

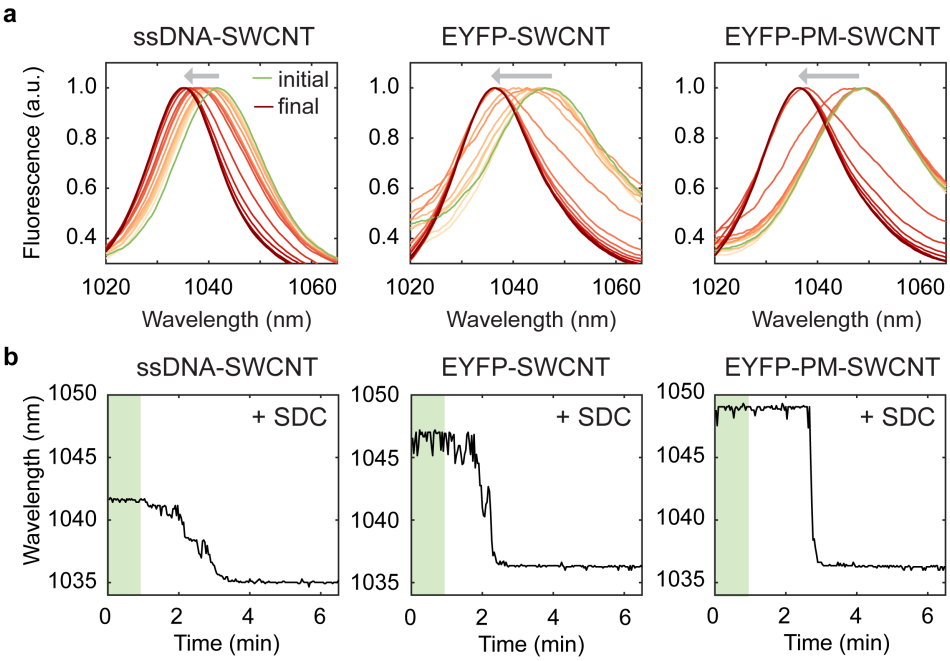

Figure C.4 – Fluorescence shifting of the (7,5) peak during SDC exchange with the SWCNT wrappings. **(a)** Time-lapse of fluorescence of ssDNA-SWCNTs, EYFP-SWCNTs, and EYFP-PM-SWCNTs spectra before (green line) and after (yellow to brown colour gradient) addition of SDC to the final concentration of 0.1 wt%. The traces are shown with 10 s time intervals. **(b)** Position of the peak maxima as a function of time. The green regions indicate times before addition of SDC. Excitation at 660±10 nm.

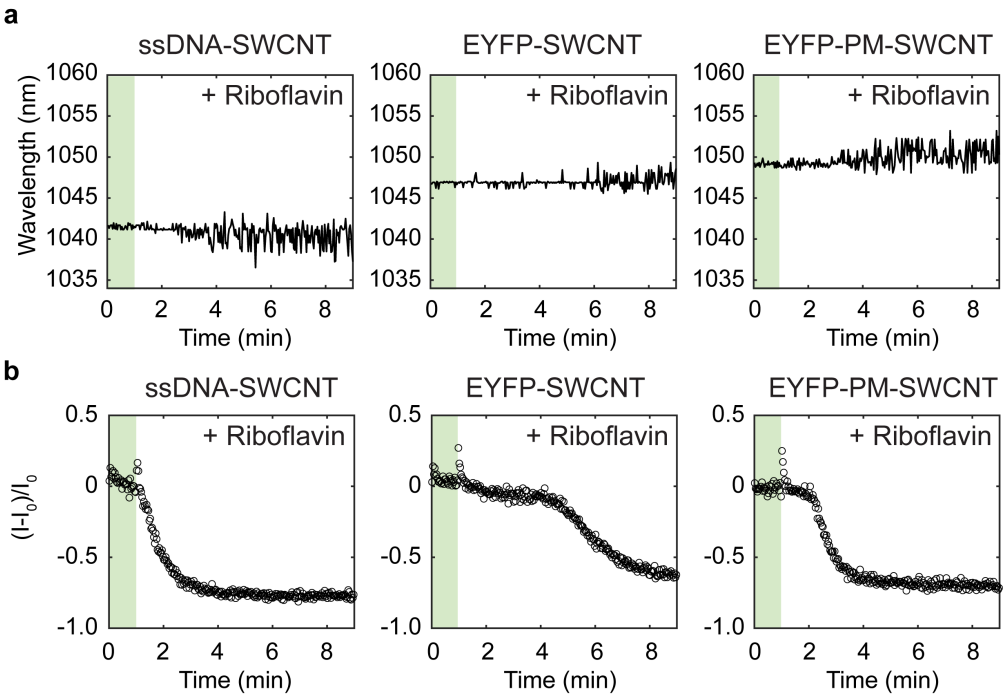

Figure C.5 – Fluorescence of the (7,5) SWCNT peak measured after addition of riboflavin. **(a)** Position of the peak maximum as a function of time after addition of riboflavin to ssDNA-SWCNTs, EYFP-SWCNTs, and EYFP-PM-SWCNTs. The green regions indicate time frames before the addition. **(b)** Intensity (I) was normalized to the intensity before the addition. All suspensions were prepared in PBS (pH 7.4). Excitation at 660±10 nm.

D GOx-PM-SWCNT sensors for continuous glucose monitoring

Table D.1 – *A. niger* wild type GOx genes from GenBank. The signaling sequence is indicated in bold

>gi|2357|emb|CAA34197.1| Glucose oxidase form *A. niger*
MQTLLVSSLVVSLAAALPHYIRSNGIEASLLTDPKDVSGRTVDYIIAGGGLTGLTTAARLTENP NISVLVIESGSYESDRGPIIEDLNAYGDIFGSSVDHAYETVELATNNQTALIRSGNGLGGSTLV NGGTWTRPHKAQVDSWETVFGNEGWNWDNVAAYSLQAERARAPNAKQIAAGHYFNASC HGVNGTVHAGPRDTGDDYSPIVKALMSAVEDRGVPTKKDFGCGDPHGVSMFPNTLHEDQ VRSDAAREWLLPNYQRPNLQVLTGQYVGKVLLSQNGTTPRAVGVEFGTHKGNTHNVYAKH EVLLAAGSAVSPTILEYSGIGMKSILEPLGIDTVVDLPVGLNLQDQTTATVRSRITSAGAGQGQ AAWFATFNETFGDYSEKAHELLNTKLEQWAEEAVARGGFHNTTALLIQYENYRDWIVNHNV AYSELFLDTAGVASFDVWDLLPFTRGYVHILDKDPYLHHFAYDPQYFLNELDLLGQAAATQL ARNISNSGAMQTYFAGETIPGDNLAYDADLSAWTEYIPYHFRPNYHGVGTCSMMPKEMGG VVDNAARVYGVQGLRVIDGSIPPTQMSSHVMTVFYAMALKISDAILEDYASMQ

Table D.2 – Synthetic double stranded DNA primers used for preparation of mutated GOx expression plasmids

Primer	**Primer sequence (5' to 3')**	**Size (bp)**
K13C-F	GGA CTG ACC CTT GTG ACG TCT CAG GTC	27
K13C-R	GAC CTG AGA CGT CAC AAG GGT CAG TCC	27
D70C-F	GAA TGC TTA TGG TTG TAT CTT CGG ATC TTC	30
D70C-R	GAA GAT CCG AAG ATA CAA CCA TAA GCA TTC	30
A418C-F	GAC CTG AGA CGT CAC AAG GGT CAG TCC	27
A418C-R	GTT CCT TGA CAC TTG TGG TGT CGC TTC	27
H446C-F	GGA CCC ATA CCT TTG TCA CTT CGC TTA CG	29
H446C-R	CGT AAG CGA AGT GAC AAA GGT ATG GGT CC	29

Table D.3 – Cell culture media for *E. coli* and *P. pastoris* culturing

Type (for 1 L)	Preparation protocol
LB growth medium:	10 g of tryptone (Sigma) 5 g of yeast extract (Becton Dickinson and Company) 10 g of NaCl (Sigma) pH adjusted to 7.0 and sterilized in an autoclave
LB medium and agar:	agar added to the LB medium at conc. 15 g L^{-1}
YPD growth medium:	10 g of yeast extract 20 g of peptone (Becton Dickinson and Company) 220 g L^{-1} dextrose (Sigma)
YPD medium and agar:	agar added to the LB medium at conc. 15 g L^{-1}
BMD 1% medium:	50 mL of 220 g L^{-1} dextrose (Sigma) 200 mL of 1M K_2PO_4 buffer at pH 6 100 ml of 134 g L^{-1} of yeast nitrogen base (Becton Dickinson and Company) 2 mL of 200 µg mL^{-1} Biotin (Fluka Chemia AG) Zeocin (InvivoGen-Eubio) added at concentration of 100 µg mL^{-1}
BMM2 (1% methanol):	10 mL of methanol (Carl Roth GmbH) 200 mL of 1M K_2PO_4 buffer at pH 6 100 mL of 134 g L^{-1} of yeast nitrogen base yeast nitrogen base 2 mL of 200 µg mL^{-1} Zeocin added at concentration of 100 µg mL^{-1}
BMM10 (5% methanol):	50 mL of methanol (Carl Roth GmbH) 200 mL of 1M K_2PO_4 buffer at pH 6 100 mL of 134 g L^{-1} of yeast nitrogen base yeast nitrogen base 2 mL of 200 µg mL^{-1} (filtered through a 0.2 µm filter) Zeocin added at concentration of 100 µg mL^{-1}

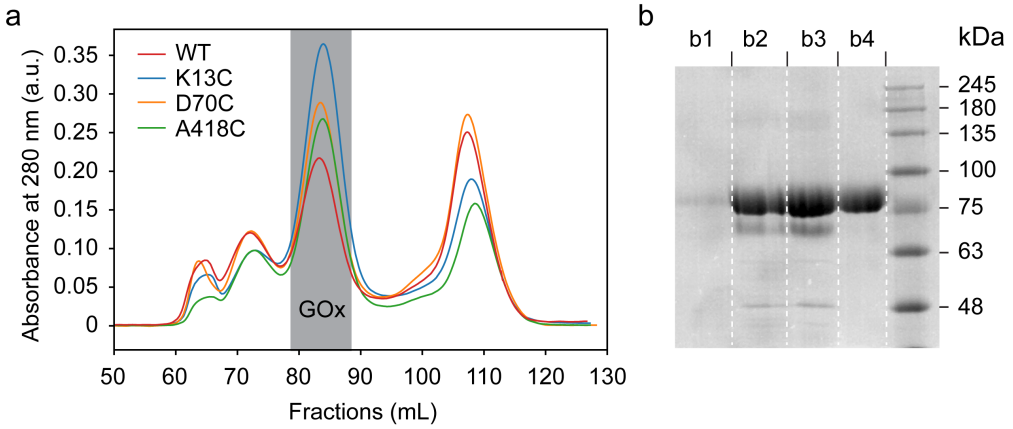

Figure D.1 – Purification of GOx variants. (a) Elution fractions which were obtained during purification of the GOx variants by size-exclusion chromatography. The absorbance of the eluted fractions was monitored at 280 nm. Presence of GOx in the eluted fractions was identified using the ABTS GOx activity assay (the peak of GOx is labeled on the graph). **(b)** SDS-PAGE analysis of the cell culture media obtained in GOx purification steps: (b1) GOx expression cell culture media; (b2) the media after its concentration; (b3) the media before and (b4) after size-exclusion chromatography purification. The gel was stained with the Coomassie Brilliant Blue dye (ITW Reagents). A protein marker IV was used as the reference (AppliChem).

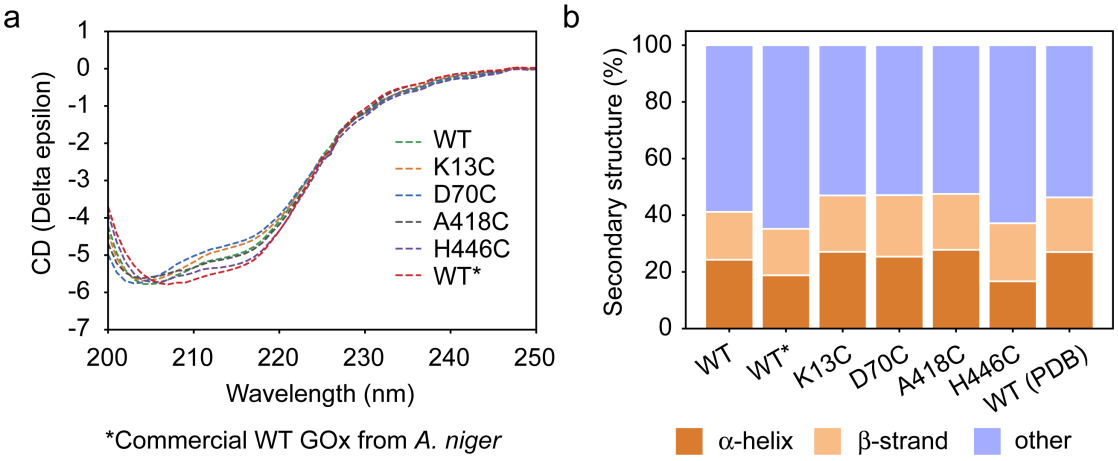

Figure D.2 – Secondary structure of GOx variants. (a) CD spectra of GOx variants fitted using a secondary structure prediction software BeStSel. **(b)** Distribution of BeStSel-predicted percentage of structure features (α-helices and β-strands) in the GOx variants. The variants were compared to the crystal structure from the PDB 1CF3 code. A star symbol indicates the sample which was prepared from the commercial GOx obtained from *A. niger*.

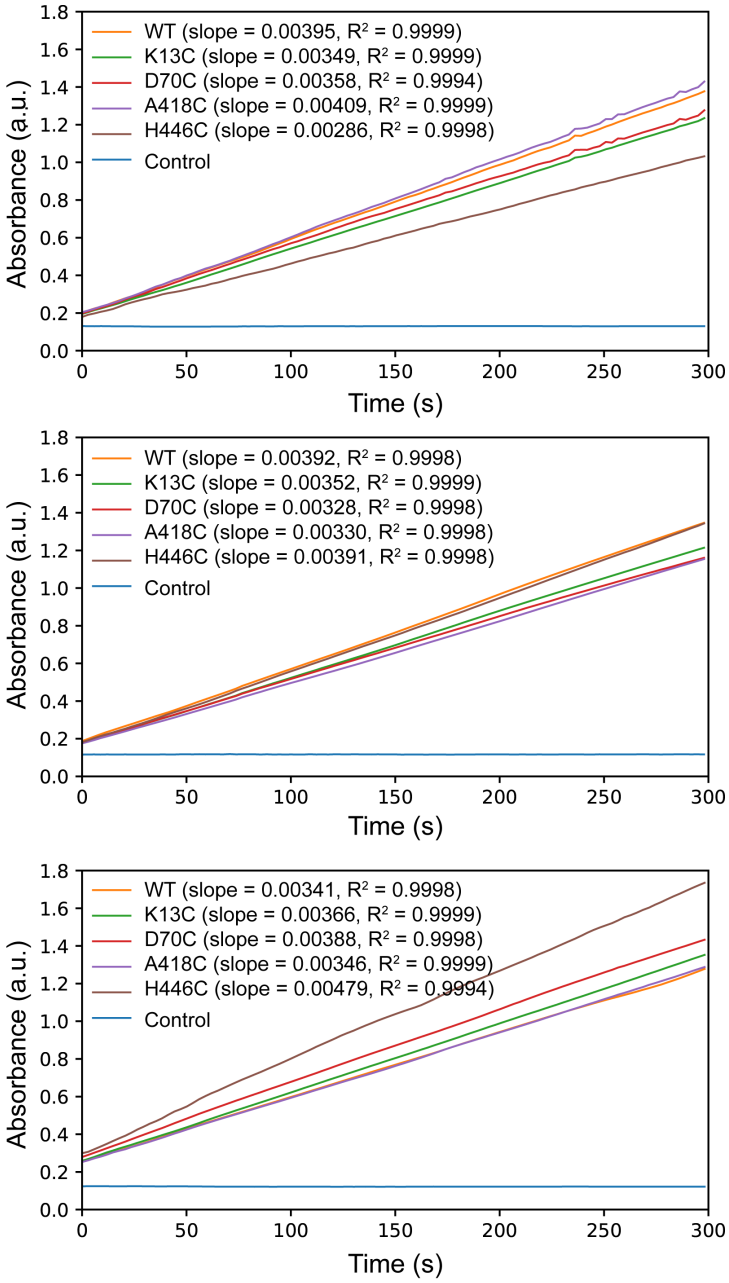

Figure D.3 – Absorbance measured at 414 nm during the ABTS colorimetric GOx activity assays. The data were fitted with linear functions. Obtained slope values are listed in the legends.

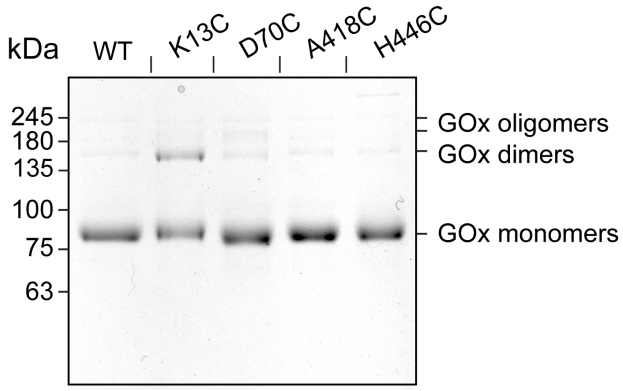

Figure D.4 – Non-reducing SDS-PAGE analysis. SDS-PAGE analysis reveals oligomerization of reduced GOx into dimers, trimers, and oligomers after storing the samples for two weeks in the EDTA-free buffer. The electrophoresis performed at 100 V for 10 min and 250 V for 30 min. The 7.5% gel was stained with the Coomassie Brilliant Blue dye (ITW Reagents).

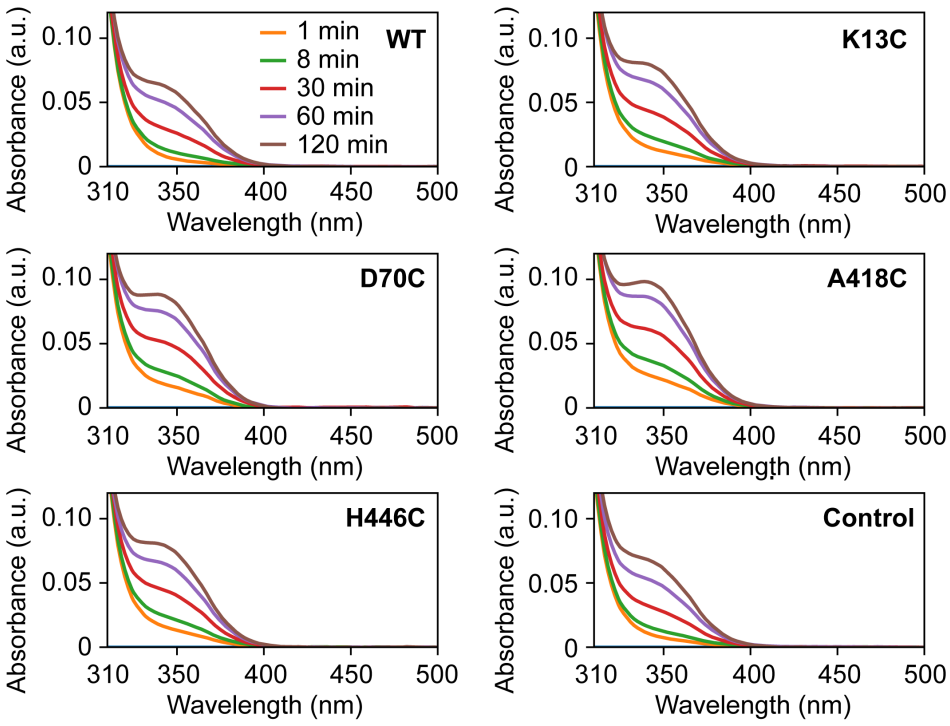

Figure D.5 – UV-Vis absorption spectra after addition of SPDP to the GOx solutions. The solutions were measured at 1, 8, 30, 60, and 120 min time points. Spontaneous degradation of SPDP was measured in PBS (control). The absorbance spectrum measured before the addition of SPDP was subtracted from each spectrum at the time points.

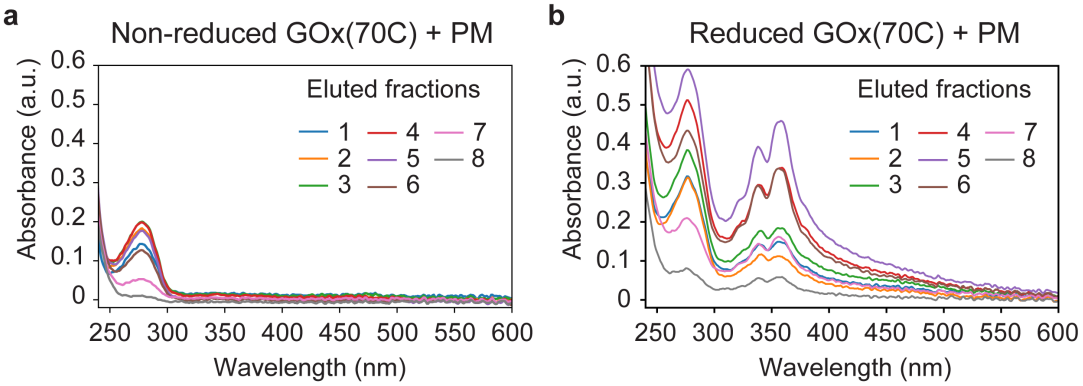

Figure D.6 – Measured absorbance spectra of the fractions collected from the desalting column. The fractions of 150 µL collected from the desalting column (PD midiTrap G-25, GE Healthcare) after overnight reaction with the PM crosslinker with the non-reduced **(a)** and reduced **(b)** GOx(70C) variant.

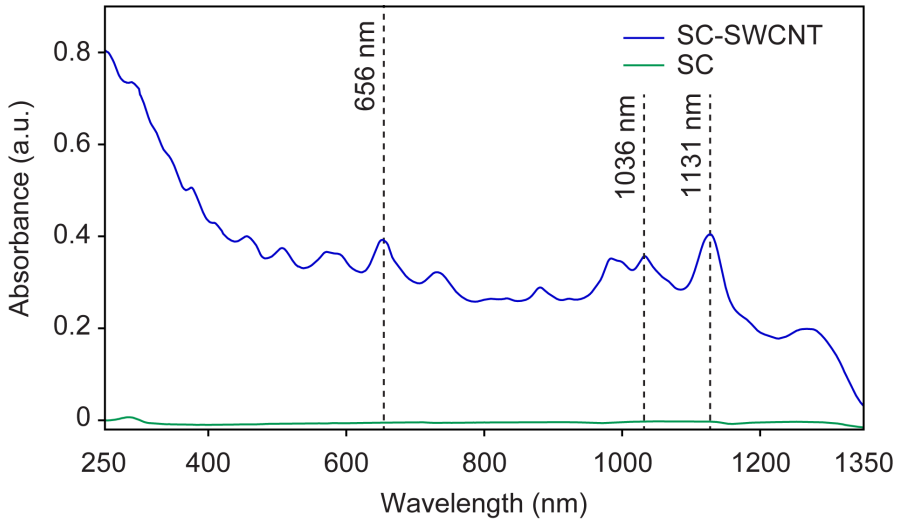

Figure D.7 – Absorbance spectra of SC-SWCNTs (with 1% SC) and 1% SC.

Bibliography

1. Iijima, S. Helical microtubules of graphitic carbon. *Nature* **354,** 56–58 (1991).
2. Jariwala, D., Sangwan, V. K., Lauhon, L. J., Marks, T. J. & Hersam, M. C. Carbon nanomaterials for electronics, optoelectronics, photovoltaics, and sensing. *Chemical Society Reviews* **42,** 2824–2860 (2013).
3. Zhang, Q., Huang, J. Q., Qian, W. Z., Zhang, Y. Y. & Wei, F. The road for nanomaterials industry: a review of carbon nanotube production, post-treatment, and bulk applications for composites and energy storage. *Small* **9,** 1237–1265 (2013).
4. Nish, A., Hwang, J.-Y., Doig, J. & Nicholas, R. J. Highly selective dispersion of single-walled carbon nanotubes using aromatic polymers. *Nature Nanotechnology* **2,** 640–646 (2007).
5. Wang, Z. H. & Jin, G. Covalent immobilization of proteins for the biosensor based on imaging ellipsometry. *Journal of Immunological Methods* **285,** 237–243 (2004).
6. Polo, E. & Kruss, S. Impact of redox-active molecules on the fluorescence of polymer-wrapped carbon nanotubes. *The Journal of Physical Chemistry C* **120,** 3061–3070 (2016).
7. Lee, A. J. *et al.* Bright fluorescence from individual single-walled carbon nanotubes. *Nano Letters* **11,** 1636–1640 (2011).
8. Gillen, A. J., Kupis-Rozmysł Owicz, J., Gigli, C., Schuergers, N. & Boghossian, A. A. Xeno nucleic acid nanosensors for enhanced stability against ion-induced perturbations. *Journal of Physical Chemistry Letters* **9,** 4336–4343 (2018).
9. Salem, D. P. *et al.* Ionic strength-mediated phase transitions of surface-adsorbed DNA on single-walled carbon nanotubes. *Journal of the American Chemical Society* **139,** 16791–16802 (2017).
10. Pramanik, C., Gissinger, J. R., Kumar, S. & Heinz, H. Carbon nanotube dispersion in solvents and polymer solutions: mechanisms, assembly, and preferences. *ACS Nano* **11,** 12805–12816 (2017).
11. Cedervall, T. *et al.* Understanding the nanoparticle-protein corona using methods to quantify exchange rates and affinities of proteins for nanoparticles. *Proceedings of the National Academy of Sciences* **104,** 2050–2055 (2007).

12. Yum, K. & McNicholas, T. Single-walled carbon nanotube-based near-infrared optical glucose sensors toward in vivo continuous glucose monitoring. *Journal of Diabetes Science and Technology* **7,** 72–87 (2013).

13. Barone, P. W., Baik, S., Heller, D. A. & Strano, M. S. Near-infrared optical sensors based on single-walled carbon nanotubes. *Nature Materials* **4,** 86–92 (2004).

14. Bati, A., Yu, L., Batmunkh, M. & Shapter, J. G. Synthesis, purification, properties and characterization of sorted single-walled carbon nanotubes. *Nanoscale* **10,** 22087–22139 (2018).

15. Crochet, J., Clemens, M. & Hertel, T. Quantum yield heterogeneities of aqueous single-wall carbon nanotube suspensions. *Journal of the American Chemical Society* **129,** 8058–8059 (2007).

16. Connell, M. J. O. *et al.* Band gap fluorescence from individual single-walled carbon nanotubes. *Science* **297,** 593–597 (2002).

17. Eckstein, K. H., Hartleb, H., Achsnich, M. M., Schöppler, F. & Hertel, T. Localized charges control exciton energetics and energy dissipation in doped carbon nanotubes. *ACS Nano* **11,** 10401–10408 (2017).

18. Antonucci, A., Kupis-Rozmyslowicz, J. & Boghossian, A. A. Noncovalent protein and peptide functionalization of single-walled carbon nanotubes for biodelivery and optical sensing applications. *ACS Applied Materials and Interfaces* **9,** 11321–11331 (2017).

19. Zubkovs, V., Schuergers, N., Lambert, B., Ahunbay, E. & Boghossian, A. A. Mediatorless, reversible optical nanosensor enabled through enzymatic pocket doping. *Small* **1701654,** 1–10 (2017).

20. Oliveira, S. F. *et al.* Protein functionalized carbon nanomaterials for biomedical applications. *Carbon* **95,** 767–779 (2015).

21. Zhou, Y., Fang, Y. & Ramasamy, R. P. Non-covalent functionalization of carbon nanotubes for electrochemical biosensor development. *Sensors* **19,** 1–29 (2019).

22. Pino, P. D. *et al.* Protein corona formation around nanoparticles - from the past to the future. *Materials Horizons* **1,** 301–313 (2014).

23. Bisker, G. *et al.* Protein-targeted corona phase molecular recognition. *Nature Communications* **7,** 1–14 (2016).

24. He, Z. & Zhou, J. Probing carbon nanotube-amino acid interactions in aqueous solution with molecular dynamics simulations. *Carbon* **78,** 500–509 (2014).

25. Okazaki, T. *et al.* Selectivity of water-soluble proteins in single-walled carbon nanotube dispersions. *Chemical Physics Letters* **429,** 497–502 (2006).

26. Saifuddin, N., Raziah, A. Z. & Junizah, A. R. Carbon nanotubes: a review on structure and their interaction with proteins. *Journal of Chemistry* **676815,** 1–18 (2013).

27. Yang, W., Thordarson, P., Gooding, J. J., Ringer, S. P. & Braet, F. Carbon nanotubes for biological and biomedical applications. *Nanotechnology* **18,** 1–12 (2007).

28. Liu, Z. *et al.* Drug delivery with carbon nanotubes for in vivo cancer treatment. *Cancer Research* **68,** 6652–6660 (2008).

29. Bisker, G. *et al.* A mathematical formulation and solution of the CoPhMoRe inverse problem for helically wrapping polymer corona phases on cylindrical substrates. *The Journal of Physical Chemistry C* **109,** 13876–13886 (2015).

30. Li, M. *et al.* Efficient and facile fabrication of glucose biosensor based on electrochemically etched porous HOPG platform. *Electroanalysis* **29,** 944–949 (2017).

31. Liu, J. *et al.* Graphene bridged enzyme electrodes for glucose biosensing application. *Analyst* **138,** 2567–2575 (2013).

32. Piao, Y., Han, D. J. & Seo, T. S. Highly conductive graphite nanoparticle based enzyme biosensor for electrochemical glucose detection. *Sensors and Actuators* **194,** 454–459 (2014).

33. Choi, Y. *et al.* Single-molecule lysozyme dynamics monitored by an electron circuit. *Science* **335,** 319–324 (2012).

34. Holzinger, M., Baur, J., Haddad, R., Wang, X. & Cosnier, S. Multiple functionalization of single-walled carbon nanotubes by dip coating. *Chemical Communications* **47,** 2450–2452 (2011).

35. Karachevtsev, V. a. *et al.* Noncovalent interaction of single-walled carbon nanotubes with 1-pyrenebutanoic acid succinimide ester and glucoseoxidase. *Journal of Physical Chemistry C* **115,** 21072–21082 (2011).

36. Hong, G., Antaris, A. L. & Dai, H. Near-infrared fluorophores for biomedical imaging. *Nature Biomedical Engineering* **1,** 1–22 (2017).

37. Martinic, I., Eliseeva, S. V. & Petoud, S. Near-infrared emitting probes for biological imaging: organic fluorophores, quantum dots, fluorescent proteins, lanthanide(III) complexes and nanomaterials. *Journal of Luminescence* **189,** 19–43 (2017).

38. Yudasaka, M. *et al.* Near-infrared photoluminescent carbon nanotubes for imaging of brown fat. *Scientific Reports* **7,** 1–12 (2017).

39. Hong, G. *et al.* Through-skull fluorescence imaging of the brain in a new near-infrared window. *Nature Photonics* **8,** 723–730 (2014).

40. Hong, L., Mouri, S., Miyauchi, Y., Matsuda, K. & Nakashima, N. Redox properties of a single (7,5) single-walled carbon nanotube determined by an in situ photoluminescence spectroelectrochemical method. *Nanoscale* **6,** 12798–12804 (2014).

41. Harvey, J. D. *et al.* A carbon nanotube reporter of microRNA hybridization events in vivo. *Nature Biomedical Engineering* **1,** 1–11 (2017).

42. Barone, P. W., Parker, R. S. & Strano, M. S. In vivo fluorescence detection of glucose using a single-walled carbon nanotube optical sensor: design, fluorophore properties, advantages, and disadvantages. *Analytical Chemistry* **77,** 7556–7562 (2005).

43. Lee, M. A. *et al.* Implanted nanosensors in marine organisms for physiological biologging: design, feasibility, and species variability. *ACS Sensors* **4,** 32–43 (2019).

44. Vogel, A. & Venugopalan, V. Mechanisms of pulsed laser ablation of biological tissues. *Chemical Reviews* **103,** 577–644 (2003).

45. Bisker, G., Iverson, N. M., Ahn, J. & Strano, M. S. A pharmacokinetic model of a tissue implantable insulin sensor. *Advanced Healthcare Materials* **4,** 87–97 (2015).

46. Rosenthal, N. R. & Barrett, E. J. Hyperglycemic nonketotic diabetic patients. *Endocrinology And Metabolism* **60,** 607–610 (1985).

47. Vashist, S. Continuous glucose monitoring systems: a review. *Diagnostics* **3,** 385–412 (2013).

48. Karuranga, S., Fernandes, J. R., Huang, Y. & Malanda, B. *International Diabetes Federation diabetes atlas* 8th Edition, 1–150 (www.diabetesatlas.org, 2017).

49. Zhu, Z. *et al.* A critical review of glucose biosensors based on carbon nanomaterials: carbon nanotubes and graphene. *Sensors* **12,** 5996–6022 (2012).

50. Kim, J., Campbell, A. S. & Wang, J. Wearable non-invasive epidermal glucose sensors: a review. *Talanta* **177,** 163–170 (2018).

51. Chen, C. *et al.* Current and emerging technology for continuous glucose monitoring. *Sensors* **17,** 1–19 (2017).

52. Kropff, J. *et al.* Accuracy and longevity of an implantable continuous glucose sensor in the PRECISE study: a 180-day, prospective, multicenter, pivotal trial. *Diabetes Care* **40,** 63–68 (2017).

53. Lundsgaard-Nielsen, S. M. *et al.* Critical-depth Raman spectroscopy enables home-use non-invasive glucose monitoring. *PLoS ONE* **13,** 1–11 (2018).

54. Mortellaro, M. & DeHennis, A. Performance characterization of an abiotic and fluor.-based continuous glucose monitoring system in patients with type 1 diabetes. *Biosensors and Bioelectronics* **61,** 227–231 (2014).

55. Yoon, H. *et al.* Periplasmic binding proteins as optical modulators of single-walled carbon nanotube fluorescence: amplifying a nanoscale actuator. *Angewandte Chemie - International Edition* **50,** 1828–1831 (2011).

56. Muguruma, H., Yoshida, S., Urata, M., Fujisawa, K. & Matsui, Y. An amperometric biosensor for glucose based on a composite electrode of glucose dehydrogenase, carbon nanotubes, and plasma-polymerized thin films. *Electrochemistry* **76,** 545–548 (2008).

57. Ferri, S., Kojima, K. & Sode, K. Review of glucose oxidases and glucose dehydrogenases: a bird's eye view of glucose sensing enzymes. *Journal of Diabetes Science and Technology* **5,** 1068–1076 (2011).

58. Karachevtsev, V. A. Glucose sensing based on NIR fluorescence of DNA-wrapped single-walled carbon nanotubes. *Chemical Physics Letters* **435,** 104–108 (2007).

59. Zubkovs, V. *et al.* Spinning-disc confocal microscopy in the second near-infrared window (NIR-II). *Scientific Reports* **8,** 1–10 (2018).

60. Antaris, A. L. *et al.* A small-molecule dye for NIR-II imaging. *Nature Materials* **15,** 235–242 (2015).

61. Hong, G. *et al.* Ultrafast fluorescence imaging in vivo with conjugated polymer fluorophores in the second near-infrared window. *Nature Communications* **5,** 1–43 (2014).

62. Hong, G. *et al.* Through-skull fluorescence imaging of the brain in a new near-infrared window. *Nature Photonics* **8,** 723–730 (2014).

63. Filonov, G. S. *et al.* Bright and stable near-infrared fluorescent protein for in vivo imaging. *Nature Biotechnology* **29,** 757–761 (2011).

64. Rodriguez, E. A. *et al.* The growing and glowing toolbox of fluorescent and photoactive proteins. *Trends in Biochemical Sciences* **42,** 111–129 (2017).

65. Curcio, J. A. & Petty, C. C. The near infrared absorption spectrum of liquid water. *Journal of the Optical Society of America* **41,** 302–303 (1951).

66. Li, C. *et al.* In vivo real-time visualization of tissue blood flow and angiogenesis using Ag2S quantum dots in the NIR-II window. *Biomaterials* **35,** 393–400 (2014).

67. Smith, A. M., Mancini, M. C. & Nie, S. Second window for in vivo imaging. *Nature Nanotechnology* **4,** 710–711 (2009).

68. Chen, G. *et al.* In vivo real-time visualization of mesenchymal stem cells tropism for cutaneous regeneration using NIR-II fluorescence imaging. *Biomaterials* **53,** 265–273 (2015).

69. Li, Q. *et al.* Graphene/graphene-tube nanocomposites templated from cage-containing metal-organic frameworks for oxygen reduction in Li-O2 batteries. *Advanced Materials* **26,** 1378–1386 (2014).

70. Wozniak, B. & Dera, J. Light absorption in sea water. *Atmospheric and Oceanographic Science Library* **33,** 11–81 (2007).

71. Tao, Z. *et al.* Near-infrared-II fluorescent agents, methods of making near-infrared-II fluorescent agents, and methods of using water-soluble NIR-II fluorescent agents. *Patent* **US20150056142,** 1–37 (2015).

72. Hong, G., Diao, S., Antaris, A. L. & Dai, H. Carbon nanomaterials for biological imaging and nanomedicinal therapy. *Chemical Reviews* **115,** 10816–10906 (2015).

73. Weisman, R. B. & Bachilo, S. M. Dependence of optical transition energies on structure for single-walled carbon nanptubes in aqueous suspension: an empirical Kataura plot. *Nano Letters* **3,** 1235–1238 (2003).

74. Antaris, A. L. *et al.* A high quantum yield molecule-protein complex fluorophore for near-infrared II imaging. *Nature Communications* **8,** 1–11 (2017).

75. Sun, Y. *et al.* Novel bright-emission small-molecule NIR-II fluorophores for in vivo tumor imaging and image-guided surgery. *Chemical Science* **8,** 3489–3493 (2017).

76. Sun, Y. *et al.* Novel benzo-bis(1,2,5-thiadiazole) fluorophores for in vivo NIR-II imaging of cancer. *Chemical Science* **7,** 6203–6207 (2016).

77. Shou, K. *et al.* Multifunctional biomedical imaging in physiological and pathological conditions using a NIR-II probe. *Advanced Functional Materials* **27,** 1–12 (2017).

78. Hatami, S. *et al.* Absolute photoluminescence quantum yields of IR26 and IR-emissive Cd1-xHg xTe and PbS quantum dots - method- and material-inherent challenges. *Nanoscale* **7,** 133–143 (2015).

79. Kumar, M. *et al.* Hot exciton cooling and multiple exciton generation in PbSe quantum dots. *Physical Chemistry Chemical Physics* **18,** 31107–31114 (2016).

80. Murray, C. B. *et al.* Colloidal synthesis of nanocrystals and nanocrystal superlattices. *IBM Journal of Research and Development* **45,** 47–56 (2001).

81. Chiappino-Pepe, A. *et al.* Towards engineering SMaRT nanosensors: elucidating the effects of polymer wrapping on exciton dynamics in single-walled carbon nanotubes. *Submitted to ACS Nano,* 1–30.

82. Godin, A. G. *et al.* Single-nanotube tracking reveals the nanoscale organization of the extracellular space in the live brain. *Nature Nanotechnology* **12,** 238–243 (2017).

83. Roxbury, D., Jena, P. V., Shamay, Y., Horoszko, C. P. & Heller, D. A. Cell membrane proteins modulate the carbon nanotube optical bandgap via surface charge accumulation. *ACS Nano* **10,** 499–506 (2016).

84. Roxbury, D. *et al.* Hyperspectral microscopy of near-Infrared fluorescence enables 17-chirality carbon nanotube imaging. *Scientific Reports* **5,** 1–6 (2015).

85. Sun, C., Wang, Y., Zhang, H. & Qian, J. Near-infrared laser scanning confocal microscopy and its application in bioimaging. *Optical and Quantum Electronics* **50,** 1–9 (2018).

86. Jonkman, J. & Brown, C. M. Any way you slice it - a comparison of confocal microscopy techniques. *Journal of Biomolecular Techniques* **26,** 54–65 (2015).

87. Theer, P., Mongis, C. & Knop, M. PSFj: Know your fluorescence microscope. *Nature Methods* **11,** 981–982 (2014).

88. Sbalzarini, I. F. & Koumoutsakos, P. Feature point tracking and trajectory analysis for video imaging in cell biology. *Journal of Structural Biology* **151,** 182–195 (2005).

89. Boghossian, A. A. *et al.* Application of nanoparticle antioxidants to enable hyperstable chloroplasts for solar energy harvesting. *Advanced Energy Materials* **3,** 881–893 (2013).

90. Zhang, J. *et al.* Single molecule detection of nitric oxide enabled by d(AT)15 DNA adsorbed to near infrared fluorescent single-walled carbon nanotubes. *Journal of the American Chemical Society* **133,** 567–581 (2011).

91. Zheng, M. *et al.* DNA-assisted dispersion and separation of carbon nanotubes. *Nature Materials* **2,** 338–342 (2003).

92. Abbe, E. Beiträge zur theorie des mikroskops und der mikroskopischen wahrnehmung. *Archiv für Mikroskopische Anatomie* **9,** 413–418 (1873).

93. Wilson, T. Resolution and optical sectioning in the confocal microscope. *Journal of Microscopy* **244,** 113–121 (2011).

94. Pawley, J. B. *Handbook of biological confocal microscopy* (2006).

95. Kubitscheck, U. *Fluorescence microscopy: from principles to biological applications* (2013).

96. Kozubek, M. Theoretical versus experimental resolution in optical microscopy. *Microscopy Research and Technique* **53,** 157–166 (2001).

97. Sandison, D. R., Piston, D. W., Williams, R. M. & Webb, W. W. Quantitative comparison of background rejection, signal-to-noise ratio, and resolution in confocal and full-field laser scanning microscopes. *Applied Optics* **34,** 3576–3588 (1995).

98. Fouquet, C. *et al.* Improving axial resolution in confocal microscopy with new high refractive index mounting media. *PLoS ONE* **10,** 1–17 (2015).

99. Swoger, J., Huisken, J. & Stelzer, E. H. K. Multiple imaging axis microscopy improves resolution for thick-sample applications. *Optics Letters* **28,** 1654–1656 (2003).

100. Heintzmann, R. & Ficz, G. Breaking the resolution limit in light microscopy. *Methods in Cell Biology* **114,** 525–544 (2013).

101. Godin, A., Lounis, B. & Cognet, L. Super-resolution microscopy approaches for live cell imaging. *Biophysical Journal* **107,** 1777–1784 (2014).

102. Anderson, N., Prabhat, P. & Erdogan, T. *Spectral modeling in fluorescence microscopy* (2008).

103. Boghossian, A. A., Choi, J. H., Ham, M. H. & Strano, M. S. Dynamic and reversible self-assembly of photoelectrochemical complexes based on lipid bilayer disks, photosynthetic reaction centers, and single-walled carbon nanotubes. *Langmuir* **27,** 1599–1609 (2011).

104. Edward, J. T. Molecular volumes and the Stokes-Einstein equation. *Journal of Chemical Education* **47,** 261–270 (1970).

105. Renn, J. Einstein's invention of Brownian motion. *Annalen der Physik* **14,** 23–37 (2005).

106. Giraldo, J. P. *et al.* Plant nanobionics approach to augment photosynthesis and biochemical sensing. *Nature Materials* **13,** 400–408 (2014).

107. Wong, M. H. *et al.* Lipid exchange envelope penetration (LEEP) of nanoparticles for plant engineering: a universal localization mechanism. *Nano Letters* **16,** 1161–1172 (2016).

108. Galassi, T. V., Jena, P. V., Roxbury, D. & Heller, D. A. Single nanotube spectral imaging to determine molar concentrations of isolated carbon nanotube species. *Analytical Chemistry* **89,** 1073–1077 (2017).

109. Amsden, B. Solute diffusion within hydrogels. Mechanisms and models. *Macromolecules* **31,** 8382–8395 (1998).

110. Narayanan, J., Xiong, J. Y. & Liu, X. Y. Determination of agarose gel pore size: absorbance measurements vis a vis other techniques. *Journal of Physics: Conference Series* **28,** 83–86 (2006).

111. Weng, L., Liang, S., Zhang, L., Zhang, X. & Xu, J. Transport of glucose and poly(ethylene glycol)s in agarose gels studied by the refractive index method. *Macromolecules* **38,** 5236–5242 (2005).

112. Azuma, T. & Kei, T. Super-resolution spinning-disk confocal microscopy using optical photon reassignment. *Optics Express* **23,** 15003–15011 (2015).

113. Ward, E. N. & Pal, R. Image scanning microscopy: an overview. *Journal of Microscopy* **266,** 221–228 (2017).

114. Wang, C., Ye, Y., Hochu, G. M., Sadeghifar, H. & Gu, Z. Enhanced cancer immunotherapy by microneedle patch-assisted delivery of anti-PD1 antibody. *Nano Letters* **16,** 2334–2340 (2016).

115. Gu, Z. *et al.* Injectable nano-network for glucose-mediated insulin delivery. *ACS Nano* **7,** 4194–4201 (2013).

116. Wang, C. *et al.* Red blood cells for glucose-responsive insulin delivery. *Advanced Materials* **29,** 1–7 (2017).

117. Yu, J. *et al.* Microneedle-array patches loaded with hypoxia-sensitive vesicles provide fast glucose-responsive insulin delivery. *Proceedings of the National Academy of Sciences of the United States of America* **112,** 8260–8265 (2015).

118. Russell, S. J. *et al.* Outpatient glycemic control with a bionic pancreas in type 1 diabetes. *The New England Journal of Medicine* **371,** 313–325 (2014).

119. Kovatchev, B. P. *et al.* Safety of outpatient closed-loop control: first randomized crossover trials of a wearable artificial pancreas. *Diabetes Care* **37,** 1789–1796 (2014).

120. Thabit, H. *et al.* Home use of an artificial beta cell in type 1 diabetes. *New England Journal of Medicine* **373,** 2129–2140 (2015).

121. Phillip, M. *et al.* Nocturnal glucose control with an artificial pancreas at a diabetes camp. *The New England Journal of Medicine* **368,** 824–833 (2013).

122. Veiseh, O., Tang, B. C., Whitehead, K. A., Anderson, D. G. & Langer, R. Managing diabetes with nanomedicine: challenges and opportunities. *Nature Reviews Drug Discovery* **14,** 45–57 (2014).

123. Barone, P. W. & Strano, M. S. Reversible control of carbon nanotube aggregation for a glucose affinity sensor. *Angewandte Chemie - International Edition* **45,** 8138–8141 (2006).

124. Jin, H. *et al.* Detection of single-molecule H2O2 signalling from epidermal growth factor receptor using fluorescent single-walled carbon nanotubes. *Nature Nanotechnology* **5,** 302–309 (2010).

125. Giraldo, J. P. *et al.* A ratiometric sensor using single chirality near-infrared fluorescent carbon nanotubes: application to in vivo monitoring. *Small* **11,** 3973–3984 (2015).

126. Stein, E. W., Grant, P. S., Zhu, H. & McShane, M. J. Microscale enzymatic optical biosensors using mass transport limiting nanofilms. Fabrication and characterization using glucose as a model analyte. *Analytical Chemistry* **79,** 1339–1348 (2007).

127. Yang, J., Zhang, Z., Zhang, D. & Li, Y. Quantitative analysis of the (n,m) abundance of single-walled carbon nanotubes dispersed in ionic liquids by optical absorption spectra. *Materials Chemistry and Physics* **139,** 233–240 (2013).

128. Keston, A. S. Specific colorimetric enzymatic analytical reagents for glucose. *129th Meeting of the American Chemical Society* **31,** 69 (1956).

129. Gouda, M. D., Singh, S. A., Rao, A. G. A., Thakur, M. S. & Karanth, N. G. Thermal inactivation of glucose oxidase: mechanism and stabilization using additives. *Journal of Biological Chemistry* **278,** 24324–24333 (2003).

130. Li, W. *et al.* Fully-drawn origami paper analytical device for electrochemical detection of glucose. *Sensors and Actuators B: Chemical* **231,** 230–238 (2016).

131. Barone, P. W. & Strano, M. S. Single walled carbon nanotubes as reporters for the optical detection of glucose. *Journal of Diabetes Science and Technology* **3,** 242–252 (2009).

132. Chey, C. O., Ibupoto, Z. H., Khun, K., Nur, O. & Willander, M. Indirect determination of mercury ion by inhibition of a glucose biosensor based on ZnO nanorods. *Sensors* **12,** 15063–15077 (2012).

133. Azamian, B. R., Davis, J. J., Coleman, K. S., Bagshaw, C. B. & Green, M. L. H. Bioelectrochemical single-walled carbon nanotubes. *Journal of the American Chemical Society* **124,** 12664–12665 (2002).

134. Keilin, D. & Hartree, E. F. Specificity of glucose oxidase. *The Biochemical Journal* **50,** 331–341 (1952).

135. Vuong, T. V., Foumani, M., MacCormick, B., Kwan, R. & Master, E. R. Direct comparison of gluco-oligosaccharide oxidase variants and glucose oxidase: substrate range and H2O2 stability. *Scientific Reports* **6,** 1–9 (2016).

136. Bartlett, P. N., Bradford, V. Q. & Whitaker, R. G. Enzyme electrode studies of glucose oxidase modified with a redox mediator. *Talanta* **38,** 57–63 (1991).

137. Gibson, Q., Swoboda, B. & Massey, V. Kinetics and mechanism of action of glucose oxidase. *Journal of Biological Chemistry* **239,** 3927–3934 (1964).

138. Mislovicova, D., Patoprsty, V. & Vikartovska, A. Enzymatic oxidation and separation of various saccharides with immobilized glucose oxidase. *Applied Biochemistry and Biotechnology* **162,** 1669–1677 (2010).

139. Hundeck, H. G. *et al.* Four-channel enzyme thermistor system for process monitoring and control in biotechnology. *Analytica Chimica Acta* **238,** 211–221 (1990).

140. Watanabe, E., Takagi, M., Takei, S., Hoshi, M. & Shu-Gui, C. Development of biosensors for the simultaneous determination of sucrose and glucose, lactose and glucose, and starch and glucose. *Biotechnology and Bioengineering* **38,** 99–103 (1991).

141. Schugerl, K. *et al.* Fermentation monitoring and control by on-line flow injection and liquid chromatography. *Analytica Chimica Acta* **249,** 87–100 (1991).

142. Harding, V. J., Nicholson, T. F. & Armstrong, A. R. Cutaneous blood-sugar curves after the administration of fructose, mannose and xylose. *The Biochemical Journal* **27,** 2035–2042 (1933).

143. Blanco, J. G. Sugar metabolism. Lactose, galactose and xylose. *Journal of Biological Chemistry* **79,** 667–672 (1928).

144. Bornhoeft, L. R., Biswas, A. & McShane, M. J. Composite hydrogels with engineered microdomains for optical glucose sensing at low oxygen conditions. *Biosensors* **7,** 1–12 (2017).

145. Roberts, J. R. Novel in situ-gelling, alginate-based composites for injectable delivery: tuning mechanical and functional characteristics. *Degree Thesis, Texas A&M University* (2014).

146. Farrell, P. C. & Babb, A. L. Estimation of the permeability of cellulosic membranes from solute dimensions and diffusivities. *Journal of Biomedical Materials Research* **7,** 275–300 (1973).

147. Wooten, M., Karra, S., Zhang, M. & Gorski, W. On the direct electron transfer, sensing, and enzyme activity in the glucose oxidase/carbon nanotubes system. *Analytical Chemistry* **86,** 752–757 (2014).

148. Ostafe, R., Prodanovic, R., Nazor, J. & Fischer, R. Ultra-high-throughput screening method for the directed evolution of glucose oxidase. *Chemistry and Biology* **21,** 414–421 (2014).

149. Swoboda, B. E. P. & Massey, V. Purification and properties of the glucose oxidase from Aspergillus niger. *Journal of Biological Chemistry* **240,** 2209–2215 (1965).

150. Nakamura, S., Hayashi, S. & Koga, K. Effect of periodate oxidation on the structure and properties of glucose oxidase. *Biochimica et Biophysica Acta* **445,** 294–308 (1976).

151. Shan, D., Wang, S., He, Y. & Xue, H. Amperometric glucose biosensor based on in situ electropolymerized polyaniline/poly(acrylonitrile-co-acrylic acid) composite film. *Materials Science and Engineering C* **28,** 213–217 (2008).

152. Xue, H., Shen, Z. & Li, Y. Polyaniline - polyisoprene composite film based glucose biosensor with high permselectivity. *Synthetic Metals* **124,** 345–349 (2001).

153. Zhou, H. *et al.* Glucose biosensor based on platinum microparticles dispersed in nanofibrous polyaniline. *Biosensors and Bioelectronics* **20,** 1305–1311 (2005).

154. Tu, X., Pehrsson, P. & Zhao, W. Redox reaction of DNA-encased HiPco carbon nanotubes with hydrogen peroxide: a near infrared optical sensitivity and kinetics study. *Journal of Physical Chemistry C* **111,** 17227–17231 (2007).

155. Jin, H., Heller, D. A., Kim, J. H. & Strano, M. S. Stochastic analysis of stepwise fluorescence quenching reactions on single-walled carbon nanotubes: single molecule sensors. *Nano Letters* **8,** 4299–4304 (2008).

156. Vogt, S., Schneider, M., Schafer-Eberwein, H. & Noll, G. Determination of the pH dependent redox potential of glucose oxidase by spectroelectrochemistry. *Analytical Chemistry* **86,** 7530–7535 (2014).

157. Stankovich, M. T., Schopfer, L. M. & Massay, V. Determination of glucose oxidase ox-red potentials and the oxygen reactivity of fully reduced and semiquinoid forms. *Journal of Biological Chemistry* **253,** 4971–4979 (1978).

158. Guiseppi, A., Lei, C. H. & Baughman, R. H. Direct electron transfer of glucose oxidase on carbon nanotubes. *Nanotechnology* **13,** 559–564 (2002).

159. Lowe, H. J. & Clark, W. M. Studies on oxidation-reduction: oxidation-redaction potentials of flavin adenine dinucleotide. *Journal of Biological Chemistry* **221,** 983–992 (1956).

160. Hirana, Y. *et al.* Empirical prediction of electronic potentials of single-walled carbon nanotubes with a specific chirality (n,m). *Scientific Reports* **3,** 1–6 (2013).

161. Liu, Y., Wang, M., Zhao, F., Xu, Z. & Dong, S. The direct electron transfer of glucose oxidase and glucose biosensor based on carbon nanotubes/chitosan matrix. *Biosensors and Bioelectronics* **21,** 984–988 (2005).

162. Hu, S. & Hu, C. Carbon nanotube-based electrochemical sensors: Principles and applications in biomedical systems. *Journal of Sensors* **2009,** 1–40 (2009).

163. Luong, J. H. T., Glennon, J. D., Gedanken, A. & Vashist, S. K. Achievement and assessment of direct electron transfer of glucose oxidase in electrochemical biosensing using carbon nanotubes, graphene, and their nanocomposites. *Microchimica Acta* **184,** 369–388 (2017).

164. Zheng, Y., Bachilo, S. M. & Weisman, R. B. Quenching of single-walled carbon nanotube fluorescence by dissolved oxygen reveals selective single-stranded DNA affinities. *The Journal of Physical Chemistry Letters* **8,** 1952–1955 (2017).

165. Zheng, M. & Diner, B. A. Solution redox chemistry of carbon nanotubes. *Journal of the American Chemical Society* **126,** 15490–15494 (2004).

166. Shiraishi, T. *et al.* Determination of precise redox properties of oxygen-doped single-walled carbon nanotubes based on in situ photoluminescence electrochemistry. *Journal of Physical Chemistry C* **120,** 15632–15639 (2016).

167. Chiu, C. S., Kartalov, E., Unger, M., Quake, S. & Lester, H. a. Single-molecule measurements calibrate green fluorescent protein surface densities on transparent beads for use with 'knock-in' animals and other expression systems. *Journal of Neuroscience Methods* **105,** 55–63 (2001).

168. Dresselhaus, M. S., Jorio, A., Souza Filho, A. G. & Saito, R. Defect characterization in graphene and carbon nanotubes using Raman spectroscopy. *Philosophical Transactions of the Royal Society A* **368,** 5355–5377 (2010).

169. Corio, P. *et al.* Potential dependent surface Raman spectroscopy of single wall carbon nanotube films on platinum electrodes. *Physical Chemistry Letters* **370,** 675–682 (2003).

170. Kavan, L. *et al.* Electrochemical tuning of electronic structure of single-walled carbon nanotubes: in-situ Raman and Vis-NIR study. *Journal of Physical Chemistry B* **105,** 10764–10771 (2001).

171. Kavan, L., Kalbac, M., Zukalova, M. & Dunsch, L. Electrochemical doping of chirality - resolved carbon nanotubes. *Journal of Physical Chemistry B* **109,** 19613–19619 (2005).

172. Kang, D., Park, N., Ko, J.-H., Bae, E. & Park, W. Oxygen-induced p-type doping of a long individual single-walled carbon nanotube. *Nanotechnology* **16,** 1048–1052 (2005).

173. Strano, M. S. *et al.* Reversible, band-gap-selective protonation of single-walled carbon nanotubes in solution. *The Journal of Physical Chemistry B* **107,** 6979–6985 (2003).

174. Naderi, Ali. Higher current ratio and improved ambipolar behavior in graphene nanoribbon field effect transistors by symmetric pocket doping profile. *ECS Journal of Solid State Science and Technology* **5,** M148–M153 (2016).

175. Guin, S., Chattopadhyay, A., Karmakar, A. & Mallik, A. Impact of a pocket doping on the device performance of a Schottky tunneling field-effect transistor. *IEEE Transactions on Electron Devices* **61,** 2515–2522 (2014).

176. Tung, N. T. *et al.* Peptide aptamer-modified single-walled carbon nanotube-based transistors for high-performance biosensors. *Scientific Reports* **7,** 1–9 (2017).

177. Shim, M., Kam, N. W. S., Chen, R. J., Li, Y. & Dai, H. Functionalization of carbon nanotubes for biocompatibility and biomolecular recognition. *Nano Letters* **2,** 285–288 (2002).

178. Liu, Z., Tabakman, S., Welsher, K. & Dai, H. Carbon nanotubes in biology and medicine: In vitro and in vivo detection, imaging and drug delivery. *Nano Research* **2,** 85–120 (2009).

179. McNicholas, T. P. *et al.* Structure and function of glucose binding protein-single walled carbon nanotube complexes. *Small* **8,** 3510–3516 (2012).

180. Salice, P., Gambarin, A., Daldosso, N., Mancin, F. & Menna, E. Noncovalent interaction between single-walled carbon nanotubes and pyrene-functionalized gold nanoparticles in water-soluble nanohybrids. *Journal of Physical Chemistry C* **118,** 27028–27038 (2014).

181. Tsien, R. Y. The green fluorescent protein. *Annual Review of Biochemistry* **67,** 509–544 (1998).

182. Patterson, R. E., Weatherbee-Martin, N. & Rainey, J. K. Pyrene-apelin conjugation modulates fluorophore- and peptide-micelle interactions. *Journal of Physical Chemistry B* **121,** 4768–4777 (2017).

183. Micsonai, A. *et al.* BeStSel: A web server for accurate protein secondary structure prediction and fold recognition from the circular dichroism spectra. *Nucleic Acids Research* **46,** W315–W322 (2018).

184. Micsonai, A. *et al.* Accurate secondary structure prediction and fold recognition for circular dichroism spectroscopy. *Proceedings of the National Academy of Sciences* **112,** E3095–E3103 (2015).

185. Williams, R. M. *et al.* Noninvasive ovarian cancer biomarker detection via an optical nanosensor implant. *Science Advances* **4,** 1–11 (2018).

186. Wu, C. W., Yarbrough, L. R. & Wu, F. Y. H. N-(1-Pyrene)maleimide: a fluorescent crosslinking reagent. *Biochemistry* **15,** 2863–2868 (1976).

187. Bachilo, S. M. *et al.* Structure-assigned optical spectra of single-walled carbon nanotubes. *Science* **298,** 2361–2366 (2002).

188. Choi, J. H. & Strano, M. S. Solvatochromism in single-walled carbon nanotubes. *Applied Physics Letters* **90,** 1–3 (2007).

189. Freeley, M. *et al.* Site-specific one-to-one click coupling of single proteins to individual carbon nanotubes: a single-molecule approach. *Journal of the American Chemical Society* **139,** 17834–17840 (2017).

190. Saeed, I. A. & Ashraf, S. S. Denaturation studies reveal significant differences between GFP and blue fluorescent protein. *International Journal of Biological Macromolecules* **45,** 236–241 (2009).

191. Prakrit V, J., Mohammad M., S., Daniel A., H. & Daniel, R. DNA-carbon nanotube complexation affinity and photoluminescence modulation are independent. *ACS Applied Mater Interfaces* **9,** 21397–21405 (2017).

192. Roxbury, D., Tu, X., Zheng, M. & Jagota, A. Recognition ability of DNA for carbon nanotubes correlates with their binding affinity. *Langmuir* **27,** 8282–8293 (2011).

193. Oh, H., Sim, J. & Ju, S. Y. Binding affinities and thermodynamics of noncovalent functionalization of carbon nanotubes with surfactants. *Langmuir* **29,** 11154–11162 (2013).

194. Kato, Y., Inoue, A., Niidome, Y. & Nakashima, N. Thermodynamics on soluble carbon nanotubes: how do DNA molecules replace surfactants on carbon nanotubes. *Scientific Reports* **2,** 1–7 (2012).

195. Feng, W. & Ji, P. Enzymes immobilized on carbon nanotubes. *Biotechnology Advances* **29,** 889–895 (2011).

196. Sanz, V., Coley, H. M., Silva, S. R. P. & McFadden, J. Modeling the binding of peptides on carbon nanotubes and their use as protein and DNA carriers. *Journal of Nanoparticle Research* **14,** 1–13 (2012).

197. Ge, C. *et al.* Binding of blood proteins to carbon nanotubes reduces cytotoxicity. *Proceedings of the National Academy of Sciences* **108,** 16968–16973 (2011).

198. Kommoju, P., Chen, Z., Bruckner, R. C., Mathews, F. S. & Jorns, M. S. Probing oxygen activation sites in two flavoprotein oxidases. *Biochemistry* **50,** 5521–5534 (2011).

199. Wohlfahrt, G. *et al.* 1.8 and 1.9 A resolution structures of the Penicillium amagasakiense and Aspergillus niger glucose oxidases as a basis for modelling substrate complexes. *Acta Crystallographica Section D: Biological Crystallography* **55,** 969–977 (1999).

200. Filla, N., Ramasamy, R. & Wang, X. Forces, energetics, and dynamics of conjugated-carbon ring tethers adhered to CNTs: a computational investigation. *Physical Chemistry Chemical Physics* **20,** 11327–11335 (2018).

201. Yang, Z., Wang, Z., Tian, X., Xiu, P. & Zhou, R. Amino acid analogues bind to carbon nanotube via $\pi\pi$ - interactions: comparison of molecular mechanical and quantum mechanical calculations. *Journal of Chemical Physics* **136,** 1–10 (2012).

202. Ashkenazy, H., Erez, E., Martz, E., Pupko, T. & Ben-Tal, N. ConSurf 2010: calculating evolutionary conservation in sequence and structure of proteins and nucleic acids. *Nucleic Acids Research* **38,** W529–W533 (2010).

203. Edelheit, O., Hanukoglu, A. & Hanukoglu, I. Simple and efficient site-directed mutagenesis using two single-primer reactions in parallel to generate mutants for protein structure-function studies. *BMC Biotechnology* **9,** 1–8 (2009).

204. Lin-Cereghino, J. *et al.* Condensed protocol for competent cell preparation and transformation of the methylotrophic yeast Pichia pastoris. *BioTechniques* **38,** 44–48 (2005).

205. Bateman, R. C. & Evans, J. A. Using the glucose oxidase/peroxidase system in enzyme kinetics. *Journal of Chemical Education* **72,** A240–A241 (1995).

206. Gu, L., Zhang, J., Liu, B., Du, G. & Chen, J. High-level extracellular production of glucose oxidase by recombinant Pichia pastoris using a combined strategy. *Applied Biochemistry and Biotechnology* **175,** 1429–1447 (2015).

207. Finnegan, S. & Percival, S. L. EDTA: an antimicrobial and antibiofilm agent for use in wound care. *Advances in Wound Care* **4,** 415–421 (2015).

208. Hermanson, G. T. *Bioconjugate techniques* 3rd edition (Elsevier Inc., 2013).

209. Mukhortava, A. & Schlierf, M. Efficient formation of site-specific protein-DNA hybrids using copper-free click chemistry. *Bioconjugate Chemistry* **27,** 1559–1563 (2016).

210. Looser, V. *et al.* Cultivation strategies to enhance productivity of Pichia pastoris: a review. *Biotechnology Advances* **33,** 1177–1193 (2014).

211. Witt, S., Singh, M. & Kalisz, H. M. Structural and kinetic properties of nonglycosylated recombinant Penicillium amagasakiense glucose oxidase expressed in Escherichia coli. *Applied and Environmental Microbiology* **64,** 1405–1411 (1998).

212. Brooks, S. A. Appropriate glycosylation of recombinant proteins for human use: implications of choice of expression system. *Molecular Biotechnology* **28,** 241–256 (2004).

213. Leskovac, V., Trivić, S., Wohlfahrt, G., Kandrač, J. & Peričin, D. Glucose oxidase from Aspergillus niger: the mechanism of action with molecular oxygen, quinones, and one-electron acceptors. *International Journal of Biochemistry and Cell Biology* **37,** 731–750 (2005).

214. Kavimandan, N. J., Losix, E., Wilson, J. J., Brodbelt, J. S. & Peppas, N. A. Synthesis and characterization of insulin-transferrin conjugates. *Biocojugate Chemistry* **17,** 1376–1384 (2006).

215. Bains, G., Patel, A. B. & Narayanaswami, V. Pyrene: a probe to study protein conformation and conformational changes. *Molecules* **16,** 7909–7935 (2011).

216. Jeng, E. S., Moll, A. E., Roy, A. C., Gastala, J. B. & Strano, M. S. Detection of DNA hybridization using the near-infrared band-gap fluorescence of single-walled carbon nanotubes. *Nano Letters* **6,** 371–375 (2006).

217. Bisker, G. *et al.* Insulin detection using a corona phase molecular recognition site on single-walled carbon nanotubes. *ACS Sensors* **3,** 367–377 (2018).

218. Jena, P. V. *et al.* A carbon nanotube optical reporter maps endolysosomal lipid flux. *ACS Nano* **11,** 10689–10703 (2017).

219. Nelson, J. T. *et al.* Mechanism of immobilized protein A binding to immunoglobulin G on nanosensor array surfaces. *Analytical Chemistry* **87,** 8186–8193 (2015).

220. Kallmyer, N., Musielwicz, J., Sutter, J. & Reuel, N. Substrate-wrapped, single-walled carbon nanotube probes for hydrolytic enzyme characterization. *Analytical Chemistry* **90,** 5209–5216 (2018).

221. He, X. *et al.* Carbon nanotubes as emerging quantum-light sources. *Nature Materials* **17,** 663–670 (2018).

222. Lambert, B., Gillen, A. J., Schuergers, N., Wu, S. J. & Boghossian, A. A. Directed evolution of the optoelectronic properties of synthetic nanomaterials. *Chemical Communications* **55,** 3239–3242 (2019).

223. Heller, D. A. *et al.* Multimodal optical sensing and analyte specificity using single-walled carbon nanotubes. *Nature Nanotechnology* **4,** 114–120 (2009).

224. Ao, G., Streit, J. K., Fagan, J. A. & Zheng, M. Differentiating left- and right-handed carbon nanotubes by DNA. **138,** 16677–16685 (2016).

225. Liu, Z. *et al.* Quasi-confocal, multichannel parallel scan hyperspectral fluorescence imaging method optimized for analysis of multicolor microarrays. *Analytical Chemistry* **82,** 7752–7757 (2010).

226. Peigney, A., Laurent, C., Flahaut, E., Bacsa, R. R. & Rousset, A. Specific surface area of carbon nanotubes and bundles of carbon nanotubes. *Carbon* **39,** 507–514 (2001).

Curriculum Vitae

Vitalijs Zubkovs

Ph.D. in Chemistry and Chemical Engineering

vitalijs.zubkovs@gmail.com

linkedin.com/in/vitalijszubkovs

Born 5th September 1988 in Latvia

EDUCATION

May 2015 – present

Ph.D. Candidate in Chemistry and Chemical Engineering

Laboratory of NanoBiotechnology, EPFL, Lausanne

- Title of the doctoral thesis: "Protein Bioconjugation to Carbon Nanotubes for Near-Infrared Sensing"

2011 – 2013

M.Sc. in Surface, Electro, Radiation, and Photo Chemistry

Paris-Sud University, Paris region, France

- Title of the master thesis: "Potentials of Combination Second Harmonic Generation (SHG) Imaging and Deep-UV Autofluorescence for Tissue Diagnosis"

2007 – 2010

B.Sc. in Chemistry

University of Latvia, Riga, Latvia

- Title of the semester project: "Tritium Accumulation in Beryllium Pebbles after Fast Neutron Flux Irradiation"

WORK EXPERIENCE

May 2015 – present

Doctoral Assistant

Laboratory of NanoBiotechnology, EPFL

October 2013 – April 2015

Laboratory Assistant

Laboratory for fundamental BioPhotonics, EPFL

May 2009 – July 2011

Laboratory Assistant

Institute of Chemical Physics, University of Latvia

INTERNSHIPS

January 2013 – July 2013

Intern

French national synchrotron facility – SOLEIL, Paris region

TEACHING

Teaching assistant for a course Electrochemical engineering (ChE-407)
Supervised students in 3 master theses and 2 internship projects

AWARDS & FELLOWSHIPS

2016

Chemistry Travel Award

from Swiss Academy of Sciences and Swiss Chemical Society

2011

Erasmus Mundus Fellowship

for studies at the joint European Master's program

TRAININGS

February 2019

Developing Leadership Skills

Organized by the Staff Training Service at EPFL

- Acquiring tools for developing emotional intelligence and managing diverse teams

November 2018

MDR/IVDR - Status Report from Stakeholders

Organized by the Regulatory Affairs Professional Society (RAPS) in Bern

- Discussion about new regulations for medical devices certification in the EU

June – September 2018

Management of Innovation and Technology Transfer (MINTT)

Organized by the Technology Transfer Office (TTO) at EPFL

- Analysis of patent application process, examples of technology commercialization, and case studies on EPFL start-ups

October – November 2017

Entrepreneurial Opportunity Identification and Exploitation

Taught by Sharon Tal Itzkovitch and Marc Gruber at EPFL

- Understanding the method of linking technology to market opportunities

October – December 2016

Academia-Industry Training (AIT) Camp

Organized by VentureLab and Swissnex India in Switzerland and India

- Entrepreneurial training and case studies on project commercialization

August 2016

Summer School on Healthcare Diagnostics

Fiesch, Switzerland

- Healthcare diagnostics - technological, economic and social perspectives

September – December 2015

Business Concept

Organized by the Swiss Commission for Technology and Innovation (CTI) in Lausanne

- Essential tools for start-up creation

June 2015

NCCR Chemical Biology Workshop on Image-based High Throughput Screening

University of Geneva

- Introduction to high throughput microscopy

January 2014

Practical Course in Advanced Microscopy

Organized by the Center for Microscopy and Image Analysis (ZMB) at ETH Zurich

- Hands-on and lectures on high resolution light microscopy

June 2013

Summer School of Biophotonics

Pavol Jozef Safarik University, Kosice, Slovakia

- Theoretical and practical courses in optics and live cell analysis

July 2012

Summer School on Science Management for Scientists and Engineers

University of Genoa, Genoa, Italy

- Fundamentals of patent law, branding, and trademarks

PUBLICATIONS

2018 Zubkovs, V., Antonucci, A., Schuergers, N., Lambert, B., Latini, A., Ceccarelli, R., Santinelli, A., Rogov, A., Ciepielewski, D., Boghossian, A. A. Spinning-disc confocal microscopy in the second near-infrared window (NIR-II) • Scientific Reports

2017 Zubkovs, V., Schuergers, N., Lambert, B., Ahunbay, E., Boghossian, A. A. Mediatorless, reversible optical nanosensor enabled through enzymatic pocket doping • Small

2016 Macias-Romero, C., Zubkovs, V., Wang, S., Roke, S. Wide-field medium-repetition-rate multiphoton microscopy reduces photodamage of living cells • Biomedical Optics Express

2014 Macias-Romero, C., Didier, M., Jourdain, P., Marquet, P., Magistreti, P., Tarun, O., Zubkovs, V., Radenovic, A., Roke, S. High throughput second harmonic imaging for label-free biological applications • Optics Express

2014 Macias-Romero, C., Diedier, M., Zubkovs, V., Delannoy, L., Dutto, F., Radenovic, A., Roke, S. Probing rotational and translational diffusion of nanodoublers in living cells on micro-second time scales • NANO Latters

2014 Zubkovs, V., Jamme, F., Kascakova, V., Chiappini, F., LeNaour, F., Refregiers, M. Single vs. two-photon microscopy for label free intrinsic tissue studies in the UV light region • Analyst

2013 Vitins, A., Kizane, G., Matiss, A., Pajuste, E., Zubkovs, V. Tritium release behavior of beryllium pebbles after neutron irradiation between 523 and 823 K • Journal of Nuclear Materials

2011 Vitins, A., Zubkovs, V., Kizane, G., Pajuste, E., Kinerte, V. Tritium release characteristics of neutron-irradiated reference beryllium pebbles for the helium cooled pebble bed (HCPB) blanket • Fusion Science and Technology

2011 Pajuste, E., Vitins, A., Kizane, G., Zubkovs, V., Birjukovs, P. Tritium distribution and chemical forms in the irradiated beryllium pebbles before and after annealing • Fusion Engineering and Design

CONFERENCES

December 2018 International Workshop on Smart Materials. Sensors, and Energy Devices (SMSED 2018) in Kalavakkam (Chennai), India (oral presentation)

October 2018 AIChE Annual Meeting in Pittsburgh, the USA (poster)

October 2018 Swiss Symposium in Point-of-Care Diagnostics in Chur, Switzerland (poster)

September 2018 Swiss Chemical Society Fall Meeting in Lausanne, Switzerland (poster)

May 2017 Raman Microscopy Workshop at ETH Zurich in Zurich, Switzerland (oral presentation)

September 2016 Trends in NanoTechnology (TNT) Conference in Fribourg, Switzerland (poster)

May 2016 229th Electro Chemical Society Meeting in San Diego, the USA (oral presentation)

April 2015 Croatian Microscopy Congress in Zadar, Croatia (oral presentation)

February 2014 Chemical Imaging by Coherent Raman Microscopy in Les Houche, France (poster)

SKILLS

Languages

Latvian – native speaker
Russian – native speaker
English – fluent
French – intermediate
- Certificate of completion level B1 from the Language Centre at EPFL

German – elementary
- Certificate of completion level A2 from the Language Centre at EPFL

IT-literacy & computing

Python • MATLAB • Adobe (Illustrator, InDesign) • ImageJ • LaTeX • MS Office (Word, Power Point, Excel) • Blender

Mastered techniques

Light microscopy • Optical engineering • Non-linear microscopy • UV-Vis-NIR spectroscopy • Fourier-Transform Infrared (FTIR) spectroscopy • Cell culture • Protein engineering • Scanning Electron Microscopy (SEM) • Dynamic Light Scattering (DLS) • Chromatography • Thermal Gravimetric Analysis (TGA)

ADDITIONAL INFORMATION

Volunteering

Laboratory safety officer at the Laboratory of NanoBiotechnology
- Certificate from Ecoservices: Basic knowledge of workplace safety and health protection
- Training of the laboratory members on lab safety, work with nanoparticles, and toxic or biological waste disposal

Vice President at the public speaking club Toastmasters International at EPFL from July 2016 until June 2018
- Organization of club events, club's membership management

Memberships

Swiss Chemical Society (SCS)
- Participation in annual meetings and organized activities

Regulatory Affairs Professional Society (RAPS)
- Member of the RAPS Switzerland Chapter

Toastmasters International
- Practical training in public speaking and leadership. Member since April 2015

Interests

Running • Hiking • Rock climbing

**Ce document a été imprimé au Centre d'impression EPFL,
imprimerie climatiquement neutre, certifiée myClimate.**